

Partial-Wave Analysis of $\tau^- \rightarrow \pi^- \pi^- \pi^+ \nu_\tau$ at Belle

Andrei Rabusov

Vollständiger Abdruck der von der TUM School of Natural Sciences der
Technischen Universität München zur Erlangung eines

Doktors der Naturwissenschaft (Dr. rer. nat.)

genehmigten Dissertation.

Vorsitz:

apl. Prof. Dr. Norbert Kaiser

Prüfer*innen der Dissertation:

1. Prof. Dr. Stephan Paul
2. apl. Prof. Dr. Hubert Kroha

Die Dissertation wurde am 21.07.2023 bei der Technischen Universität München
eingereicht und durch die TUM School of Natural Sciences am 08.09.2023
angenommen.

Kurzzusammenfassung

Ich stelle die Ergebnisse einer Partialwellenanalyse von $\tau^- \rightarrow \pi^- \pi^- \pi^+ \nu_\tau$ bei Belle vor. Ich zeige die Anwesenheit der $a_1(1420)$ und $a_1(1640)$ Resonanzen und die Wichtigkeit der $1^-[\omega(782)\pi]_P$ Welle. Die $a_1(1420)$ -Anwesenheit wird mit einem modellunabhängigen Ansatz validiert. Diese Ergebnisse können die Modellierung in Simulationstudien verbessern, die für die Messung der elektrischen und magnetischen Dipolmomente von τ und Michel-Parameter erforderlich ist.

Abstract

I present the results of a partial-wave analysis of $\tau^- \rightarrow \pi^- \pi^- \pi^+ \nu_\tau$ at Belle. I show the presence of the $a_1(1420)$ and $a_1(1640)$ resonances and the significance of the $1^-[\omega(782)\pi]_P$ wave. The $a_1(1420)$ presence is validated using a model-independent approach. These results can improve modeling in simulation studies necessary for measuring the τ electric and magnetic dipole moments and Michel parameters.

Contents

Kurzzusammenfassung	iii
Abstract	v
Contents	vii
1 Introduction	1
2 Belle experiment	5
2.1 KEKB collider	7
2.2 Tracking system	7
2.3 Electromagnetic Calorimeter	8
2.4 Particle identification	8
2.5 Trigger and DAQ	9
2.6 Event reconstruction and simulation	11
3 Event selection	13
3.1 Phase space variables	13
3.1.1 Mass variables	13
3.1.2 Euler angles	14
3.1.3 Helicity angle	15
3.2 Belle data and generic MC sets	17
3.3 Belle skimming	17
3.4 Definition of good charged tracks and photons	19
3.5 Definition of the thrust vector	19
3.6 Event-class boosted decision trees	20
3.7 Backgrounds from the tauon decays	25
4 Background shape parametrization	29
5 Partial-wave analysis	33
5.1 Phase space volume $d\Phi$	33
5.2 Matrix element of $\tau^- \rightarrow \pi^- \pi^- \pi^+ \nu_\tau$	34
5.3 Lepton tensor decomposition	35

CONTENTS

5.4	Lepton tensor averaging over the tauon direction	36
5.5	Partial-wave decomposition	38
5.6	Spin structure of $\tau^- \rightarrow \pi^- \pi^- \pi^+ \nu_\tau$: hadron form-factor	39
5.7	Evaluation of partial waves: covariant tensor formalism	40
5.8	Dynamic factor parametrization of isobars	42
5.9	Fitting method of partial-wave decomposition	43
5.10	Mathematical ambiguities of freed-isobar PWA	45
5.11	Isobar fit	46
5.12	Resonance-model fit	47
5.13	Dynamic amplitude of the $1^+[\rho(770)\pi]_S$ wave	47
6	Simulation studies	49
6.1	Missing-neutrino test	49
6.2	Initial-state radiation test	50
6.3	Spin-spin correlation test	51
6.4	Freed-isobar test	52
7	Results	55
7.1	Partial-wave decomposition	55
7.1.1	Conventional PWA	55
7.1.1.1	1^+ sector	57
7.1.1.2	0^- sector	63
7.1.1.3	1^- sector	64
7.1.2	Freed-isobar PWA	67
7.2	Resonance-model fit	70
8	Systematic uncertainties	73
8.1	Fit model	73
8.2	Background	74
8.3	Acceptance	76
8.4	Resolution	77
9	Discussion	79
10	Conclusion	81
	Appendix A Cut-flow table	83
	Appendix B Acknowledgements	85
	Bibliography	87

1 Introduction

The quark model [1, 2] has had great success in systematizing the so-called particle zoo in 60s, and it still remains the basic tool for thinking about hadrons. It predicts for mesons and baryons their isospin, G -parity, spin, parity, and charge parity quantum numbers, denoted as $I^G J^{PC}$, depending on their quark content. It fails, though, to predict their dynamic amplitudes (in other words, masses and widths).

These properties of light hadrons usually cannot be found from first-principle quantum chromodynamics either, and they need to be measured experimentally. To measure the properties of light mesons one first needs to produce them. Typically, this is done on hadron accelerators with a fixed-target such as VES and COMPASS [3], providing access to a wide variety of J^{PC} with large numbers of events. To reveal how different light meson states contribute to different J^{PC} these experiments perform complex fitting procedures to the data, such as a partial-wave analysis (PWA) [4]. However, hadron accelerators have the disadvantage of producing light mesons alongside other hadrons either in the beam or in the target. Due to the nature of the strong interaction, the obtained light meson properties are influenced by the final-state interaction, and are distorted.

An alternative option is e^+e^- colliders: they produce hadrons in an environment which is free from the final-state strong interaction, but usually they can access only the $J^{PC} = 1^{--}$ sector from direct e^+e^- annihilation. Additionally, e^+e^- colliders can produce other particles that weakly decay to hadrons, thus simultaneously providing a clean environment and accessing different J^{PC} . For example, the decay products of the D-meson have $J^P = 0^-$ quantum numbers, and τ^- -lepton decay products can have $J^P = 1^+, 0^-,$ and 1^- . The latter case can be used to study isospin symmetry breaking when compared with direct e^+e^- measurements. Tauon pairs can be directly produced in large numbers in the $e^+e^- \rightarrow \tau^+\tau^-$ annihilation at the e^+e^- experiments such as Belle [5] and BaBar [6].

In the $\tau^- \rightarrow \pi^-\pi^-\pi^+\nu_\tau$ decay,¹ pions are produced from unflavored axial vector resonances [7]. The dominantly produced resonance is $a_1(1260)$, whose shape is much debated and whose mass and width are not well determined [8–11]. Another puzzle is a narrow axial-vector resonance, $a_1(1420)$ [12], observed by COMPASS in a PWA. Is this also present in $\tau^- \rightarrow \pi^-\pi^-\pi^+\nu_\tau$? Whether $a_1(1420)$ has an exotic nature, or it is just an effect of the triangular diagram of the $a_1(1260)$ decay,

¹The charge conjugation is taken into account implicitly.

1 Introduction

is also debated [13], and requires experimental input using different production mechanism such as the tauon decay.

Tauons are also used as a laboratory for the New Physics searches. Although many decays of the tauon exist, the $\tau^- \rightarrow \pi^- \pi^- \pi^+ \nu_\tau$ one is of particular interest because it provides the spin-analyzing power. Also, it has a relatively large branching fraction, $\mathcal{B} \approx 9\%$, and the reconstruction of this decay is simple due to the absence of neutral pions. However, the $\tau^- \rightarrow \pi^- \pi^- \pi^+ \nu_\tau$ process occurs via intermediate hadron resonances which are not studied well in the tauon decays. This leads to notable discrepancies between simulated and real data and to large systematic uncertainties in the New Physics searches. A better model for $\tau^- \rightarrow \pi^- \pi^- \pi^+ \nu_\tau$, driven by experimental measurements, will improve the simulation of this decay in existing Monte Carlo (MC) generators, which is necessary for the precise measurements of the tauon electric and magnetic dipole moments [14] and the tauon Michel parameters [15] planned with the ongoing experiment Belle II [16].

In the last three decades, several analyses of $\tau^- \rightarrow \pi\pi\pi\nu_\tau$ were published, but in most cases only spectra of two- and three-pions were reported. The only analysis which determined decay amplitudes was done by CLEO II [9]. It is a multidimensional amplitude analysis of $\tau^- \rightarrow \pi^- \pi^0 \pi^0 \nu_\tau$ in the full available phase space of $e^+e^- \rightarrow \tau^+\tau^-$. Unfortunately, CLEO II analysis was conducted assuming that all partial waves have the same shape in $m_{3\pi}$, which is known to be false. A better approach would be to perform a PWA without this assumption. Such analysis probably was not possible at CLEO II mainly because the data sample contained 37×10^3 events.

This limitation of the CLEO II analysis could be bypassed at the newer e^+e^- experiments, where a much larger recorded data is available. However, they have published only mass spectra as a byproduct of the $\tau^- \rightarrow \pi^- \pi^- \pi^+ \nu_\tau$ branching fraction measurements: BaBar published two- and three-pion invariant mass spectra [17] using 1.6×10^6 events, and Belle published a three-pion invariant mass spectrum [18] using 9×10^6 events. Neither of them performed a PWA.

There were several consecutive attempts to fit to the BaBar spectra performed by the TAUOLA group [19], intending to improve their MC generator [20, 21] and exploit the Resonance Chiral Perturbation Theory [22–24]. BaBar spectra had shown notable discrepancies with the existing models in TAUOLA. The authors of [25] highlight the need to include into models the scalar and tensor isobars and the $a_1(1640)$ resonance.

This motivates a PWA of $\tau^- \rightarrow \pi^- \pi^- \pi^+ \nu_\tau$ at Belle, where the data sample can reach about 50×10^6 $\tau^- \rightarrow \pi^- \pi^- \pi^+ \nu_\tau$ events. This number of events is compatible with COMPASS and well-suited for PWA.

This thesis describes the first detailed study of the spin structure of the hadron

systems in the $\tau^- \rightarrow \pi^- \pi^- \pi^+ \nu_\tau$ decay. I apply the PWA technique and investigate the three-pion mass spectrum in the mass range of 1.1–1.7 GeV.² For this study I select events clearly identified as $e^+e^- \rightarrow \tau^+\tau^-$ through an unambiguous tagging of one of the tauons. Recoiling against this tauon I require three charged particles. The selection of this event topology makes use of specific selection criteria and a multivariate analysis technique, which is based on boosted decision trees (BDT). The final data sample contains background from decays of tauons into four or more pions, in which additional neutral pions remain unobserved. The background is modeled through a neural network using simulated data.

Although PWA is a common tool in hadron physics, the application of PWA to tauon decays is novel. The standard technique has been adapted for the weak decay with an escaping neutrino, which has ambiguous kinematic information. I prove the validity of this method using simulated data.

²Assume $c = \hbar = 1$ units

2 Belle experiment

To perform a PWA of the $\tau^- \rightarrow \pi^- \pi^- \pi^+ \nu_\tau$ process, millions of tauons need to be produced, and three pions of the $\tau^- \rightarrow \pi^- \pi^- \pi^+ \nu_\tau$ decay need to be reconstructed. The conventional way of tauon production is the $e^+ e^- \rightarrow \tau^+ \tau^-$ reaction at an $e^+ e^-$ collider, where the tauon pair production can be well separated from other processes with purity close to 99%.

Every $e^+ e^-$ collider produces tauon pairs if the energy in the rest of the $e^+ e^-$ collision, \sqrt{s} , is above two masses of the tauon, $2m_\tau$. The production cross-section has a peak slightly above the threshold, and then decreases with \sqrt{s} ,

$$\sigma_{e^+ e^- \rightarrow \tau^+ \tau^-} \approx \frac{4\pi\alpha^2}{3s}, \quad (2.1)$$

where α is the fine-structure constant. The number of produced tauon pairs,

$$N_{\tau^+ \tau^-} = L_{\text{int}} \sigma_{e^+ e^- \rightarrow \tau^+ \tau^-}, \quad (2.2)$$

where L_{int} is the integrated luminosity of an $e^+ e^-$ collider. Thus, to produce a large number of tauon pairs, $\sigma_{e^+ e^- \rightarrow \tau^+ \tau^-}$ and L_{int} need to be large.

So far, the largest L_{int} is achieved at the B-factories. A B-factory is a collider that can produce and record millions of B-meson decays. Two B-factories, BaBar [6] in the US at SLAC National Accelerator Laboratory and Belle [5] in Japan at High Energy Accelerator Research Organization (KEK), were designed and built in the late 90s. The BaBar experiment recorded $L_{\text{int}} = 513 \text{ fb}^{-1}$, while the Belle experiment recorded $L_{\text{int}} = 988 \text{ fb}^{-1}$. They observed CP -violation in the neutral B system, which led to a Nobel Prize award for Kobayashi and Masukawa in 2008. Besides the most notable discovery of CP -violation in the B-sector, B-factories are also capable of measuring various properties of the τ -lepton, because the production cross-section of $e^+ e^- \rightarrow \tau^+ \tau^-$ is about the same as the $B\bar{B}$ one,

$$\sigma_{e^+ e^- \rightarrow \tau^+ \tau^-} \approx 0.9 \text{ nb}. \quad (2.3)$$

Also, B-factories can study the physics of the charm quark, the $e^+ e^-$ annihilation to hadrons via radiative return, and two-photon physics.

Statistical precision increases with the number of reconstructed events. It increases not only with L_{int} , but also with the detection efficiency ε , such that

$$N_{\text{rec}} = \varepsilon L_{\text{int}} \sigma_{e^+ e^- \rightarrow \tau^+ \tau^-} 2B_{\tau^- \rightarrow \pi^- \pi^- \pi^+ \nu_\tau}, \quad (2.4)$$

2 Belle experiment

where $B_{\tau^- \rightarrow \pi^- \pi^- \pi^+ \nu_\tau}$ is the branching fraction of the $\tau^- \rightarrow \pi^- \pi^- \pi^+ \nu_\tau$ process. The factor 2 appears in Eq. (2.4) because both tauons can decay to three charged pions, and I assume there is no CP -violation in the $\tau^- \rightarrow \pi^- \pi^- \pi^+ \nu_\tau$ process. To perform the reconstruction, the decay products of tauons need to be detected and recorded, which was done with the Belle detector.

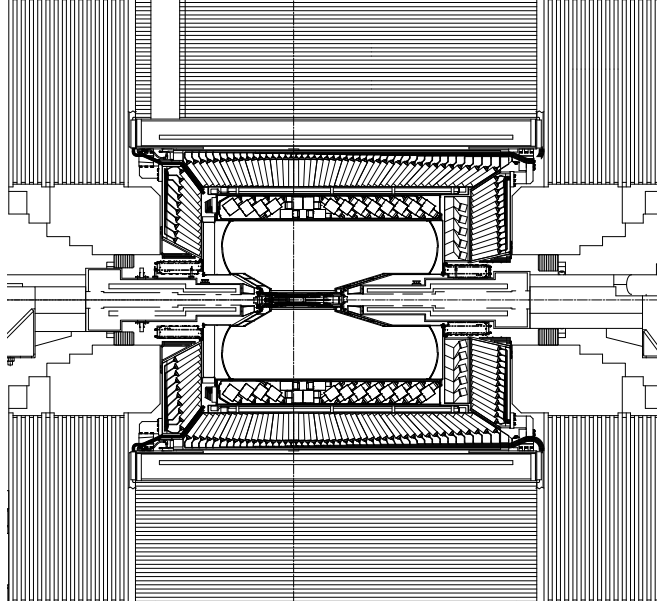


Figure 1: Belle detector schematics, side view.

The Belle detector shown in Fig. 1 was a cylindrical magnet spectrometer installed at the asymmetric e^+e^- collider KEKB [26]. It had an onion-like structure of sub-detectors as described in [5]. Belle consisted of the following sub-detectors: the Silicon Vertex Detector (SVD), the innermost sub-detector, which measured the decay vertices of short-lived particles, the Central Drift Chamber (CDC), which detected charged particles and measured their momenta, the Array of Cerenkov Counters (ACC) and the Time of Flight (ToF), which were designed to distinguish the kinds of charged particles, the Electromagnetic Calorimeter (ECL), which detected photons and measured their energies, and, placed outside the magnetic field, the detector of K_L^0 and muons (KLM), serving also as a yoke of the 1.5 T superconducting magnet [27]. From 1999 to 2010, Belle collected 1 ab^{-1} of L_{int} , which is the largest data set from e^+e^- colliders to date.

2.1 KEKB collider

KEKB is an e^+e^- collider with asymmetric beam energies: $E_{e^-} = 8$ GeV and $E_{e^+} = 3.5$ GeV. KEKB's center-of-momentum energy ($\sqrt{s} = 10.58$ GeV) was designed to correspond to the peak of the $\Upsilon(4S)$ resonance, such that B-mesons are produced almost at rest in pairs, providing an opportunity for flavor tagging. The asymmetric scheme of e^+e^- collisions was needed to measure CP -violation effects in the B sector by analyzing the displacement of B-meson vertices caused by the Lorentz boost in the laboratory frame. Another requirement to the KEKB collider was to operate with an unprecedented instantaneous luminosity to reduce the statistical uncertainties of the CP -asymmetry measurement. To achieve this goal, the collider was constructed with two separate rings: the High-Energy Ring for electrons and Low-Energy Ring for positrons; each ring was populated with about a thousand bunches. In 2009, KEKB reached the world record instantaneous luminosity of $2.11 \times 10^{34} \text{cm}^{-2}\text{s}^{-1}$, which was beaten only in 2021 by the SuperKEKB collider [28].

2.2 Tracking system

The tracking system of Belle consists of the CDC and SVD sub-detectors. The CDC [29], in addition to measuring momenta of electrons, muons, charged pions, charged kaons, protons, and deuterons, provides information about energy loss within its medium. The CDC is a cylinder of 2.4 m length, 83 mm inner and 874 mm outer radii, populated with 33×10^3 field wires.

On average, the CDC reconstructs 20–30 hits per track in axial and 10–20 hits in stereo superlayers. The resulting transverse momentum resolution of a charged particle is

$$\left(\frac{\sigma(p_{\perp})}{p_{\perp}}\right)^2 = (0.0019 p_{\perp})^2 + 0.0034^2, \quad (2.5)$$

where p_{\perp} is the transverse momentum of a particle in GeV.

The CDC provides good momentum resolution for tracks, but its coordinate resolution is not enough to distinguish B meson decay vertices. For this purpose, the SVD detector [30] was designed and installed just around the beam pipe, becoming the closest sub-detector to the interaction point. The SVD achieved $60 \mu\text{m}$ coordinate resolution of decay vertices.

The first version of the SVD was upgraded in summer 2003 from a three-layer to a four-layer strip silicon detector [31], separating the Belle data set into the older SVD1 and the newer SVD2 subsets.

2.3 Electromagnetic Calorimeter

The main purpose of the ECL [32] is photon detection in a large energy range and with a high energy resolution.

The ECL was designed as a homogeneous crystal calorimeter made of CsI(Tl). The ECL consists of barrel and endcap parts. The barrel part has a length of 3 m, and its internal radius equals 1.25 m. The ECL covers the whole range for the azimuth and the $[17^\circ, 150^\circ]$ range for the polar angle, which corresponds to 91% of the 4π spatial angle. There are small gaps between the endcaps and the barrel, which reduce the polar angle coverage by 3% of the 4π spatial angle.

Photons in the ECL are reconstructed from clusters. The clustering algorithm works as follows. First, seeding crystals are found: the energy deposition in a seeding crystal must be above 10 MeV. Then, a geometrically connected region around the seeding crystal is found, in which clusters are defined as a 5×5 matrix of crystals around local maxima. If two clusters share the same crystal, its energy deposition is divided between the clusters according to the total energy deposition of each cluster excluding the shared crystal. Photons are defined first as clusters which are not associated with tracks. Second, if the energy of the cluster is above 600 MeV, the cluster is considered a photon. If the cluster energy is below 600 MeV, the following conditions are required: the cluster energy is above 20 MeV, the root-mean-square weighted by the energy deposition, w , is below 6 cm, and the 3×3 matrix of crystals contains at least 75% of the energy deposition in the cluster.

The obtained energy resolution in Bhabha scattering is 1.7% for the barrel region, 1.74% for the forward endcap, and 2.85% for the backward endcap. The resulting resolution of the two-photon invariant mass peak for the $\pi^0 \rightarrow \gamma\gamma$ decay is 4.9 MeV and for the $\eta \rightarrow \gamma\gamma$ decay is 12.1 MeV.

2.4 Particle identification

Among the large variety of particles, only few hit the detector. From the charged ones, one distinguishes between electrons, muons, pions, kaons, and protons. Some particle kinds can be identified using information from only one of the sub-detectors: protons can be distinguished from the other particles by using mostly the CDC information about the track energy losses dE/dx . Electrons can be identified by large energy deposition in the ECL. Muons pass through the detector material and hit the KLM. The most challenging identification task for Belle is to separate pions from kaons, for which the information from various systems is combined.

At the reconstruction level, the following information is used for particle identification: dE/dx from the CDC, time of flight from the ToF, and number of photo-electrons from the ACC. To separate charged particles of different kinds, this

information is combined into a likelihood $\mathcal{L}_{\text{comb}}$ as a product of the subsystems' likelihoods \mathcal{L}_{ACC} , \mathcal{L}_{ToF} , and \mathcal{L}_{CDC} , assuming that the values are not correlated. The resulting likelihood to detect, for example, a pion, is constructed in the binary manner:

$$\mathcal{L}_{\text{comb}, \pi} = \frac{\mathcal{L}_{\pi}}{\mathcal{L}_{\pi} + \mathcal{L}_{\text{K}}}. \quad (2.6)$$

The ToF [33] measures the flight time of a particle directly, leaving the flight distance fixed, thus measuring the velocity of the particle. The ToF consists of 128 plastic scintillators with the short decay time of 2 ns. They are 4 cm thick, 6 cm wide, and 255 cm long, and placed just in front of the barrel part of the ECL looking from the interaction point, such that the distance from the ToF scintillators to the interaction point is 120 cm. When a charged particle hits a scintillator, the produced light is detected with a time resolution of about 100 ps, which makes it possible to distinguish particles with momenta below 1.5 GeV.

To separate charged particles with larger momenta, the ACC [34] is installed between the CDC and the ECL. The ACC exploits the Cerenkov effect: while a particle of one kind with momentum p emits no Cerenkov photons in the ACC because it is too slow, another particle of another kind with the same momentum p does emit photons, because it is fast enough for a particular media of the ACC. The ACC consists of 960 modules covering the barrel and the forward endcap regions of Belle. The momenta of charged pions and kaons in the B-meson decay are in the 2–3 GeV range. The resulting Belle detection efficiency for pions is in the 85%–95% range while the fake rate from mis-identified kaons is in the 5%–15% range.

Electron identification is done by combining CDC and ECL information with 92% efficiency and 0.5% fake rate caused by pions.

To separate muons from other charged particles, Belle is equipped with the KLM [35]. It consists of alternating layers of glass electrode resistive plate counters and 4.7 cm thick iron plates, having in total 15 sensitive and 14 absorbing layers in the barrel region and 14 sensitive and 14 absorbing layers in the endcap regions. When a muon travels through the KLM, in most cases it does not deposit its whole kinetic energy and passes through the KLM, while a charged pion or kaon interacts with the detector medium strongly and in the end is absorbed by the KLM in the most cases. This effect helps to separate muons from hadrons.

2.5 Trigger and DAQ

Sub-detectors transform hits of final-state particles into electric signals. The amplitude and timing information about these electric signals is recorded on a tape

2 Belle experiment

in order to be processed afterwards off-line. The recording procedure includes several steps: first, the trigger system takes the decision to record the event; then, the data acquisition system (DAQ) gathers the information from the sub-detectors and stores raw information in a computer-readable format. The trigger and DAQ systems need to have an efficiency close to 100% for the physics processes and high retention rate for the background processes. This requires the trigger system to be able to separate between physics and background processes. Furthermore, the DAQ system needs to be stable even if the noise coming from the detector is high: the designed trigger rate limit for the DAQ system was 500 Hz.

Some physics processes have large cross-sections, such as Bhabha scattering ($e^+e^- \rightarrow e^+e^-$) and two-photon annihilation ($e^+e^- \rightarrow \gamma\gamma$). These are used for the detector calibration, but they are not as interesting for analyses as the $e^+e^- \rightarrow B\bar{B}$, $\tau^+\tau^-$, or $q\bar{q}$ processes. To reduce the trigger rate of e^+e^- to e^+e^- and $\gamma\gamma$, these are identified by the primary trigger and recorded only once per several tens of events.

Table 1 lists the physics processes which are subjects of the detailed studies at Belle. The total rate expected from these processes is below 100 Hz.

Process	Cross-section [nb]	Rate [Hz]
$\tau^+\tau^-$	0.9	9.0
$\mu^+\mu^-$	1.0	10.0
$q\bar{q}$	2.8	28.0
$B\bar{B}$	1.1	11.0
$e^+e^- \gamma^* \gamma^*$ ¹	15.0	35.0 ²
Bhabha ³	44.0	4.4 ²
$\gamma\gamma$ ³	2.4	0.2 ²

Table 1: Cross-sections and trigger rates of physics processes at Belle assuming instantaneous luminosity $L = 10^{34} \text{ cm}^{-2} \text{ s}^{-1}$ and beam energy corresponding to the $\Upsilon(4S)$ resonance.

The Belle trigger system [36] consists of three trigger levels: L1, L3, and L4. The L1 trigger level takes the decision to process the event on the level of the electric signals, the L3 trigger level takes decision to record the event for the on-line data processing. The last trigger level, L4, is used for the off-line data processing.

¹ $\theta_{\text{lab}} > 17^\circ$, $p_\perp > 0.1 \text{ GeV}$.

² After trigger suppression.

³ $\theta_{\text{lab}} > 17^\circ$.

2.6 Event reconstruction and simulation

Raw events contain information about hits in the sub-detectors, but for physics analyses, the useful information is parameters of final-state particles such as their types, charges, four-momenta, and coordinates. The reconstruction program is responsible for converting raw hits into reconstructed particles.

Just before the full event reconstruction of the raw data, the L4 trigger level is applied, which uses L1 trigger level information, energy deposition in the ECL, and a fast track reconstruction program. The L4 trigger level reduces the data flow by a factor of three, while the efficiency of physics processes is kept on the 97% level.

The reconstruction program determines the track parameters for the charged particles in the CDC. The track origin is determined with the SVD hits by projecting onto SVD layers the CDC tracks. The reconstruction program finds clusters in the ECL and KLM. Tracks from the CDC are projected onto the ACC, ToF, ECL, and KLM. Hits and clusters which intersect with the projected track are used to determine the type of the charged particle, while clusters in the ECL not assigned to the tracks are treated as photons.

To control the detector performance one needs to simulate the physics of the e^+e^- collisions and the detector response. Also, simulations are used to determine the detector efficiency and to optimize selection criteria.

The physics processes are simulated with MC generators, such as QQ98 [37] and EVTGEN [38] to simulate B and D decays, jetset [39] and PYTHIA [40] to simulate $q\bar{q}$ hadronization, BHLUMI [41] to simulate Bhabha scattering, AAFH [42] to simulate two-photon processes, and KORALB [43] and, later, KKMC [44] to simulate $e^+e^- \rightarrow \mu^+\mu^-$ and $e^+e^- \rightarrow \tau^+\tau^-$.

A program GSIM, based on the GEANT3 framework [45], simulates the detector response for the final-state particles. The program produces low-level information similar to the raw information after the trigger. Then, the reconstruction program processes the obtained low-level information as it was produced by the detector. Finally, the whole simulation and reconstruction chain is validated against known physics processes.

3 Event selection

The Belle detector recorded several billion events, keeping all possible processes interesting for physics analyses. For this work, the $\tau^- \rightarrow \pi^- \pi^- \pi^+ \nu_\tau$ process needs to be selected from the rest to keep the data size compact enough to be processed, transferred, and analyzed in a reasonable time.

The selection procedure is required to retain signal efficiency and signal purity as high as possible. To reach this goal, one needs to find variables whose separation power of signal against background is high. This study is done with simulated data to avoid introducing a bias into the analysis.

Belle already provides pre-selected data samples containing large classes of events sorted with a simple and fast cut-based approach. One of these data samples is suitable for τ analysis, the TauSkim [46]. I further restrict the TauSkim cuts with additional selection criteria and a boosted decision tree. This results in 55×10^6 data events for the full integrated luminosity with 13% background contamination in the signal region, estimated with the simulated data.

3.1 Phase space variables

The $\tau^- \rightarrow \pi^- \pi^- \pi^+ \nu_\tau$ process is a four-body decay. Every four-body decay can be parametrized with seven phase-space variables: three mass variables, three Euler angles, and one helicity angle. The following notation for τ^\mp decay will be used: \vec{p}_1, \vec{p}_2 denote π^\mp momenta in the center-of-momentum frame of the e^+e^- system (CMS), and \vec{p}_3 denotes the π^\pm momentum. The order of pions with the same charge is randomized.

3.1.1 Mass variables

The sum of the pion momenta in the CMS is denoted as q^μ , and the invariant mass of the three pions is

$$m_{3\pi} \equiv \sqrt{q^2}. \tag{3.1}$$

The squares of invariant masses of pion pairs are defined as

$$s_1 \equiv m_{23}^2 = (p_2^\mu + p_3^\mu)^2, \tag{3.2}$$

3 Event selection

$$s_2 \equiv m_{13}^2 = (p_1^\mu + p_3^\mu)^2, \quad (3.3)$$

and

$$s_3 = m_{12}^2 = (p_1^\mu + p_2^\mu)^2. \quad (3.4)$$

In the m_{ij} notation, indices i and j denote pions, while in the s_i notation, the index i denotes a pair of pions whose indices are not i .

The s_3 variable can be expressed via q^2 , s_1 , and s_2 ,

$$s_3 = q^2 - s_1 - s_2 + 3m_\pi^2, \quad (3.5)$$

where m_π is the mass of a charged pion.

3.1.2 Euler angles

Pion momenta boosted to the three-pion rest frame are denoted as \vec{q}_1 , \vec{q}_2 , \vec{q}_3 , where pions with the same charge are reordered such that $|\vec{q}_2| > |\vec{q}_1|$. The direction of the CMS in the three-pion frame is opposite to the sum of three-pion momenta in the CMS:

$$\vec{n}_{\text{CMS}} = -\hat{q} \equiv -\vec{q}/|\vec{q}|. \quad (3.6)$$

Let us define

$$\vec{n}_\perp = \frac{\vec{q}_1 \times \vec{q}_2}{|\vec{q}_1 \times \vec{q}_2|}, \quad (3.7)$$

$$\cos \beta = \vec{n}_{\text{CMS}} \cdot \vec{n}_\perp, \quad (3.8)$$

$$\cos \gamma = -\frac{\vec{n}_{\text{CMS}} \cdot \vec{q}_3}{|\vec{n}_{\text{CMS}} \times \vec{n}_\perp|}, \quad (3.9)$$

$$\sin \gamma = \frac{(\vec{n}_{\text{CMS}} \times \vec{n}_\perp) \cdot \vec{q}_3}{|\vec{n}_{\text{CMS}} \times \vec{n}_\perp|}. \quad (3.10)$$

\vec{n}_\perp is the normal to the decay plane in the three-pion rest frame. β and γ , shown in Fig. 2, are two Euler angles of the rotation from one coordinate system to another, both in the hadron rest frame.

In the first coordinate system, the \mathcal{Z} -axis points in the \vec{n}_{CMS} direction, and the tauon momentum lies in the plane of \mathcal{Z} - and \mathcal{X} -axis. In the second coordinate system, the \mathcal{X} -axis points towards the \vec{q}_3 direction, and the \mathcal{Z} -axis is perpendicular to the decay plane and points towards the \vec{n}_\perp direction. The Euler angle α , defined as the angle between the two planes $\{\vec{n}_{\text{CMS}}, \vec{n}_\tau\}$ and $\{\vec{n}_{\text{CMS}}, \vec{n}_\perp\}$, is not measured. β , the angle between \vec{n}_\perp and \vec{n}_{CMS} , and γ , the angle between the $\{\vec{n}_{\text{CMS}}, \vec{n}_\perp\}$ and $\{\vec{n}_\perp, \vec{q}_3\}$ planes, are measured.

The Euler angle α can be measured with two-fold ambiguity by using only hadronic decays of the tagging tauon [47], but the data sample is smaller in this case. Direct reconstruction of the tauon direction using vertex information is

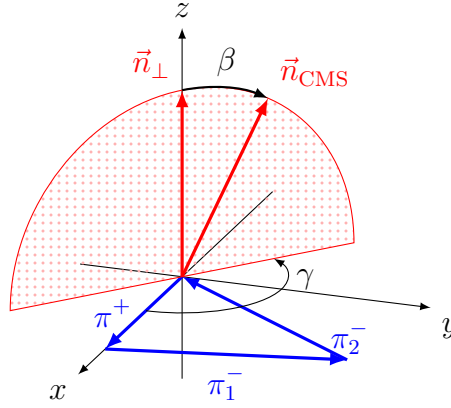


Figure 2: Euler angles β and γ .

not feasible at Belle, because taus decay mostly inside the interaction region of colliding beams. The tauon lifetime $c\tau \approx 87 \mu\text{m}$, and beam radii at Belle are approximately $120 \mu\text{m}$. Thus, the tauon decay rate must be averaged over α .

3.1.3 Helicity angle

At Belle the initial state is known with good precision. In the laboratory frame, $E_{e^-} = 8 \text{ GeV}$, $E_{e^+} = 3.5 \text{ GeV}$, and the crossing angle is 22 mrad . In the CMS

$$E_{e^-} = E_{e^+} \equiv E_{\text{beam}}, \quad (3.11)$$

where E_{beam} denotes the energy of electrons and positrons from beams in the CMS. The Mandelstam variable s is defined as square of the total four-momentum [48], thus

$$s = 4E_{\text{beam}}^2. \quad (3.12)$$

Ignoring the initial-state radiation (ISR), tauon energy and momentum magnitude in the CMS can be written as

$$E_\tau = E_{\text{beam}}, \quad |\vec{p}_\tau| = \sqrt{E_\tau^2 - m_\tau^2}. \quad (3.13)$$

In $\tau^- \rightarrow \pi^- \pi^- \pi^+ \nu_\tau$ only one neutrino is produced, thus the angle between the tauon and the three-pion momentum (helicity angle) can be evaluated in three rest frames: in the CMS, in the three-pion rest frame, and in the tauon rest frame.

The helicity angle in the CMS, Θ , is evaluated as

$$\Theta = \arccos \frac{|\vec{p}_\tau|^2 + |\vec{q}|^2 - |\vec{p}_\nu|^2}{2|\vec{p}_\tau| \cdot |\vec{q}|}, \quad (3.14)$$

3 Event selection

where the neutrino momentum magnitude $|\vec{p}_\nu|$ is

$$|\vec{p}_\nu| = E_\nu = E_\tau - E_{\text{had}}, \quad (3.15)$$

assuming massless neutrino, and E_{had} is the energy of three pions in CMS.

The helicity angle in the three-pion system, ψ , is the angle between the tauon and $-\vec{n}_{\text{CMS}}$,

$$\psi = \arccos \frac{2 m_\tau^2 E_{\text{had}}/E_\tau - m_\tau^2 - q^2}{(m_\tau^2 - q^2) \sqrt{1 - 4m_\tau^2/s}}. \quad (3.16)$$

The helicity angle in the tauon rest frame, θ , is the angle between the hadron system and $-\vec{n}_{\text{CMS}}$ from tau,

$$\theta = \arccos \frac{2E_{\text{had}} - E_\tau (1 + q^2/m_\tau^2)}{|\vec{p}_\tau| \cdot \left(1 - \sqrt{q^2}/m_\tau\right)}. \quad (3.17)$$

Fig. 3 shows $\cos \Theta$, $\cos \psi$, and $\cos \theta$ distributions of 1×10^6 events produced with a generic phase space generator [49]. Fig. 3a shows that the $\cos \Theta$ distribution has a narrow peak towards 1. Fig. 3b shows that $\cos \psi$ peaks towards -1 , but not as narrowly as $\cos \Theta$. Fig. 3c shows that the $\cos \theta$ distribution is flat, thus $\cos \theta$ is used for MC generation.

ISR reduces E_τ and thus affects the helicity angle. For a small fraction of events, reconstructed $E_{\text{had}} > E_\tau$ due to the finite resolution, which makes $|\cos \psi| > 1$. These events are removed from the analysis.

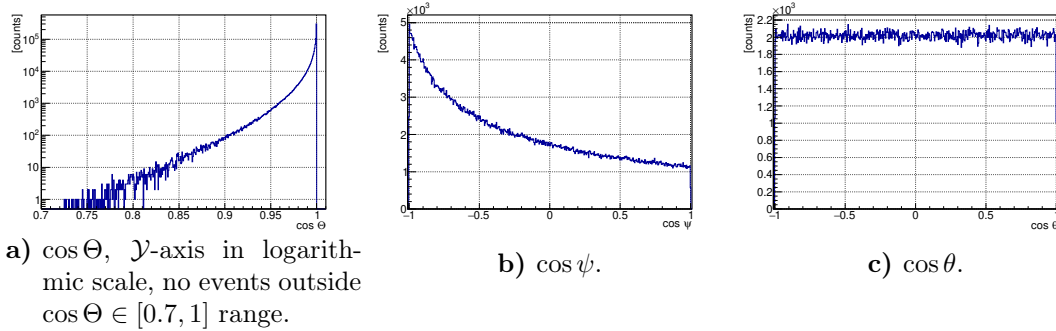


Figure 3: Phase space distribution for the helicity angle in CMS (Fig. 3a), three-pion (Fig. 3b), and tauon (Fig. 3c) rest frames.

3.2 Belle data and generic MC sets

The Belle data set is divided into two subsets collected with the SVD1 and SVD2 vertex detectors. The data was collected mostly at the $\Upsilon(4S)$ resonance, but it also includes $\Upsilon(nS)$ resonances where $n \in \{1, 2, 3, 5\}$, corresponding resonance shape scans, and the off-resonance regions. The integrated luminosities are shown in Table 2.

Vertex detector	Resonance	Integrated luminosity (fb^{-1})
SVD1	$\Upsilon(4S)$	140.747
	continuum	15.621
	rest	0
SVD2	$\Upsilon(4S)$	562.615
	continuum	73.833
	rest	188.06

Table 2: Belle integrated luminosity. Continuum row denotes the off-resonance region near $\Upsilon(4S)$ resonance. Rest row denotes the $\Upsilon(5S)$ and $\Upsilon(1-3S)$ resonances, resonance shape scans, and the off-resonance regions, not included in either $\Upsilon(4S)$ or continuum data sets.

The standard Belle MC data sets already contain the signal $e^+e^- \rightarrow \tau^+\tau^-$ process where one of two tauons decays to three charged pions. The KKMC generator [44] is used to generate the tauon pair production in the e^+e^- collision, and TAUOLA [21] generates the tauon decay to three charged pions using the CLEO II [9] model.

The luminosity of the $e^+e^- \rightarrow \tau^+\tau^-$ MC sample is $10 \times L_{\text{int}}$ for the SVD2 setup (Table 2) and $5 \times L_{\text{int}}$ for the SVD1 setup. [50] describes how the $e^+e^- \rightarrow \tau^+\tau^-$ and other quantum electrodynamics (QED) samples are produced and stored.

For developing selection criteria, only 2% of L_{int} are analysed to demonstrate that the processes other than the tauon pair production and the e^+e^- annihilation to hadrons have minor impact on the total yield. I use $5 \times L_{\text{int}}$ to reduce the statistical uncertainty in the study of the major background components originating from either the tauon pair production or the $q\bar{q}$ process.

3.3 Belle skimming

To isolate an interesting signal from the large data set and to get rid of most of the background events, several data skims are used depending on the physics being

3 Event selection

studied. In this analysis, the relevant Belle physics skims are the TauSkim and the HadronBJ [51]. Here I list definitions and selection criteria from the TauSkim.

The tauon is a short-lived particle, thus a good charged track left by the tauon decay products must originate from the region near the interaction point. The impact parameter is required to be below 2 cm, and the longitudinal coordinate with respect to the interaction point is required to be below 5 cm. Additionally, the transverse momentum, p_{\perp} , is required to be above 100 MeV, such that the charged particle hits enough layers of the SVD and the CDC and the track is properly reconstructed. Further, the tracks are assumed to be left by charged pions.

Good photons are good ECL clusters that are not matched with any charged track. The energy of the good photon must be above 100 MeV.

At an e^+e^- collider the full kinematics of the initial state can be derived from the energy of the beams and the crossing angle of the beams. KEKB is a collider with asymmetric beam energies, thus the laboratory frame of the Belle detector differs from the CMS.

The general TauSkim selection criteria are: the number of good tracks, N_{trk} , is above one and below nine, the sum of good track charges is above minus three and below three, the maximum p_{\perp} of the good charged tracks in the laboratory frame, $\max p_{\perp}$, is above 0.5 GeV, the event vertex is located at the interaction point such that the transverse projection of the distance to the interaction point is below 1 cm and the longitudinal projection of the distance to the interaction point is below 3 cm, the sum of momenta of the good charged tracks and photons in the CMS, $E_{\text{rec, CMS}}^1$, is above 3 GeV or $\max p_{\perp} > 1$ GeV.

In the case $2 \leq N_{\text{trk}} \leq 4$, TauSkim includes additional selection criteria: first, the total energy, $E_{\text{tot}} = E_{\text{rec, CMS}} + |p_{\text{miss, CMS}}|$, is below 9 GeV, or the maximum angle between good tracks is below 175° , or the sum of the energy deposition in the ECL, $E_{\text{ECL, lab}}$, is above 2 GeV and below 9 GeV, and second, the number of good tracks in the barrel region (track polar angle, θ_{trk} : $30^\circ < \theta_{\text{trk}} < 130^\circ$) is above two or the ECL energy of tracks in the center-of-momentum frame, $E_{\text{ECL, trk, CMS}}$, is below 5.3 GeV.

TauSkim requires that the p_{\perp} in the laboratory frame is above 0.1 GeV. This criterion has only a small effect on the detection efficiency: most of the signal tracks have $p_{\perp} > 0.1$ GeV, see Fig. 4.

To avoid double counting of the data events from the HadronBJ and TauSkim skims, a special cut is applied, see [52].

¹Although the sum of momenta would be better to denote as $P_{\text{rec, CMS}}$ I keep here and after the original Belle notation for consistency.

3.4 Definition of good charged tracks and photons

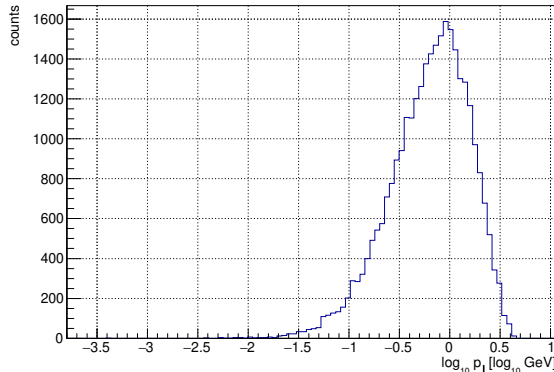


Figure 4: MC Truth distribution of $\log_{10} p_{\perp}$, obtained with the Belle version KKMC.

3.4 Definition of good charged tracks and photons

The good charged track definition from TauSkim is further restricted to reduce the beam background as follows: the impact parameter is below 0.5 cm, the longitudinal coordinate with respect to the interaction point is below 2.5 cm, and the particle's charge is either 1 or -1 . The tracks are assumed to be charged pions.

The good photon definition from TauSkim is further restricted as follows: the photon energy E_{γ} is above 0.04 GeV, the weighted root-mean-square is above 0.5 cm, the number of crystals with the energy deposition above a threshold in the cluster is above 2, and the ratio $E_{\text{seeding crystal}}/E_{\text{cluster}}$ is below 0.95.

3.5 Definition of the thrust vector

Tauons, produced in the $e^+e^- \rightarrow \tau^+\tau^-$ process at a B-factory, have high momenta in comparison with the B-mesons, such that the decay products of each tauon fly within a narrow cone and the cones are oriented almost back to back, while the decay products of the B-meson pair have a more spherical shape. The thrust variable T separates $e^+e^- \rightarrow \tau^+\tau^-$ from $B\bar{B}$ events (see [53]):

$$T = \max_i \frac{\sum_j |(\vec{p}_j, \vec{n}_{\text{thrust}})|}{\sum_j |\vec{p}_j|}, \quad T \in [0, 1], \quad (3.18)$$

where \vec{p}_i is the momentum of the i th charged particle or photon in the CMS. The thrust value is close to unity for the $e^+e^- \rightarrow \tau^+\tau^-$ process and close to 0.6 for the $B\bar{B}$ process.

3 Event selection

The thrust direction \vec{n}_{thrust} splits the event into two hemispheres. The signal hemisphere contains three tracks, while the tag hemisphere may contain one or three tracks.

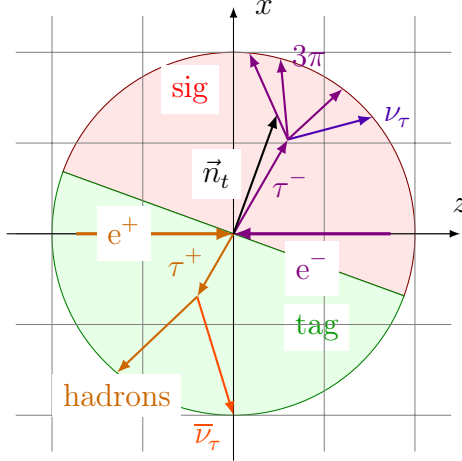


Figure 5: Schematic view of an $e^+e^- \rightarrow \tau^+\tau^-$ event, split with the thrust direction.

The number of tracks contained in each hemisphere defines the topology of the event. In this analysis, I require the 3–1 topology as my baseline selection criterion, having three charged tracks in the signal hemisphere and one charged track in the tag hemisphere, as demonstrated in Fig. 5. The total charge is required to be zero.

A typical $e^+e^- \rightarrow \tau^+\tau^-$ event is shown in Fig. 6, where one tauon decays to three pions, and another tauon decays to an electron. The electron deposits its energy in the calorimeter, which is highlighted with the long pink bar in the top right corner of Fig. 6a, while the pions’ energy depositions in the ECL are relatively low. The electron flies almost back-to-back to the pions due to the boost of the tauons. Also, there is no displaced vertex in this event: all tracks come from the interaction point.

3.6 Event-class boosted decision trees

According to [54] the thrust and the reconstructed energy in the CMS $E_{\text{rec, CMS}}$ as defined in TauSkim separate the $\tau^+\tau^-$ process from the $q\bar{q}$ and the two-photon backgrounds. According to [55] the two-dimensional octagon-shaped cut on the mass and the polar angle of the missing four-momentum separates the $\tau^+\tau^-$ process from the Bhabha scattering and additionally restricts the two-photon processes. These analyses motivate the development of a more sophisticated method of selecting $e^+e^- \rightarrow \tau^+\tau^-$ processes using these four variables.

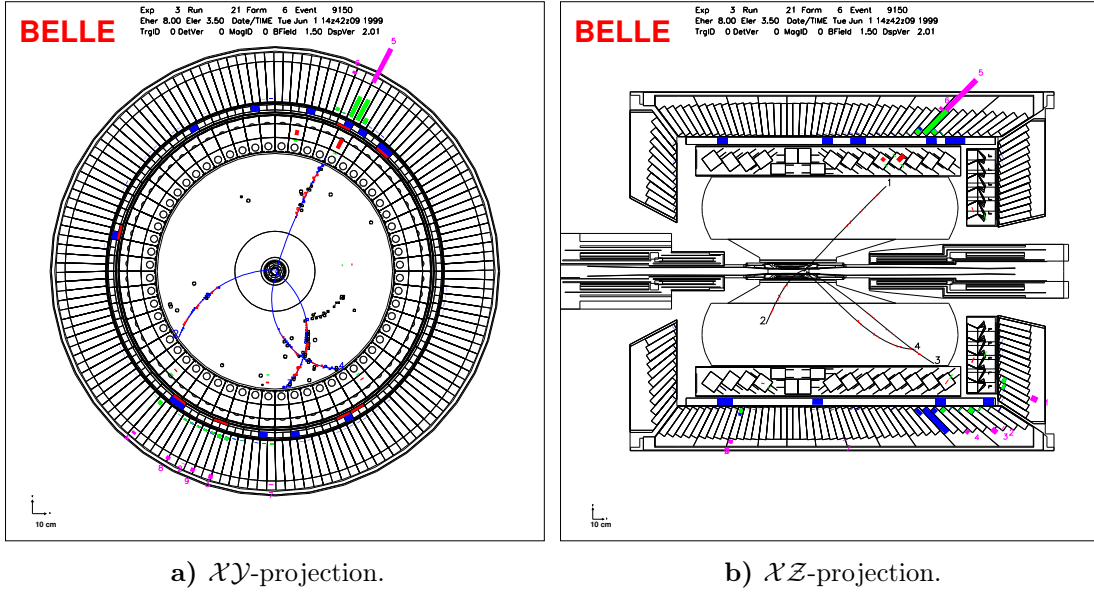


Figure 6: Belle event display.

To increase the efficiency and the purity for the $e^+e^- \rightarrow \tau^+\tau^-$ process, one can exploit correlations between the variables in a multivariate data analysis approach, such as the boosted decision trees (BDT). The BDT produces an output, the BDT response, which is the weighted average of weakly learning decision trees. In this analysis, the ROOT Toolkit for Multivariate Data Analysis is used [56] to train the Adaptive BDT and to evaluate its output.

The following variables are used for training and BDT response evaluation: thrust, sum of momenta in the CMS frame, $E_{\text{rec, CMS}}$, as defined in TauSkin, the mass and the cosine of the polar angle of the missing four-momentum in the CMS, the sum of cluster energies in the laboratory frame, $E_{\text{ECL, Lab}}$, as defined in TauSkin, and the sum of track energies in the CMS, $E_{\text{ECL, trk, CMS}}$, as defined in TauSkin.

One-dimensional distributions of these six variables are shown in Fig. 7. In the $E_{\text{rec, CMS}}$ distribution, the background from two-photon processes peaks at 3 GeV and about 10.25 GeV, while the $e^+e^- \rightarrow \tau^+\tau^-$ process peaks at 6 GeV. In the thrust distribution, there is a clear background peak at unity corresponding to the Bhabha process, also the background distribution has a broad structure peaking at 0.87 while the $e^+e^- \rightarrow \tau^+\tau^-$ process has a narrow structure and peaks at 0.95. In the $E_{\text{ECL, Lab}}$ distribution, the background has a broad structure and peaks at 6 GeV, while the $e^+e^- \rightarrow \tau^+\tau^-$ process has a slightly narrower structure and peaks at 3.2 GeV. The $E_{\text{ECL, trk, CMS}}$ variable looks similar for both background

3 Event selection

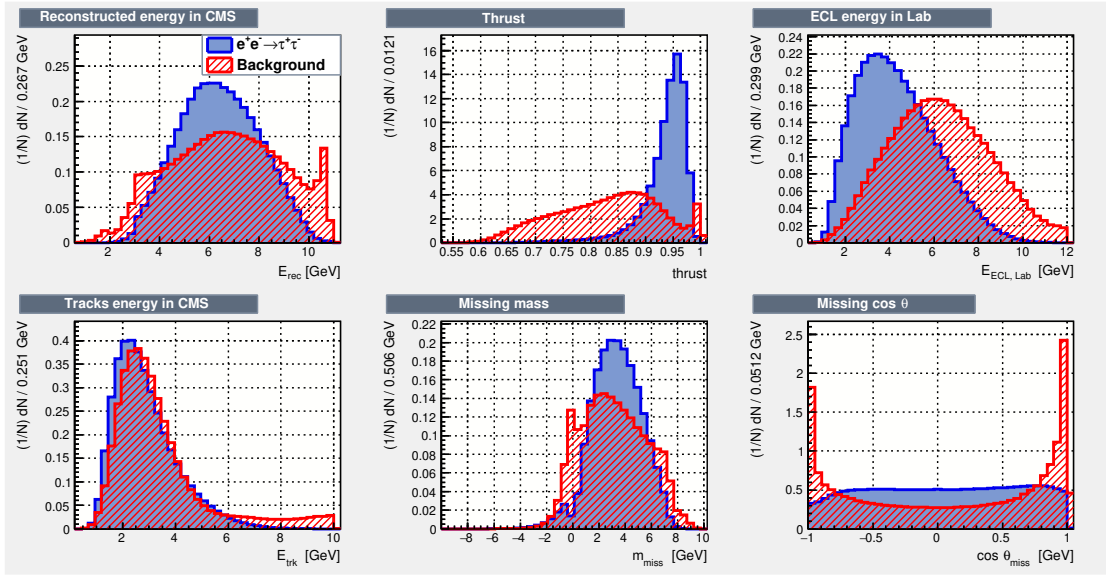


Figure 7: Input variables for the event-class BDT. The Solid blue line shows the $e^+e^- \rightarrow \tau^+\tau^-$ process, and the hatched red line shows the total of the rest processes. The top left figure shows the $E_{\text{rec, CMS}}$ distribution, the top middle figure shows the thrust distribution, the top right figure shows the $E_{\text{ECL, Lab}}$ distribution, the bottom left figure shows the $E_{\text{ECL, trk, CMS}}$ distribution, the bottom middle and right figures show the distributions of the mass and the cosine of the polar angle of the missing four-momentum in the center-of-momentum frame.

and for the $e^+e^- \rightarrow \tau^+\tau^-$ process. In the distributions of the mass and the cosine of the polar angle of the missing four-momentum in the CMS, one can see the peaking QED background at zero mass and in the forward and backward directions ($|\cos\theta| \approx 1$), while the $e^+e^- \rightarrow \tau^+\tau^-$ process peaks at 3 GeV and -1 GeV in the mass distribution and has almost flat behavior in the cosine of the polar angle distribution.

Correlation matrices of the input variables are shown in Fig. 8. For background Fig. 8b, there is strong correlation between the $E_{\text{rec, CMS}}$, thrust, $E_{\text{ECL, Lab}}$, and $E_{\text{ECL, trk, CMS}}$ variables, while for the $e^+e^- \rightarrow \tau^+\tau^-$ process in Fig. 8a there is no such strong correlation. For both $e^+e^- \rightarrow \tau^+\tau^-$ and background processes, the mass of the missing four-momentum in the CMS anti-correlates with the thrust.

The BDT needs to be trained and tested on statistically independent samples. In this analysis, I use a simulated data sample corresponding to $L_{\text{int}} = 67 \text{ fb}^{-1}$ for $e^+e^- \rightarrow \tau^+\tau^-$, $q\bar{q}$, $B\bar{B}$, $e^+e^- \rightarrow \gamma^*\gamma^*$, $\mu^+\mu^-$ processes and $L_{\text{int}} = 35 \text{ fb}^{-1}$ for the Bhabha process. The yield of the Bhabha process is rescaled according to the integrated luminosity. The sample is evenly split for training and testing. The

3.6 Event-class boosted decision trees

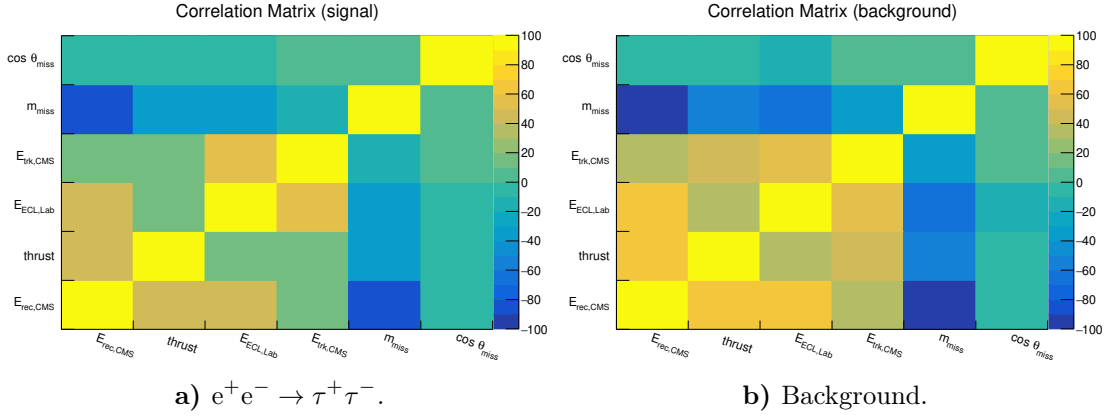


Figure 8: Correlation matrices for $e^+e^- \rightarrow \tau^+\tau^-$ (left) and background (right). The range of the color scale is $[-100\%, 100\%]$.

BDT is trained such that the $e^+e^- \rightarrow \tau^+\tau^-$ process including all tauon decay modes is considered signal, and the rest background.

The separation power of an input variable y is defined as follows:

$$\frac{1}{2} \int \frac{(S(y) - B(y))^2}{S(y) + B(y)} dy, \quad (3.19)$$

where $S(y)$ is the signal probability density function (PDF), and $B(y)$ is the background PDF. The separation power is zero if the signal shape matches the background one, and is unity if there is no overlap between signal and background. The separation power of the six variables is shown in Table 3. The thrust variable has the largest separation power, while $E_{\text{ECL, trk, CMS}}$ has the least separation power.

Rank	Variable	Separation
1	thrust	0.2529
2	$\cos \theta_{\text{miss}}$	0.1575
3	$E_{\text{rec, CMS}}$	0.1550
4	$E_{\text{ECL,lab}}$	0.1542
5	m_{miss}	0.1530
6	$E_{\text{trk, CMS}}$	0.1273

Table 3: Event-class BDT ranking of variables after training.

After training a BDT, one needs to ensure on a test sample that there is no over-training. Fig. 9a shows the histograms of the BDT response for signal and background for both training and test samples. The BDT response lies in the

3 Event selection

$[-0.7, 0.5]$ range, the signal peaks at 0.2 and the background peaks at -0.25 . The Kolmogorov-Smirnov test first described in [57] is performed separately for signal and background by comparing the BDT response histogram for the training and test samples. The over-training test score is 0.626 for signal and 0.612 for background.

The receiver operator characteristic (ROC) curve is shown in Fig. 9b. It demonstrates how background rejection reduces with the increase of the efficiency relative to the 3–1 baseline selection. One can achieve 92% background rejection with 90% of the relative signal efficiency.

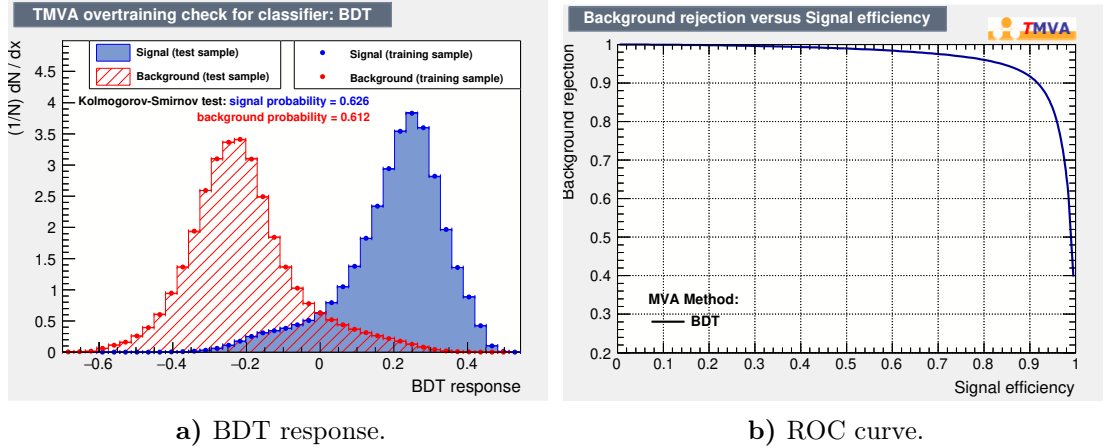


Figure 9: Left: the BDT response distribution for the signal and background for the test and training samples. Right: the background rejection versus the tau-pair relative efficiency.

The BDT response for different background components is shown in Fig. 10a. One can see that the largest background component is the $q\bar{q}$ process for almost any selection criterion on the BDT response.

Fig. 10b compares the BDT ROC curve against the ROC curve obtained for the one-dimensional cut on the thrust value. In this plot, both purity and efficiency are evaluated considering $\tau^- \rightarrow \pi^- \pi^- \pi^+ \nu_\tau$ as signal and not $e^+ e^- \rightarrow \tau^+ \tau^-$. The BDT-based approach shows higher efficiency for the same purity, and higher purity for the same efficiency. Moreover, the BDT-based approach reaches purity above 90%, while the cut on the thrust value can reach at maximum only 89% of purity.

To speed up the processing of data, additional selection criteria are required before applying BDT: $E_{\text{ECL, Lab}} < 12$ GeV, $E_{\text{rec, CMS}} < 11$ GeV, and $E_{\text{ECL, trk, CMS}} < 10$ GeV. Table 4 shows numbers of events for a test sample of simulated data before any selection, after the BDT preselection, and after requiring the 3–1 topology. The BDT preselection criteria reduce the baseline signal efficiency by 3×10^{-3} .

3.7 Backgrounds from the tauon decays

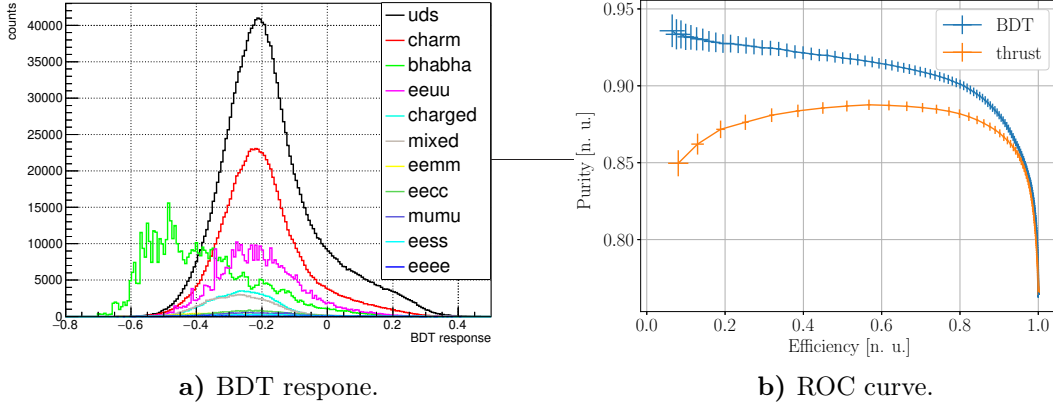


Figure 10: Left: the BDT response for the background components. Right: ROC curves of the event class BDT (blue) in comparison with threshold on thrust (orange). Here, purity calculated for the signal $\tau^- \rightarrow \pi^- \pi^- \pi^+ \nu_\tau$ efficiency is shown relative to the baseline selection; in normalized units (n. u.).

process	processed	preselected for BDT	3-1 topology
$\tau^+ \tau^-$	16286654	16221625	2291243
$q\bar{q}$	57716100	57132558	2338973
QED	827832728	294437546	1004895
$B\bar{B}$	18556968	18430463	251384

Table 4: Number of events for the 3-1 topology selection (baseline selection).

The event-class BDT response $b_{\tau\tau}$ is evaluated after the 3-1 topology requirement. The selection criterion on the $b_{\tau\tau}$ is optimized by finding the maximum of the figure-of-merit,

$$\frac{S}{\sqrt{S+B}}, \quad (3.20)$$

where S is the signal yield and B is the background yield. The figure-of-merit reaches maximum if $b_{\tau\tau} > 0$.

3.7 Backgrounds from the tauon decays

So far we have discussed only how to separate $e^+e^- \rightarrow \tau^+\tau^-$ process from other processes. Now we need to reduce the background of tauon decays.

The signal hemisphere tracks are required to satisfy the following particle identification (PID) conditions: the binary likelihood of a charged particle to be an

3 Event selection

electron against to be a pion, \mathcal{P}_e , is required to be below 0.9, and the binary likelihood of a charged particle to be a muon against to be a pion, \mathcal{P}_μ , is required to be below 0.9. For tracks with the same charge, I require the binary likelihood for a charged track to be a kaon against to be a pion, \mathcal{P}_K , to be below 0.9. This reduces the $\tau \rightarrow K\pi\pi\nu_\tau$ background.

The phase-space allowed region of $\tau^- \rightarrow \pi^- \pi^- \pi^+ \nu_\tau$ is selected by requiring the invariant mass of three pions, $m_{3\pi}$, to be below the nominal mass of the tauon, $m_\tau = 1.77686$ GeV. Also, invariant masses of all combinations of two pions, $m_{2\pi}$, are required to be above two nominal masses of the charged pion, $2m_\pi = 279.14$ MeV.

The angle between three pions and the tauon, $\cos\psi$, is required to be in the physical range $|\cos\psi| < 1$.

The $\tau \rightarrow K^0\pi\nu_\tau$ process is not a subject of this analysis because it has a different decay amplitude, therefore it needs to be removed. To reduce the K^0 contamination I place a requirement on m_{13} and m_{23} in the signal hemisphere outside of the 1.5-standard-deviation window around the nominal K^0 mass:

$$\left| m_{2\pi} - m_{K^0} \right| > 12 \text{ MeV}. \quad (3.21)$$

The standard deviation is obtained from the simulated data by fitting with a Gaussian function to the $m_{2\pi}$ distribution of the $\tau \rightarrow K^0\pi\nu_\tau$ process.

The π^0 -veto is applied: a cut on the sum of good photon energies in the laboratory frame from the signal hemisphere $\sum E_{\gamma,\text{sig}}$. After optimizing the figure-of-merit from Eq. (3.20), the obtained selection criterion is used: $E_{\gamma,\text{sig}} < 0.48$ GeV.

Purity and efficiency for selection criteria applied sequentially are shown in Table 5; Table 13 in Appendix A shows in more details the number of selected events for the signal and for some background processes.

Criterion	purity in %	efficiency in %
baseline	22.2	50.5
skimming	24.5	43.1
BDT	50.6	39.9
PID	57.4	36.7
phase space	58.2	35.9
K^0 -veto	60.7	34.3
π^0 -veto	81.6	32.3

Table 5: Sequential purity and efficiency. The PID row combines lepton and hadron particle identification, the phase space row combines selection criteria on $m_{3\pi}$, m_{23} , m_{13} , m_{12} , and $\cos\psi$.

3.7 Backgrounds from the tauon decays

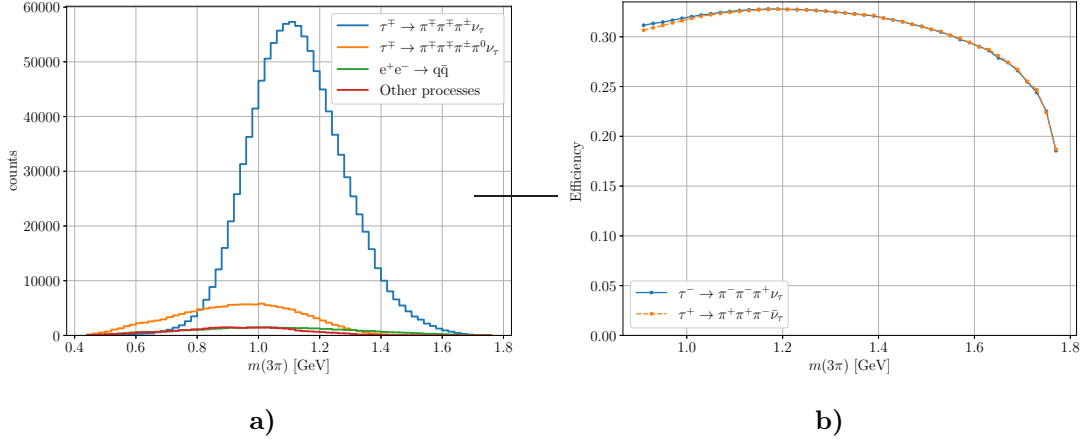


Figure 11: Fig. a shows $m_{3\pi}$ histograms after applying all selection criteria to the generic MC, The blue line shows the $\tau^- \rightarrow \pi^- \pi^- \pi^+ \nu_\tau$ process, the orange line shows the $\tau^- \rightarrow \pi^- \pi^- \pi^+ \pi^0 \nu_\tau$ process, the green line shows the $q\bar{q}$ process, and the red line shows all other backgrounds. $L_{\text{int}} = 20 \text{ fb}^{-1}$. Fig. b shows the signal efficiency as a function of $m_{3\pi}$. The blue line shows the efficiency for $\tau^- \rightarrow \pi^- \pi^- \pi^+ \nu_\tau$, and the orange line shows the efficiency for $\tau^+ \rightarrow \pi^+ \pi^+ \pi^- \bar{\nu}_\tau$.

The resulting histogram of $m_{3\pi}$ in Fig. 11a shows that the major background components are $\tau^- \rightarrow \pi^- \pi^- \pi^+ \pi^0 \nu_\tau$ for $m_{3\pi} < 1.3 \text{ GeV}$ and $q\bar{q}$ for $m_{3\pi} > 1.3 \text{ GeV}$. The signal region is defined to be above 0.9 GeV, where the expected number of events for the signal process is at least twice as large as for the sum of the background processes. For this signal region the background contamination is 13%, which is still large for a typical PWA, thus the background shape must be modeled properly beforehand. Otherwise, it will leak into the partial waves, distorting their amplitudes and phases.

Fig. 11b shows how efficiency depends on $m_{3\pi}$ in the signal region. For low $m_{3\pi}$ values one can see a small charge asymmetry due to the detector effects. Efficiency drops with $m_{3\pi}$ getting closer to the tauon mass. In the region where one expects to observe the $a_1(1260)$ and $a_1(1420)$ peaks there is no sharp behavior of the efficiency function.

4 Background shape parametrization

Because of the complicated dynamic structure of the major background components and because the detector acceptance for these components is not known, a physical model cannot be adopted for these components in the PWA. I have adopted a neural-network method of background description developed in [58] for the $\tau^- \rightarrow \pi^- \pi^- \pi^+ \nu_\tau$ analysis.

The neural network is an analytical PDF $w(\Phi)$ of phase-space variables Φ . $w(\Phi)$ is defined like in [58] as follows:

$$w(\Phi) = \ln \left(1 + \exp \left[\left\{ \prod_{i=0}^h D \circ A_i \right\} \vec{\Phi} \right] \right), \quad (4.1)$$

where A_i are real-valued matrices, \circ denotes the element-wise action, and $D(x)$ is a non-linear smooth function.

The matrices A_i transform real-valued vectors, the layers of the neural network. The input layer is the vector of the phase-space variables $\vec{\Phi}$. The output layer is the value of the neural network $w(\Phi)$. The remaining layers are called the hidden layers, and h is the number of hidden layers. A_0 connects the input layer of the neural network with that of the phase-space variables $\vec{\Phi}$, with the first hidden layer $\vec{\Lambda}_1$, such that

$$\vec{\Lambda}_1 = D \circ A_0 \vec{\Phi}. \quad (4.2)$$

Λ_1 is a vector of dimension W .

A_h connects the last hidden layer $\vec{\Lambda}_h$ with the output layer,

$$\vec{\Lambda}_h = A_h \vec{\Lambda}_h. \quad (4.3)$$

$\dim A_0 = W \times \dim \vec{\Phi}$, $\dim A_h = 1 \times W$, $\dim A_i = W \times W$ for $i \in [1, h - 1]$.

$D(x)$ is a smooth non-linear function,

$$D(x) \approx \frac{x}{2} \left\{ 1 + \operatorname{tgh} \left[\sqrt{\frac{2}{\pi}} (x + 0.044715x^3) \right] \right\}, \quad (4.4)$$

where tgh denotes the hyperbolic tangent function.

4 Background shape parametrization

The objective of the training procedure is to optimize the parameters of the neural network by finding the maximum of the logarithm likelihood,

$$\ln \mathcal{L}_{\text{neural network}} = \sum_i \ln w - k \ln \mathcal{N}_{\text{bcg}}, \quad (4.5)$$

where k is the number of simulated background events, i sums over the accepted background events in the simulation, and \mathcal{N}_{bcg} is the normalizing constant of background,

$$\mathcal{N}_{\text{bcg}} = \mathbf{E}[w], \quad (4.6)$$

where \mathbf{E} denotes the average over the phase space Φ . Due to the large number of parameters, a gradient descent approach is not feasible in this case, and a stochastic gradient-based optimizer is used instead [59].

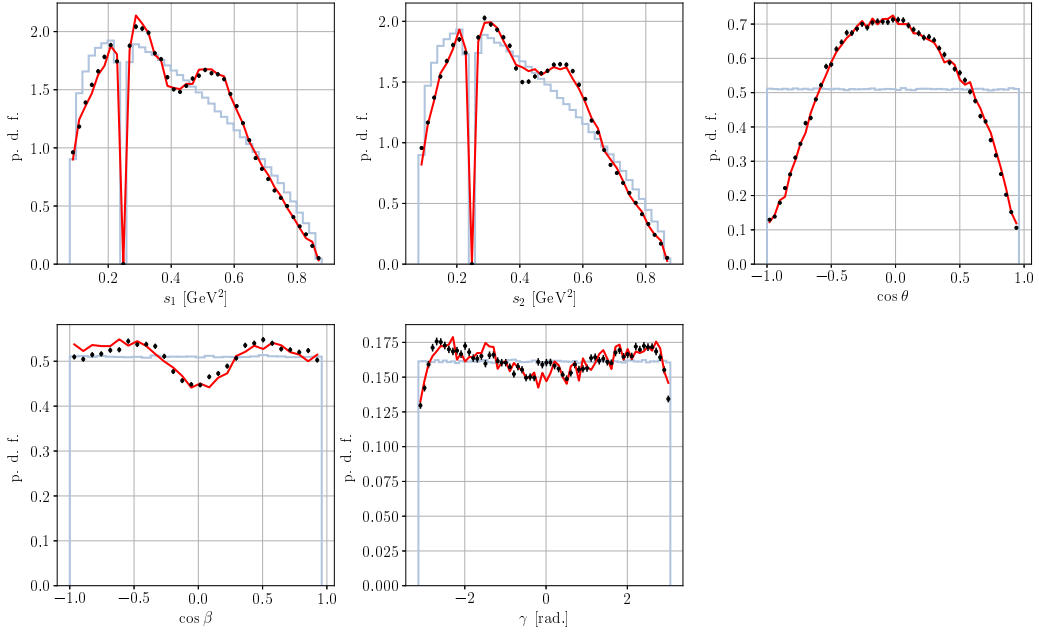


Figure 12: Neural network example: one-dimensional projections of w (red) versus the simulated background (black dots with error bars). The faint blue line shows how three pions phase space projects on the variables. The top row depicts from left to right s_1 , s_2 , and $\cos \theta$ phase-space variables. The bottom row depicts from left to right $\cos \beta$ and γ phase-space variables.

Despite the recent progress in machine learning studies, some training details cannot be obtained analytically from first principles, and must be studied empirically. In $\tau^- \rightarrow \pi^- \pi^- \pi^+ \nu_\tau$ the neural network configuration taken from [58] shows notable discrepancy from the simulated background. Instead of increasing

the complexity of the neural network by adding more hidden layers and increasing W , I found that training multiple neural networks in bins of $m_{3\pi}$ works reasonably well with the neural-network configuration close to [58]: $\dim \vec{\Phi} = 5$, $h = 3$, $W = 40$, and Adam optimizer step size is 10^{-4} . For better convergence, variables s_1 and s_2 are centered around zero. All these parameters were found empirically after series of trials.

$w(\Phi)$ for $m_{3\pi} \in [1.06, 1.08]$ GeV is illustrated in Fig. 12: shown are one-dimensional histograms. The background has a two-peak structure in the s_1 and s_2 variables with a dip at approximately 0.25 GeV^2 corresponding to the K^0 -veto from the selection criteria. The background shows strong dependence on the $\cos \theta$ variable, and weak but notable dependence on the $\cos \beta$ and γ variables. The flat phase space is notably different from the background, while the neural network prediction shows good agreement with the simulated background for all five phase space variables.

5 Partial-wave analysis

Tauons decay to three pions via intermediate quantum states that interfere with each other. In the isobar model, this decay is seen as a cascade of two-body decays,

$$\tau^- \rightarrow X^- \nu_\tau, \quad X^- \rightarrow \pi^- \xi^0, \quad \text{and} \quad \xi^0 \rightarrow \pi^- \pi^+, \quad (5.1)$$

where X^- denotes a three-pion resonance such as $a_1(1260)$ or $\pi(1300)$, and ξ^0 denotes an isobar, which is a two-pion resonance such as $\rho(770)$ or $f_0(980)$. Conventional PWA includes two stages: partial-wave decomposition and a three-pion resonance-model fit. Partial-wave decomposition extracts partial-wave amplitudes from an input data set in bins of $m_{3\pi}$. The $\tau^- \rightarrow \pi^- \pi^- \pi^+ \nu_\tau$ differential decay rate is used:

$$d\Gamma = |\mathcal{M}|^2 d\Phi, \quad (5.2)$$

where \mathcal{M} is the $\tau^- \rightarrow \pi^- \pi^- \pi^+ \nu_\tau$ matrix element, and $d\Phi$ is the phase space volume element. Decomposed partial-wave amplitudes serve as an input into the resonance-model fit, which finds parameters of the three-pion resonances.

In the conventional PWA approach there is no *a priori* assumption on the shape of the dynamic amplitudes of the three-pion resonances as functions of $m_{3\pi}$. However, there is model dependence in the isobar parametrizations as functions of $m_{2\pi}$. To bypass this limitation of conventional PWA, authors of [60] developed a freed-isobar PWA method where isobar parametrization is learned from data directly. To perform a resonance-model fit on the freed-isobar PWA output, one needs to insert an additional intermediate step, the isobar fit, which extracts the partial-wave amplitudes under some model assumption.

5.1 Phase space volume $d\Phi$

Euler angles α, β, γ , helicity angle θ , and squared invariant masses q^2, s_1 , and s_2 fully describe the kinematics of $\tau^- \rightarrow \pi^- \pi^- \pi^+ \nu_\tau$. The phase space volume after integrating over Euler angle α is

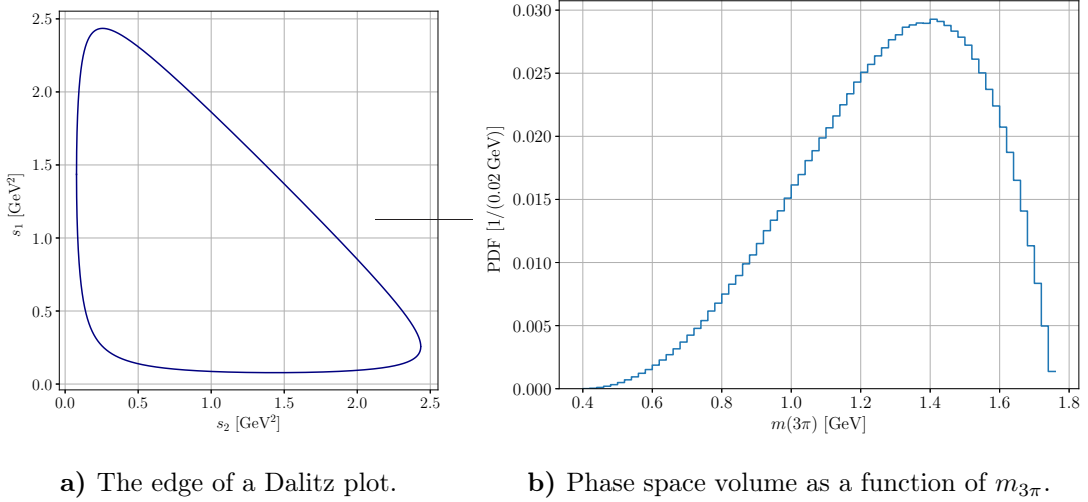
$$d\Phi = \frac{1}{(2\pi)^5} \frac{1}{64} \frac{m_\tau^2 - q^2}{m_\tau^2} \frac{dq^2}{q^2} ds_1 ds_2 \frac{d \cos \beta}{2} \frac{d\gamma}{2\pi} \frac{d \cos \theta}{2}. \quad (5.3)$$

5 Partial-wave analysis

To restore the $d\alpha$ dependence in Eq. (5.3), one needs to multiply it by

$$\frac{d\alpha}{2\pi}. \quad (5.4)$$

The phase space is uniform in α , $\cos\beta$, γ , $\cos\theta$, and on the kinematically allowed two-dimensional region of s_1 and s_2 , the Dalitz plot [61]. The edge of the Dalitz plot can be evaluated analytically and is shown in Fig. 13a for $m_{3\pi} = 1.7$ GeV.



a) The edge of a Dalitz plot.

b) Phase space volume as a function of $m_{3\pi}$.

Figure 13: Mass variables s_1 , s_2 , and $m_{3\pi}$. Fig. 13a shows the Dalitz plot edge for $m_{3\pi} = 1.7$ GeV, Fig. 13b shows $\Phi(m_{3\pi})$.

Fig. 13b shows how the phase space volume depends on $m_{3\pi} \equiv \sqrt{q^2}$ after integrating over all other phase space variables. The phase space is zero if $m_{3\pi} < 3m_\pi = 419$ MeV. For $419 \text{ MeV} < m_{3\pi} < 1.4$ GeV, the phase space volume increases with the Dalitz plot area. Above 1.4 GeV, it decreases with the

$$\frac{m_\tau^2 - q^2}{q^2} \quad (5.5)$$

factor. Above m_τ , the phase space is zero.

5.2 Matrix element of $\tau^- \rightarrow \pi^- \pi^- \pi^+ \nu_\tau$

PWA requires knowing how to evaluate the differential decay rate of $\tau^- \rightarrow \pi^- \pi^- \pi^+ \nu_\tau$. The decay rate formula in Eq. (5.2) consists of two ingredients: the phase space in Eq. (5.3) and the matrix element. To develop the matrix element, we first investigate how the tauon decays to three pions in the Standard Model.

5.3 Lepton tensor decomposition

In the Standard Model, $\tau^- \rightarrow \pi^- \pi^- \pi^+ \nu_\tau$ occurs via the hadronization of $d\bar{u}$ quarks in the $\tau^- \rightarrow \nu_\tau d\bar{u}$ process via W^- exchange. The $\tau^- \rightarrow \nu_\tau d\bar{u}$ process is represented schematically in Fig. 14.

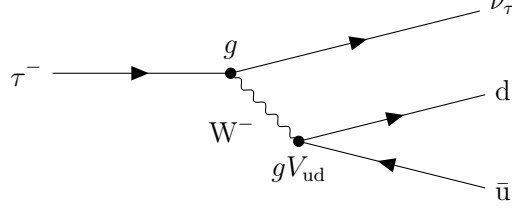


Figure 14: Diagram for the $\tau^- \rightarrow \nu_\tau d\bar{u}$ process.

In the $m_\tau^2/m_W^2 \approx 0$ approximation, the matrix element from Eq. (5.2) takes the following form [62, 63]:

$$\mathcal{M} = \frac{G_F}{\sqrt{2}} V_{ud} \underbrace{\langle \nu_\tau | \bar{u}(l') \gamma^\mu (1 - \gamma^5) u(l) | \tau \rangle}_{\text{lepton current}} \underbrace{\langle \pi^- \pi^- \pi^+ | J_{\text{had},\mu} | 0 \rangle}_{\text{hadron current}}, \quad (5.6)$$

where G_F is the Fermi coupling constant, V_{ud} is the element of the Cabibbo-Kobayashi-Masukawa matrix that connects up and down quarks, l and l' are τ^- and ν_τ four-momenta respectively, and $\langle \pi^- \pi^- \pi^+ | J_{\text{had},\mu} | 0 \rangle$ is the hadron current.

The differential decay rate $d\Gamma$ of $\tau^- \rightarrow \pi^- \pi^- \pi^+ \nu_\tau$ is the product of the phase space volume and the square of the matrix element, averaged over the tauon spin states and summed over the final states:

$$d\Gamma = |\mathcal{M}|^2 d\Phi = \frac{G_F^2}{4m_\tau} |V_{ud}|^2 \mathfrak{L}^{\mu\nu} \mathfrak{H}_{\mu\nu} d\Phi, \quad (5.7)$$

where the lepton tensor $\mathfrak{L}^{\mu\nu}$ is the outer product of the lepton current, and the hadron tensor $\mathfrak{H}^{\mu\nu}$ is the outer product of the hadron current.

5.3 Lepton tensor decomposition

The lepton tensor can be decomposed with respect to the tauon polarization:

$$\mathfrak{L}^{\mu\nu} = \mathfrak{L}_{\text{pol-indep.}}^{\mu\nu} + \mathfrak{L}_{\text{pol-dep.}}^{\mu\nu}. \quad (5.8)$$

From [62],

$$\mathfrak{L}_{\text{pol-indep.}}^{\mu\nu} = \{l, l'\}^{\mu\nu} - 4i e_\tau \varepsilon^{\alpha\beta\mu\nu} l'_\alpha l_\beta, \quad (5.9)$$

$$\mathfrak{L}_{\text{pol-dep.}}^{\mu\nu} = 4i e_\tau m_\tau \varepsilon^{\alpha\beta\mu\nu} l'_\alpha s_\beta + 4e_\tau m_\tau \{s, l'\}^{\mu\nu}. \quad (5.10)$$

5 Partial-wave analysis

In the above,

$$\{p, q\} \equiv p^\mu q^\nu + q^\mu p^\nu - g^{\mu\nu} p_\sigma q^\sigma \quad (5.11)$$

for arbitrary four-vectors p and q , $g^{\mu\nu}$ is the Minkowsky metric tensor,

$$g^{\mu\nu} = \text{diag}(1, -1, -1, -1), \quad (5.12)$$

and $\varepsilon^{\alpha\beta\mu\nu}$ is the covariant Levi-Civita tensor with

$$\varepsilon^{0123} = 1. \quad (5.13)$$

e_τ is the tauon electric charge, and s^μ is the tauon polarization four-vector with the following properties:

$$s_\mu s^\mu = -P^2, \quad (5.14)$$

$$|P| \leq 1, \quad (5.15)$$

$$s_\mu l^\mu = 0. \quad (5.16)$$

For the nominal analysis, I assume that the tauon is depolarized; thus

$$\mathfrak{L}_{\text{pol-dep.}}^{\mu\nu} = 0 \quad (5.17)$$

5.4 Lepton tensor averaging over the tauon direction

The Euler angle α is immeasurable at Belle. Therefore, the lepton tensor is integrated over α .

For an arbitrary spatial vector \vec{p} in the hadron rest frame, Euler rotation can be written as:

$$\hat{\mathbb{R}} = \begin{pmatrix} \cos \gamma & \sin \gamma & 0 \\ -\sin \gamma & \cos \gamma & 0 \\ 0 & 0 & 1 \end{pmatrix} \begin{pmatrix} \cos \beta & 0 & -\sin \beta \\ 0 & 1 & 0 \\ \sin \beta & 0 & \cos \beta \end{pmatrix} \begin{pmatrix} \cos \alpha & \sin \alpha & 0 \\ -\sin \alpha & \cos \alpha & 0 \\ 0 & 0 & 1 \end{pmatrix} \quad (5.18)$$

$\mathfrak{L}^{\mu\nu}$ is a bilinear combination of l^μ and l'^μ , thus the lepton tensor can be rewritten as a function of α as follows:

$$\mathfrak{L}_{\mu\nu}^{\alpha,0} + \mathfrak{L}_{\mu\nu}^{\alpha,1,s} \sin \alpha + \mathfrak{L}_{\mu\nu}^{\alpha,1,c} \cos \alpha + \mathfrak{L}_{\mu\nu}^{\alpha,1,sc} \sin \alpha \cos \alpha \quad (5.19)$$

$$+ \mathfrak{L}_{\mu\nu}^{\alpha,2,s} \sin^2 \alpha + \mathfrak{L}_{\mu\nu}^{\alpha,2,c} \cos^2 \alpha, \quad (5.20)$$

where $\mathfrak{L}_{\mu\nu}^{\alpha,i}$ can be interpreted as Fourier-series coefficients, i can be 0, 1, s , 1, c , 1, sc , 2, s , and 2, c .

5.4 Lepton tensor averaging over the tauon direction

Integrating $\mathfrak{L}_{\mu\nu}$ with respect to α on the interval $[0, 2\pi)$ gives the averaged spatial coordinates of the lepton tensor:

$$\bar{\mathfrak{L}}_{ij}(\dots) = \mathfrak{L}_{ij}^{\alpha,0} + \frac{1}{2} \mathfrak{L}_{ij}^{\alpha,2,s} + \frac{1}{2} \mathfrak{L}_{ij}^{\alpha,2,c}. \quad (5.21)$$

Meanwhile, \mathfrak{L}_{00} stays the same after averaging, because it does not depend on α . \mathfrak{L}_{i0} and \mathfrak{L}_{0i} stay the same after averaging as well, because these terms depend only linearly on either $\sin \alpha$ or $\cos \alpha$, and after integration the linear terms vanish.

The same averaging procedure can be applied in any frame, for example, in the CMS. This requires us first to construct three orthonormal vectors,

$$\hat{i} = \hat{q}, \quad (5.22)$$

$$\hat{j} = \frac{\hat{q} \times \hat{\mathcal{Z}}}{|\hat{q} \times \hat{\mathcal{Z}}|}, \quad (5.23)$$

$$\hat{k} = \frac{\hat{q} \times \hat{j}}{|\hat{q} \times \hat{j}|}, \quad (5.24)$$

where

$$\hat{\mathcal{Z}} \equiv (0, 0, 1). \quad (5.25)$$

Then, three tauon four-vectors are constructed:

$$l_{\parallel}^{\mu} = (E_{\tau}, \hat{i} |p_{\tau}| \cos \Theta), \quad (5.26)$$

$$l_{\perp,1}^{\mu} = (0, \hat{j} |p_{\tau}| \sin \Theta), \quad (5.27)$$

$$l_{\perp,2}^{\mu} = (0, \hat{k} |p_{\tau}| \sin \Theta), \quad (5.28)$$

where E_{τ} and $|p_{\tau}|$ were given in Eq. (3.13), $\cos \Theta$ was given in Eq. (3.14), and

$$\sin \Theta = \sqrt{1 - \cos^2 \Theta}. \quad (5.29)$$

Three tau neutrino four-vectors are derived from three tauon four-vectors as follows:

$$l'_{\parallel}{}^{\mu} = l_{\parallel}^{\mu} - q^{\mu}, \quad (5.30)$$

$$l'_{\perp,1\text{or}2}{}^{\mu} = l_{\perp,1\text{or}2}^{\mu}. \quad (5.31)$$

The averaged lepton tensor is constructed as follows:

$$\bar{\mathfrak{L}}^{\mu\nu} = \mathfrak{L}_{\parallel}^{\mu\nu} + \frac{1}{2} \mathfrak{L}_{\perp,1}^{\mu\nu} + \frac{1}{2} \mathfrak{L}_{\perp,2}^{\mu\nu}, \quad (5.32)$$

where $\mathfrak{L}_X^{\mu\nu}$ are constructed by substituting tauon and tau neutrino four-momenta from Eqs. (5.8) to (5.10) with l_X^{μ} and $l'_X{}^{\mu}$, where X stands for either \parallel , \perp , 1, or \perp , 2.

5.5 Partial-wave decomposition

While the Standard Model fully predicts the lepton current, it does not fully predict the hadron current. In the isobar model, the $\tau^- \rightarrow \pi^- \pi^- \pi^+ \nu_\tau$ decay occurs via a cascade of two-body decays as shown in Eq. (5.1). The first two-body decay of the cascade,

$$\tau^- \rightarrow \nu_\tau X^-, \quad (5.33)$$

is fully determined with the Standard Model lepton current and q^2 . The rest,

$$X^- \rightarrow \pi^- \xi^0, \quad \xi^0 \rightarrow \pi^- \pi^+, \quad (5.34)$$

corresponds to the hadron current, which is decomposed into partial waves. Fig. 15 depicts the hadronization of $d\bar{u}$ quarks to $\pi^- \pi^- \pi^+$ via the cascade decay.

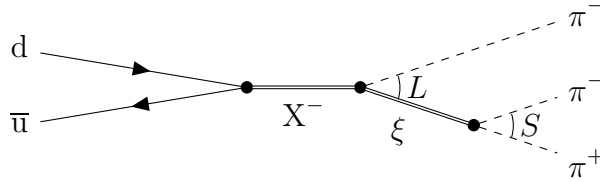


Figure 15: Hadronization of $d\bar{u}$ quarks into $\pi^- \pi^- \pi^+$ in the isobar model.

The partial-wave decomposition of the hadron current is the linear combination of a set of partial waves j_w^μ corresponding to a definite angular momentum L between an isobar ξ^0 and a bachelor pion.

$$J_{\text{had}}^\mu = \sum_w \mathcal{C}_w j_w^\mu, \quad (5.35)$$

where w denotes a partial-wave index in Table 6, and \mathcal{C}_w denotes a complex amplitude of the partial-wave. The partial-wave decomposition accesses not only the dynamic structure of the intermediate resonances, as in a Dalitz plot analysis, but also their spin structures via angular distributions.

In conventional PWA, the notation for a single partial wave w with quantum numbers J^P of a resonance X^- , ξ^0 , and with L between ξ^0 and a bachelor pion, is

$$J^P[\xi^0 \pi]_L. \quad (5.36)$$

In freed-isobar PWA, a freed isobar has only quantum numbers $S^{\tilde{P}\tilde{C}}$,

$$J^P[S^{\tilde{P}\tilde{C}} \pi]_L, \quad (5.37)$$

where S , \tilde{P} , and \tilde{C} stand for the spin, parity, and the C -parity of the isobar.

5.6 Spin structure of $\tau^- \rightarrow \pi^- \pi^- \pi^+ \nu_\tau$: hadron form-factor

Partial wave	Threshold [GeV]
$1^+ [\sigma\pi]_P$	—
$1^+ [f_0(980)\pi]_P$	1.14
$1^+ [f_0(1500)\pi]_P$	1.24
$1^+ [\rho(770)\pi]_S$	—
$1^+ [\rho(1450)\pi]_S$	1.18
$1^+ [\rho(770)\pi]_D$	—
$1^+ [\rho(1450)\pi]_D$	1
$1^+ [f_2(1270)\pi]_P$	1.1
$1^+ [f_2(1270)\pi]_F$	1.06
$0^- [\sigma\pi]_S$	—
$0^- [f_0(980)\pi]_S$	1.14
$0^- [\rho(770)\pi]_P$	—
$0^- [f_2(1270)\pi]_D$	1
$1^- [\omega(782)\pi]_P$	—
$1^- [\rho(770)\pi]_P$	0.96
$1^- [f_2(1270)\pi]_D$	0.9

Table 6: Set of conventional partial waves of the $\tau^- \rightarrow \pi^- \pi^- \pi^+ \nu_\tau$ process.

5.6 Spin structure of $\tau^- \rightarrow \pi^- \pi^- \pi^+ \nu_\tau$: hadron form-factor

The hadron current J_{had}^μ in the $\tau^- \rightarrow \pi^- \pi^- \pi^+ \nu_\tau$ decay can be constructed of only the five following Lorentz tensors: p_1^μ , p_2^μ , p_3^μ , $g^{\mu\nu}$, and $\varepsilon^{\mu\nu\rho\sigma}$. To reveal the spin structure of X^- resonances, J_{had}^μ is decomposed into the linear combination of four Lorentz vectors:

$$J_{\text{had}}^\mu = p_{1,\perp}^\mu F_1(q^2, s_1, s_2) + p_{2,\perp}^\mu F_2(q^2, s_1, s_2) \quad (5.38)$$

$$+ q^\mu F_\pi(q^2, s_1, s_2) \quad (5.39)$$

$$+ \varepsilon^{\mu\nu\rho\sigma} p_{1,\nu} p_{2,\rho} p_{3,\sigma} F_\varepsilon(q^2, s_1, s_2). \quad (5.40)$$

a_\perp^μ is the a^μ component, orthogonal to q^μ ,

$$a_\perp^\mu \equiv a^\mu - \frac{q^\mu q^\nu a_\nu}{q^2} \quad (5.41)$$

for an arbitrary four-vector a^μ . $q^\mu \equiv p_1^\mu + p_2^\mu + p_3^\mu$ is used to shorten the expression.

The Lorentz vectors corresponding to the definite J^P quantum numbers are

5 Partial-wave analysis

- $p_{1,\perp}^\mu F_1(q^2, s_1, s_2) + p_{2,\perp}^\mu F_2(q^2, s_1, s_2)$, the axial current ($J^P = 1^+$),
- $q^\mu F_\pi$, the pseudoscalar current ($J^P = 0^-$), and
- $\varepsilon^{\mu\nu\rho\sigma} p_{1,\nu} p_{2,\rho} p_{3,\sigma} F_\varepsilon$, the vector current ($J^P = 1^-$).

The form-factors $F(q^2, s_1, s_2)$ are the complex-valued functions of only the mass variables q^2 , s_1 , and s_2 , while all the angular dependence is contained in the Lorentz vectors. Bose symmetry imposes

$$F_1(q^2, s_1, s_2) = F_2(q^2, s_2, s_1). \quad (5.42)$$

Axial, pseudoscalar, and vector currents are orthogonal to each other, thus they form the orthogonal basis. While projecting partial waves onto these currents, J^P is encoded in the basis Lorentz vectors, and S and L are encoded in the form-factors.

G -parity conservation leads to $F_\varepsilon = 0$. Also, the $q^\mu F_\pi$ contribution is expected to be small according to the hypothesis of the partially conserved axial current proposed in [64].

5.7 Evaluation of partial waves: covariant tensor formalism

There are two approaches to describe the spin structure of a hadron system: helicity [65] and tensor [66, 67]. I use the latter one because the Lorentz-covariant tensors are compatible with the hadron current description in [9, 62]. The detailed description of this approach is given in [68].

In the cascade of $X^- \rightarrow \pi^- \xi^0$ and $\xi^0 \rightarrow \pi^- \pi^+$ decays, there are three non-trivial spin structures: J , L , and S , which are represented by Lorentz tensors t . In the rest frame of a decaying particle A, t must be in the irreducible representation of the rotation group. This implies that t are symmetric, traceless, and transverse to the four-momentum p_A^μ of the decaying particle. In the cascade, A stands for either X^- or ξ^0 .

In both decays of the cascade, the four-momentum conservation law states that

$$q^\mu = p_{\xi^0}^\mu + p_1^\mu \text{ and} \quad (5.43)$$

$$p_{\xi^0}^\mu = p_2^\mu + p_3^\mu, \quad (5.44)$$

where $p_{\xi^0}^\mu$ denotes the isobar four-momentum. $p_A^\mu = q^\mu$ if t represents L and $p_A^\mu = p_{\xi^0}^\mu$ if t represents S .

5.7 Evaluation of partial waves: covariant tensor formalism

To make t transverse to p_A^μ , one needs to project it out with the projection operator $g_A^{\mu\nu}$,

$$g_A^{\mu\nu} = g^{\mu\nu} - p_A^\mu p_A^\nu / p_A^2. \quad (5.45)$$

t rank matches with either L or S . For rank zero,

$$t_A = 1. \quad (5.46)$$

For rank one,

$$t_A^\mu = \frac{1}{2} g_A^{\mu\nu} (p_{B,\nu} - p_{C,\nu}), \quad (5.47)$$

where B and C denote the decay product of the particle A. For rank two, $t_A^{\mu\nu}$ is expressed via t_A^μ ,

$$t_A^{\mu\nu} = \frac{1}{2} [3 t_A^\mu t_A^\nu - g_A^{\mu\nu} t_{A,\sigma}^\sigma], \quad (5.48)$$

thus it also depends on the difference of the four-momenta of the particle A decay products. For rank three,

$$t_A^{\mu\nu\rho} = \frac{1}{2} [5 t_A^\mu t_A^\nu t_A^\rho - t_{A,\sigma}^\sigma (g_A^{\mu\nu} t_A^\rho + g_A^{\nu\rho} t_A^\mu + g_A^{\rho\mu} t_A^\nu)]. \quad (5.49)$$

In this analysis, partial waves with S or L above three are not considered.

In Eq. (5.47) the order of B and C four-momenta can be arbitrary. I chose

$$t_{X^-}^\mu = \frac{1}{2} g_{X^-}^{\mu\nu} (p_{\xi^0,\nu} - p_{1,\nu}) \quad \text{and} \quad (5.50)$$

$$t_{\xi^0}^\mu = \frac{1}{2} g_{\xi^0}^{\mu\nu} (p_{2,\nu} - p_{3,\nu}). \quad (5.51)$$

Partial waves are composed by contracting tensors that correspond to L and S . For example, $1^+ [f_2(1270)\pi]_P$ wave corresponds to the tensor $t_{w,1}^\mu$,

$$t_{w,1}^\mu = t_{X^-}^\nu t_{\xi^0,\nu}^\mu, \quad (5.52)$$

where a subscript 1 denotes that the isobar is composed of $\pi^- {}_2\pi^+$. Pseudoscalar partial waves are multiplied by q^μ after contraction, for example, $0^- [f_2(1270)\pi]_D$ wave corresponds to

$$t_{w,1}^\mu = q^\mu t_{X^-}^{\nu\rho} t_{\xi^0,\nu\rho}^\mu. \quad (5.53)$$

Vector partial waves are contracted with $\varepsilon_{\mu\nu\rho\sigma} q^\nu$, for example, the $1^- [f_2(1270)\pi]_D$ wave corresponds to

$$t_{w,1}^\mu = \varepsilon^{\mu\nu\rho\sigma} q_\nu t_{X^-,\rho}^\mu t_{\xi^0,\sigma}^\mu. \quad (5.54)$$

Partial waves are constructed by imposing the Bose symmetry as follows:

$$j_w^\mu = \Delta_{\xi^0}(s_1) t_{w,1}^\mu + \Delta_{\xi^0}(s_2) t_{w,2}^\mu, \quad (5.55)$$

where $\Delta_{\xi^0}(s_1)$ is the dynamic factor of the isobar ξ^0 . A subscript 2 denotes that the isobar is composed of $\pi^- {}_2\pi^+$.

5.8 Dynamic factor parametrization of isobars

Usually $\Delta_{\xi^0}(s_1)$ is described by the relativistic Breit-Wigner function [69]:

$$\Delta_{\xi^0}(s_1) = \frac{m_{\xi^0}^2 F_S(s_1) F_L(q^2, s_1)}{m_{\xi^0}^2 - s_1 - i\sqrt{s_1} \Gamma_{\xi^0}(s_1) F_S(s_1)}, \quad (5.56)$$

$$\Gamma_{\xi^0}(s_1) = \Gamma_{\xi^0} \left(\frac{q_s}{q_m} \right)^{2S+1} \frac{m_{\xi^0}}{\sqrt{s_1}}, \quad (5.57)$$

where m_{ξ^0} and Γ_{ξ^0} are masses and widths of ξ^0 , and F_S and F_L are the Blatt-Weisskopf centrifugal-barrier factors.

The values of masses and widths are taken from [69] and are shown in Table 7.

Isobar	$I^G S^{PC}$	mass [GeV]	width [GeV]
$f_0(980)$	$0^+ 0^{++}$	0.99	0.07
$f_0(1500)$	$0^+ 0^{++}$	1.504	0.109
$\rho(770)$	$1^+ 1^{--}$	0.7690	0.1509
$\rho(1450)$	$1^+ 1^{--}$	1.465	0.4
$f_2(1270)$	$0^+ 2^{++}$	1.2755	0.1867
$\omega(782)$	$0^- 1^{--}$	0.782 65	0.008 49

Table 7: Masses and widths for the isobars, described with the Breit-Wigner function.

To take into account finite sizes of mesons, $\Delta_{\xi^0}(s_1)$ is corrected with two Blatt-Weisskopf centrifugal-barrier factors F_S and F_L [70]. F_S takes into account the finite size of ξ^0 . It depends on S and the break-up momentum in the rest frame of ξ^0 . F_L takes into account the finite size of X^- . It depends on L and the break-up momentum in the rest frame of X^- , which is a function of q^2 and the invariant mass of two pions. There are two alternative parametrizations for F , and I use the relativistic one, for example for the angular momentum 1,

$$F_1(x) = \sqrt{\frac{1+x_0}{1+x}}, \quad (5.58)$$

where $x = (p_b d)^2$, p_b is the break-up momentum, $x_0 = (p_0 d)^2$, p_0 is the value of p_b when the invariant mass of the decay products is set to the nominal mass of the isobar, and

$$1/d = 0.1937 \text{ [GeV]}. \quad (5.59)$$

For some isobars, the Breit-Wigner shape is not applicable (for example, $f_0(500)$ or so-called σ , see [71, 72]), and a more complex parametrization is needed.

5.9 Fitting method of partial-wave decomposition

In the conventional PWA, parameters describing isobars' shapes such as mass and width are fixed in the fit. This leads to model dependence and introduces a bias. Another disadvantage of the conventional PWA arises when $m_{3\pi}$ is below m_{ξ^0} of two or more isobars. At some point, there is not enough precision of the fitter to distinguish these isobars, which leads to nonphysical results. These partial waves need to be excluded from the fit below corresponding $m_{3\pi}$ thresholds. There is no analytical prediction to find these thresholds. I vary them to achieve a maximum smoothness of the intensity. There are methods to select partial waves numerically (for example, see [73]), which is useful for large wave sets, but these methods can also introduce a bias.

To overcome these limitations of conventional PWA, one can parametrize some isobars by complex-valued step functions in the freed-isobar PWA [60],

$$\Delta(m) = \sum_i \mathcal{C}_i \Theta_i(m) \quad (5.60)$$

$$\Theta_w(m) = \begin{cases} 1 & \text{if } m \text{ in the } m_{2\pi} \text{ bin } i \\ 0 & \text{otherwise.} \end{cases} \quad (5.61)$$

This method removes model dependence from the isobar parametrization. However, it has some disadvantages in comparison with conventional PWA: first, there are possible mathematical ambiguities [60] when more than one isobar is freed, and second, the number of fit parameters increases significantly per freed isobar. Nevertheless, this method is suitable to study the dynamics of some complex isobars, where the conventional method is too simplistic.

5.9 Fitting method of partial-wave decomposition

Partial-wave decomposition is done in bins of $m_{3\pi}$, the bins being narrow enough to assume there is no change in the $m_{3\pi}$ dynamics, but larger than the detector resolution.

The number of fit parameters N_{par} in the conventional PWA is significantly lower than in the freed-isobar PWA. The only free parameters of a single partial wave w are the complex-valued partial-wave amplitudes \mathcal{C}_w , thus one has two real-valued parameters per wave. Also, the global phase has no physical sense, thus one wave is parametrized with only the real part of \mathcal{C}_w .

$$N_{\text{par}} = 2 \times N_{\text{PW}} - 1, \quad (5.62)$$

where N_{PW} is the number of partial waves. For one wave, the imaginary part is set to zero. This wave is called the anchor wave.

5 Partial-wave analysis

In a freed-isobar PWA, the number of parameters for a single wave is $2 \times N_{\text{bins of } m_{3\pi}}$, and the anchor wave must be a fixed-isobar partial wave.

To simplify the logarithm likelihood, I also neglect how phase space and acceptance depend on $m_{3\pi}$ in a single $m_{3\pi}$ bin (this dependence is recovered in the resonance-model fit). Thus, the probability density function (PDF) is proportional to $|\mathcal{M}|^2$.

Let us introduce the intensity, equalling the PDF with an arbitrary normalizing constant. Intensity is the bilinear form of \mathcal{C}_w :

$$\mathcal{I}(\Phi|\mathcal{C}_w) = \sum_{w,v} \mathcal{C}_w \mathcal{C}_v^* \mathcal{I}_{wv}(\Phi), \quad \mathcal{I}_{wv}(\Phi) = \overline{\mathfrak{T}}^{\mu\nu} j_\mu^w (j_\nu^v)^*, \quad (5.63)$$

\mathcal{I}_{wv} is a hermitian matrix of rank 4, the same rank as of $\overline{\mathfrak{T}}^{\mu\nu}$.

The \mathcal{C}_w are found in the fitting procedure by numerically maximizing $\ln \mathcal{L}(\mathcal{C}_w)$ in every bin of $m_{3\pi}$ with Minuit2 [74]. The extended logarithm likelihood is

$$\ln \mathcal{L}(\mathcal{C}_w) = \sum_{\text{Data}} \ln \mathcal{I}(\Phi|\mathcal{C}_w) - \mathcal{N}(\mathcal{C}_w), \quad (5.64)$$

where $\mathcal{N}(\mathcal{C}_w)$ is the normalizing constant,

$$\mathcal{N}(\mathcal{C}_w) = \int \varepsilon(\Phi) \mathcal{I}(\Phi|\mathcal{C}_w) d\Phi, \quad (5.65)$$

and $\varepsilon(\Phi)$ is the detector acceptance. There is no good method to describe $\varepsilon(\Phi)$ in the six-dimensional phase space analytically, but one can sample $\mathcal{N}(\mathcal{C}_w)$ with the simulated data by averaging over those events which passed the selection criteria. This procedure requires the simulated sample being larger than the real data sample to reduce the uncertainties. If a model was used to generate the simulated sample, each simulated event enters averaging with a weight, which is inversely proportional to the model's intensity.

The normalizing constant can be expressed via the bilinear form of \mathcal{C}_w :

$$\mathcal{N}(\mathcal{C}_w) = \mathcal{N}_{wv} \mathcal{C}_w \mathcal{C}_v^*, \quad (5.66)$$

and the integral matrix \mathcal{N}_{wv} can be pre-calculated before the fit:

$$\mathcal{N}_{wv} = \frac{\sum_{\text{Acc MC}} \mathcal{I}_{wv}(\Phi) / |\mathcal{M}_{\text{MC Generator}}(\Phi)|^2}{\sum_{\text{Acc MC}} 1 / |\mathcal{M}_{\text{MC Generator}}(\Phi)|^2}. \quad (5.67)$$

Because the simulated sample of Belle was produced with TAUOLA, \mathcal{N}_{wv} is de-weighted with the matrix element of $\tau^- \rightarrow \pi^- \pi^- \pi^+ \nu_\tau$ from TAUOLA, and \mathcal{N}_{wv} does not depend on the TAUOLA model. However, the uncertainty of \mathcal{N}_{wv} depends on the number of generated events per $m_{3\pi}$ bin, thus it depends on the TAUOLA model.

5.10 Mathematical ambiguities of freed-isobar PWA

There are mathematical ambiguities [60], which appear in the PWA if two or more waves are parametrized with freed shape isobars. They are called zero modes, the dynamic amplitudes constructed such that the corresponding hadron current vanishes:

$$\sum_w j_w^\mu \Delta_w(m_{2\pi}) = 0. \quad (5.68)$$

Let us have a look at a zero mode example for the $1^+[1^{--}\pi]_S$ and $1^+[0^{++}\pi]_P$ waves, which we can find analytically. The hadron current $j_{0^{++}}^\mu$ of the $1^+[0^{++}\pi]_P$ wave is

$$j_{0^{++}}^\mu = \Delta_{0^{++}}(s_1) (p_2 + p_3 - p_1)_\perp^\mu + \Delta_{0^{++}}(s_2) (p_1 + p_3 - p_2)_\perp^\mu, \quad (5.69)$$

and the hadron current $j_{1^{--}}^\mu$ for the $1^+[1^{--}\pi]_S$ wave is

$$j_{1^{--}}^\mu = \Delta_{1^{--}}(s_1) (p_2 - p_3)_\perp^\mu + \Delta_{1^{--}}(s_2) (p_1 - p_3)_\perp^\mu. \quad (5.70)$$

The resulting zero mode is

$$\Delta_{0^{++}}(s_2) = -2/3 \Delta_{1^{--}}(s_2). \quad (5.71)$$

The obtained zero mode of the $1^+[1^{--}\pi]_S$ and $1^+[0^{++}\pi]_P$ waves is a real-valued constant. It is notable that the same result was obtained in [75] for the diffractive production of three pions. Indeed, the zero mode is defined in a such way that the hadron current of the decay amplitude equals zero, and despite the hadron current being contracted with a different production amplitude, the total amplitude vanishes.

One can cross-check the zero mode from Eq. (5.71) numerically by looking at the spectrum and the eigenvectors of the Gram matrix:

$$\mathbb{N} = \int d\Phi \mathcal{I}_{wv}, \quad (5.72)$$

where \mathcal{I}_{wv} is the bilinear form matrix from Eq. (5.63) integrated over the phase space, and w and v are the freed wave $m(2\pi)$ bin indices. Numerically, the integral is approximated by the \mathcal{I}_{wv} averaged over the phase space using an MC sampling technique. Fig. 16a shows the Gram matrix spectrum: the lowest eigenvalue corresponds to the zero mode. Real and imaginary components of the zero mode shown in Fig. 16b and Fig. 16c are indeed constants. Moreover, the imaginary part is compatible with zero with double floating point precision level. The shown result matches with the analytical prediction in Eq. (5.71).

5 Partial-wave analysis

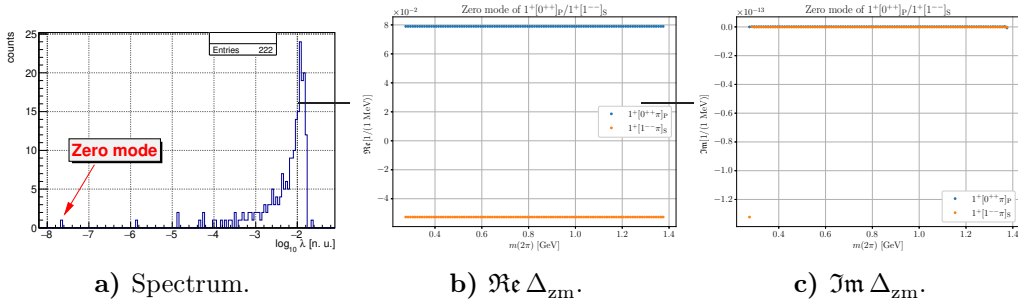


Figure 16: Numerical search for the Δ_{zm} — zero mode.

5.11 Isobar fit

Even if only a single partial wave is freed and there are no zero modes in the partial-wave decomposition fit, one still needs an isobar fit to the resulting coefficients to extract not only the isobar's parameters, but also its complex magnitude. This complex magnitude plays the same role as the \mathcal{C}_w complex coefficients in the conventional PWA.

If in the fit there is at least one zero mode, it needs to be resolved in the simultaneous isobar fit by fixing a reference wave (usually it is the dominant $1^+[1^-\pi]_S$) to a well-known shape. For $1^+[1^-\pi]_S$, it is the $\rho(770)$ shape. The naive χ^2 fit approach will not work in this case because the covariance matrix also contains the same zero mode, although it is distorted due to unequal binning for different waves. In order to fix this issue, one needs to modify the covariance matrix \mathbb{V} : first, everything but the fitted freed wave must be truncated, second, zero modes must be projected out with the following operator,

$$\mathbb{P}_{ij} = \delta_{ij} - \Delta_i \Delta_j, \quad (5.73)$$

where δ_{ij} denotes the Cronecker symbol, and Δ_i is the zero mode. Because zero modes are real functions, \mathbb{V} indices corresponding to the real and imaginary parts of the freed partial wave coefficients are decoupled,

$$(\mathbb{V}_{\Re, \Im})_{ij} \rightarrow (\mathbb{P} \mathbb{V}_{\Re, \Im} \mathbb{P})_{ij}, \quad (5.74)$$

and the χ^2 of the fit is

$$[\vec{\mathbf{x}}_{\text{PWA}}(m_{2\pi}) - \vec{\mathbf{x}}_{\text{model}}(m_{2\pi})]^\top \mathbb{V}^{-1} [\vec{\mathbf{x}}_{\text{PWA}}(m_{2\pi}) - \vec{\mathbf{x}}_{\text{model}}(m_{2\pi})], \quad (5.75)$$

where $\vec{\mathbf{x}}_{\text{PWA}}$ denotes the real-valued vector composed of real and imaginary parts of the complex amplitudes \mathcal{C}_w obtained in the partial-wave decomposition, and $\vec{\mathbf{x}}_{\text{model}}$ denotes the real and imaginary parts of the complex amplitudes \mathcal{C}_w predicted in the isobar fit as a function of $m_{2\pi}$.

5.12 Resonance-model fit

After extracting partial-wave amplitudes \mathcal{C}_w , I analyze the three-body dynamics of the disentangled quantum states. The goal of this stage is to find a decay amplitude as a function of $m_{3\pi}$. It is a χ^2 fit,

$$\chi^2 = [\vec{\mathbf{x}}_{\text{PWA}}(m_{3\pi}) - \vec{\mathbf{x}}_{\text{model}}(m_{3\pi})]^T \mathbb{V}^{-1} [\vec{\mathbf{x}}_{\text{PWA}}(m_{3\pi}) - \vec{\mathbf{x}}_{\text{model}}(m_{3\pi})], \quad (5.76)$$

where the notation is as in Eq. (5.75).

The integrals in Eq. (5.67) are normalized to the number of reconstructed events in each bin, thus it is necessary to divide out the efficiency in the $m_{3\pi}$ dimension in the resonance-model fit, such that

$$\vec{\mathbf{x}}_{\text{PWA}} \rightarrow \vec{\mathbf{x}}_{\text{PWA}} \sqrt{\frac{N_{\text{gen}}(m_{3\pi})}{N_{\text{rec}}(m_{3\pi})}}, \quad (5.77)$$

where $N_{\text{gen}}(m_{3\pi})$ is the number of generated events in a bin of $m_{3\pi}$, and $N_{\text{rec}}(m_{3\pi})$ is the number of reconstructed events in the same bin.

Similar adjustment is needed to take into account the phase space volume behavior as a function of $m_{3\pi}$. I multiply the predicted intensities by the phase space volume, such that

$$\vec{\mathbf{x}}_{\text{model}} \rightarrow \vec{\mathbf{x}}_{\text{model}} \sqrt{\Phi(m_{3\pi})}. \quad (5.78)$$

In the resonance-model fit, the predicted complex amplitudes are rotated such that the imaginary part of the anchor wave is zero.

The resonance-model fit is performed only to a manually selected set of partial waves: to those which are significant, and to which I could find a good model. Those waves to which I did not manage to find a model will be published in a machine-readable format for further investigation and for MC generator usage.

The resonance-model fit is repeated several times with uniformly distributed starting parameters; the parameters leading to the least χ^2 value is the result of the fit.

5.13 Dynamic amplitude of the $1^+[\rho(770)\pi]_S$ wave

According to previous studies one can expect the appearance of $a_1(1260)$ and $a_1(1640)$ resonances in the $1^+[\rho(770)\pi]_S$ channel. Also, it was shown by CLEO II, that a single Breit-Wigner function does not describe the $1^+[\rho(770)\pi]_S$ shape well, thus a more complex model is needed. The CLEO II model is taken from [9], with the difference that the K^*K branching fraction of $a_1(1260)$ is set to zero. It

5 Partial-wave analysis

includes only $a_1(1260)$ resonance parametrized with the Breit-Wigner-like shape, but with a sophisticated energy-dependent width,

$$\Gamma(s) = \begin{cases} 0 & s < 0.1753 \text{ [GeV}^2\text{]} \\ P_2(s) & s \in [0.1753, 0.8230] \text{ [GeV}^2\text{]} \\ P_4(s) & s > 0.8230 \text{ [GeV}^2\text{]}, \end{cases} \quad (5.79)$$

where P_n denotes a polynomial of n -th degree. Polynomial coefficients and ranges are taken from the TAUOLA source code. Fig. 17 compares COMPASS $a_1(1260)$

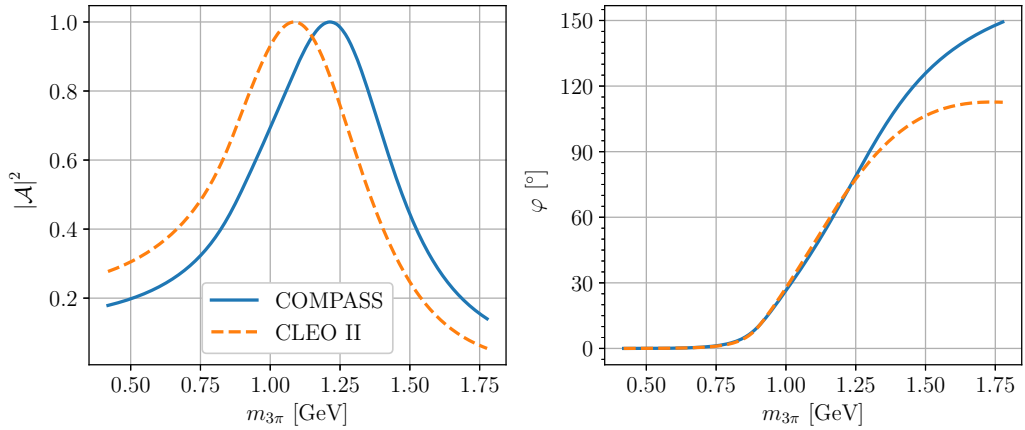


Figure 17: Normalized amplitude of the $a_1(1260)$ meson for COMPASS and CLEO II parametrizations. The left figure shows the amplitude modulo squared, the right figure shows the complex phase of the amplitudes. Models are normalized such that magnitude maxima are unity. Blue solid line shows the COMPASS model. Orange hashed line shows the CLEO II model.

meson amplitude from [8] with the CLEO II one. Both models are parametrized with mass m and width Γ . For the COMPASS model $m = 1.299$ GeV, $\Gamma = 0.420$ GeV, and for the CLEO II model $m = 1.331$ GeV, $\Gamma = 0.814$ GeV. One can see that the larger width of the CLEO II model shifts the peak position below the COMPASS model, while the full widths on the half of the heights are approximately equal. The models have the same phase motion below 1.23 GeV and above 1.25 GeV CLEO II phase is notably lower.

6 Simulation studies

PWA is a complicated analysis technique and requires testing before it can be applied to the data. Also, there are several considerations to why PWA may not work for the $\tau^- \rightarrow \pi^- \pi^- \pi^+ \nu_\tau$ process. One of them is the presence of the tau neutrino, which misses the detector. Thus, we do not have the full information about the hadron system and the partial-wave decomposition fit cannot disentangle partial waves. Second, ISR or $e^+e^- \rightarrow \tau^+\tau^-$ spin-spin correlations may distort hadron shapes. Third, the freed-isobar PWA fit needs to be validated separately.

All simulation studies are based on a single test scheme: arbitrary input $\mathcal{C}_{w, \text{input}}$ are fed into an MC generator. The partial-wave decomposition fit finds output $\mathcal{C}_{w, \text{output}}$ and a covariance matrix for $\mathcal{C}_{w, \text{output}}$. The difference Δ_i is normalized in units of the $\mathcal{C}_{w, \text{output}}$ uncertainties σ_i , highlighting possible biases. i enumerates the real-valued parameters of the fit such that $i = 2w$ for the real part of $\mathcal{C}_{w, \text{output}}$ and $i = 2w + 1$ for the imaginary part of $\mathcal{C}_{w, \text{output}}$. If on average no bias is found, the cross-check is passed.

6.1 Missing-neutrino test

To reduce the chance of a mistake in the partial-wave decomposition program, I check it against an independent implementation of the partial-wave decomposition algorithm in [76], TauPWA, which can be used also as an MC generator. TauPWA generates a simulated test sample of 360×10^3 events without acceptance effects and without background. Only six partial waves are implemented in TauPWA.

The reference values $\mathcal{C}_{w, \text{input}}$ and the partial-wave decomposition fit output $\mathcal{C}_{w, \text{output}}$ are shown in Table 8. Most of the Δ_i lie within one standard deviation of the reference values, except $\Im 1^+[f_0(980)\pi]_P$, $\Re 1^+[\rho(1450)\pi]_S$, and $\Im 1^+[f_2(1270)\pi]_P$, where the discrepancy is slightly above the statistical uncertainty. It can be concluded that there are no obvious mistakes in the main partial-wave decomposition program, and it works satisfactorily. This test also demonstrates that there is no bias caused by averaging the intensity \mathcal{I} over the angle α in the partial-wave decomposition.

6 Simulation studies

Wave component	Input	Output	Δ_i/σ_i
$\Re 1^+[f_0(980)\pi]_P$	0.0500	0.0501 ± 0.0019	0.05
$\Im 1^+[f_0(980)\pi]_P$	-0.0866	-0.0839 ± 0.0023	1.17
$\Re 1^+[\rho(770)\pi]_S$	0.7000	0.7000 ± 0.0027	Ref. wave
$\Im 1^+[\rho(770)\pi]_S$		Set to zero in fit	
$\Re 1^+[\rho(1450)\pi]_S$	0.0500	0.0465 ± 0.002	1.75
$\Im 1^+[\rho(1450)\pi]_S$	0.0866	0.0830 ± 0.004	0.90
$\Re 1^+[\rho(770)\pi]_D$	-0.1000	-0.0977 ± 0.0028	0.82
$\Im 1^+[\rho(770)\pi]_D$	0.1732	0.1737 ± 0.0038	0.13
$\Re 1^+[\rho(1450)\pi]_D$	-0.0500	-0.0505 ± 0.003	0.17
$\Im 1^+[\rho(1450)\pi]_D$	0.0000	-0.0032 ± 0.0036	0.89
$\Re 1^+[f_2(1270)\pi]_P$	0.0966	0.0980 ± 0.0022	0.64
$\Im 1^+[f_2(1270)\pi]_P$	0.0259	0.0281 ± 0.0019	1.16

Table 8: Input $\mathcal{C}_{w \text{ input}}$, output $\mathcal{C}_{w \text{ output}}$, and the difference Δ_i of the first test against the TauPWA program, $m(3\pi) \in [1.50, 1.52]$ GeV.

6.2 Initial-state radiation test

The TauPWA program does not take into account ISR effects. To study if ISR introduces a bias in the partial-wave decomposition, I developed an updated version of TAUOLA, the TAUOLA-m generator [77]. It can generate $\tau^- \rightarrow \pi^- \pi^- \pi^+ \nu_\tau$ events in a single $m_{3\pi}$ bin using partial waves. TAUOLA-m, like the original TAUOLA, is integrated with the $e^+e^- \rightarrow \tau^+\tau^-$ MC generator KKMC [44], which takes into account ISR effects. To speed up the test, no detector effects are simulated, and to simulate the ISR effect, a selection on $\cos\psi$ is required such that

$$|\cos\psi| \leq 1. \quad (6.1)$$

The wave set in the test is extended with the $1^+[\sigma\pi]_P$ wave in comparison with the previous test.

$\mathcal{C}_{w \text{ input}}$ and the $\mathcal{C}_{w \text{ output}}$ are shown in Table 9. Most of the Δ_i lie within one standard deviation of the reference values, except $\Re 1^+[\sigma\pi]_P$, $\Im 1^+[f_0(980)\pi]_P$, and $\Re 1^+[\rho(770)\pi]_D$, where the discrepancy is above the statistical uncertainty. It can be concluded that the ISR does not introduce a notable bias in the partial-wave decomposition.

Passing both tests validates the TAUOLA-m MC generator as well.

Wave component	Input	Output	Δ_i/σ_i
$\Re 1^+[\sigma\pi]_P$	-0.0500	-0.0571 ± 0.0053	1.34
$\Im 1^+[\sigma\pi]_P$	0.0866	0.0825 ± 0.0066	0.62
$\Re 1^+[f_0(980)\pi]_P$	0.0500	0.0506 ± 0.0023	0.26
$\Im 1^+[f_0(980)\pi]_P$	-0.0866	-0.0814 ± 0.0027	1.93
$\Re 1^+[\rho(770)\pi]_S$	0.7000	0.7000 ± 0.0034	Ref. wave
$\Im 1^+[\rho(770)\pi]_S$		Set to zero in fit	
$\Re 1^+[\rho(1450)\pi]_S$	0.0500	0.0510 ± 0.0048	0.21
$\Im 1^+[\rho(1450)\pi]_S$	0.0866	0.0874 ± 0.0068	0.12
$\Re 1^+[\rho(770)\pi]_D$	-0.1000	-0.0947 ± 0.0032	1.66
$\Im 1^+[\rho(770)\pi]_D$	0.1732	0.1714 ± 0.0045	0.40
$\Re 1^+[\rho(1450)\pi]_D$	-0.0500	-0.0530 ± 0.0043	0.70
$\Im 1^+[\rho(1450)\pi]_D$	0.0000	-0.0039 ± 0.005	0.78
$\Re 1^+[f_2(1270)\pi]_P$	0.0966	0.0953 ± 0.0032	0.41
$\Im 1^+[f_2(1270)\pi]_P$	0.0259	0.0247 ± 0.0033	0.36

Table 9: Input and output \mathcal{C}_w of the MC Truth test with TAUOLA-m and ISR effects, $m(3\pi) \in [1.50, 1.52]$ GeV.

6.3 Spin-spin correlation test

The analyzed tauon is produced in the $e^+e^- \rightarrow \tau^+\tau^-$ process such that it is entangled with the tagging tauon. In partial-wave decomposition this entanglement is neglected. To validate the assumption, a test on simulated data is needed.

In the previous test the tag side tauon was generated by KKMC, and it was shown that there is no bias in the assumption that the tag side acceptance effects can be neglected. In this test this assumption is checked. Additionally, it is checked whether the acceptance effect can bias the $J^P = 0^-$ and $J^P = 1^-$ sectors, thus the parameters of these partial waves are included in the fit. The expected \mathcal{C}_w output should be close to zero for these waves, because I did not implement these waves in the TAUOLA-m generator.

The test is constructed as follows. First, TAUOLA-m with the standard Belle KKMC generates signal decay, with inclusive tagging generated with the standard Belle TAUOLA. Second, simple selection criteria are applied at the generator level to the tag side final state charged particle: it is required to have $p_\perp > 0.1$ GeV and $\theta_{\text{lab}} \in [17, 150]^\circ$. Also, $\cos\psi$ needs to have a physical value in the $[-1, 1]$ range.

Table 10 shows the result of this test. No bias in neglecting spin-spin correlations is found.

wave	Input	Output	Δ_i/σ_i
\Re $1^+[\text{f}_0(980)\pi]_{\text{P}}$	4.22	4.03 ± 0.25	0.78
\Im $1^+[\text{f}_0(980)\pi]_{\text{P}}$	1.39	1.28 ± 0.26	0.39
\Re $1^+[\text{f}_0(1500)\pi]_{\text{P}}$	-15.89	-16.85 ± 4.27	0.22
\Im $1^+[\text{f}_0(1500)\pi]_{\text{P}}$	22.63	24.74 ± 5.56	0.38
\Re $1^+[\rho(770)\pi]_{\text{S}}$	-83.34	-83.34 ± 0.74	Reference wave
\Im $1^+[\rho(770)\pi]_{\text{S}}$		Set to zero in fit	
\Re $1^+[\rho(1450)\pi]_{\text{S}}$	-0.30	-0.77 ± 1.72	0.27
\Im $1^+[\rho(1450)\pi]_{\text{S}}$	-24.06	-22.31 ± 2.13	0.82
\Re $1^+[\rho(770)\pi]_{\text{D}}$	82.83	82.18 ± 2.73	0.24
\Im $1^+[\rho(770)\pi]_{\text{D}}$	26.93	30.61 ± 6.39	0.58
\Re $1^+[\rho(1450)\pi]_{\text{D}}$	-15.94	-17.54 ± 11.13	0.14
\Im $1^+[\rho(1450)\pi]_{\text{D}}$	-11.69	4.42 ± 13.01	1.24
\Re $1^+[\text{f}_2(1270)\pi]_{\text{P}}$	-13.39	-10.65 ± 3.97	0.69
\Im $1^+[\text{f}_2(1270)\pi]_{\text{P}}$	131.20	125.35 ± 4.31	1.36
\Re $1^+[\sigma_{\text{AMP}}\pi]_{\text{P}}$	80.87	73.76 ± 7.03	1.01
\Im $1^+[\sigma_{\text{AMP}}\pi]_{\text{P}}$	-113.97	-120.57 ± 6.76	0.98
\Re $0^-[\sigma_{\text{AMP}}\pi]_{\text{S}}$	0.00	0.11 ± 0.85	0.14
\Im $0^-[\sigma_{\text{AMP}}\pi]_{\text{S}}$	0.00	-0.16 ± 0.52	0.31
\Re $0^-[\text{f}_0(980)\pi]_{\text{S}}$	0.00	0.04 ± 0.08	0.55
\Im $0^-[\text{f}_0(980)\pi]_{\text{S}}$	0.00	0.07 ± 0.08	0.80
\Re $0^-[\rho(770)\pi]_{\text{P}}$	0.00	0.01 ± 1.62	0.01
\Im $0^-[\rho(770)\pi]_{\text{P}}$	0.00	-0.30 ± 2.44	0.12
\Re $1^-[\rho(770)\pi]_{\text{P}}$	0.00	1.60 ± 2.38	0.67
\Im $1^-[\rho(770)\pi]_{\text{P}}$	0.00	0.57 ± 1.96	0.29

Table 10: Test of the tauon pair spin-spin correlation effect.

6.4 Freed-isobar test

To cross-check the freed-isobar PWA, I analyze data simulated with only four partial waves: $1^+[\text{f}_0(975)\pi]_{\text{P}}$, $1^+[\rho(770)\pi]_{\text{S}}$, $1^+[\rho(770)\pi]_{\text{D}}$, and $1^+[\text{f}_2(1270)\pi]_{\text{P}}$. I parametrize only $1^+[1^{--}\pi]_{\text{S}}$ wave with the freed-isobar method to avoid zero modes and simplify the test. I fit the freed-isobar complex amplitudes and a complex multiplier for each other wave. I then fit a Breit-Wigner function to the freed-isobar results, see Fig. 18. The second fit determines the ρ 's mass and width to be (769.8 ± 0.6) MeV and (155.2 ± 1.3) MeV, agreeing with the simulated values of 769.0 MeV and 150.9 MeV. The fit results (Table 11) all agree with their simulated values.

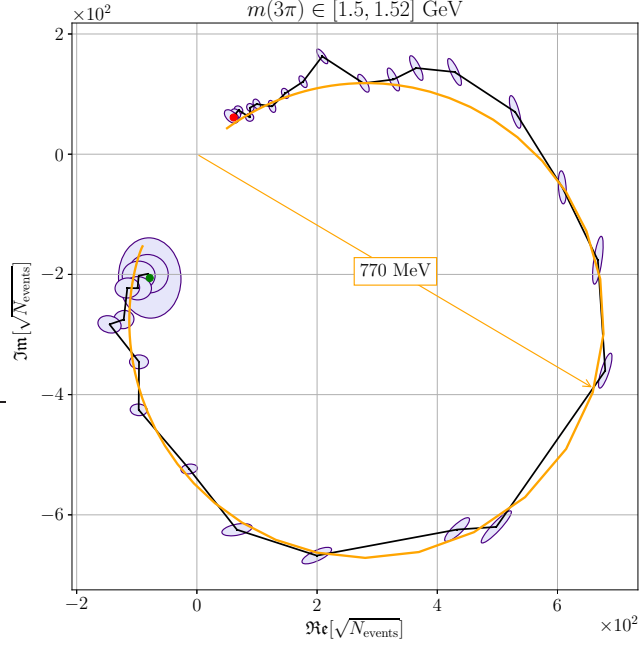


Figure 18: Freed-isobar PWA (violet) and Breit-Wigner (orange) fit results for the $1^+[1^-\pi]_S$ wave in simulated data; ellipses show 68%-confidence intervals. The arrow points towards the resulting pole position $m - \frac{i}{2}\Gamma$.

Wave	Amplitude		Phase [°]	
	sim.	res.	sim.	res.
$[f_0(975)\pi]_P$	0.10	0.099 ± 0.001	-60	-55.485 ± 1.947
$[\rho(770)\pi]_S$	0.70	0.712 ± 0.005	0	reference phase
$[\rho(770)\pi]_D$	0.92	0.959 ± 0.025	120	120.546 ± 0.459
$[f_2(1270)\pi]_P$	0.53	0.514 ± 0.020	15	18.255 ± 2.525

Table 11: Comparison of simulated values and fit results.

The result of this cross-check was published in [78].

7 Results

I present the results of the conventional and freed-isobar PWA, the background leakage studies, and the resonance-model fit to the $1^+[\rho(770)\pi]_S$, $1^+[\text{f}_0(980)\pi]_P$, $1^+[\rho(770)\pi]_D$, $1^+[\sigma\pi]_P$, and $1^+[\text{f}_2(1270)\pi]_P$ waves on the Belle data set.

7.1 Partial-wave decomposition

A partial-wave decomposition was done for all the waves shown in Table 6. No $m_{3\pi}$ efficiency or phase-space correction are applied to the plotted results in this section. The shown intensities \mathcal{I}_w are calculated such that

$$\mathcal{I}_w(\mathcal{C}_w) = |\mathcal{C}_w|^2 \int \mathcal{I}_{ww}(\Phi) d\Phi, \quad (7.1)$$

\mathcal{I}_{ww} is defined in Eq. (5.63) and $\mathcal{C}_{w \text{ output}}$ is the complex amplitude of the w obtained in the fit. The shown phases are evaluated relative to the $1^+[\rho(770)\pi]_S$ wave.

7.1.1 Conventional PWA

Table 12 summarizes the partial-wave decomposition results. The branching fraction \mathbb{B}_w of a partial wave w is defined as follows:

$$\mathbb{B}_w = \frac{\sum_i \mathcal{I}_w}{\sum_i \mathbb{N}_{vv'} \mathcal{C}_v \mathcal{C}_v^*}, \quad (7.2)$$

where \sum_i sums over the bins of $m_{3\pi}$, and $\mathbb{N}_{vv'}$ denotes the Gram matrix from Eq. (5.72). \mathbb{B}_w can be above 1 because of the interference between waves.

I also plot the results of the background leakage study. This study has been performed on the $5 \times L_{\text{int}}$ simulated sample for $e^+e^- \rightarrow \tau^+\tau^-$ and $q\bar{q}$ backgrounds available in Belle MC with the standard partial-wave decomposition procedure. If a partial-wave intensity is above zero, this is considered as a leakage from the background. The plotted intensities of this study are divided by 5 to match the real data luminosity.

Fig. 19 shows the number of events and the normalizing constant of the total PDF \mathcal{N}_{tot} in bins of $m_{3\pi}$.

$$\mathcal{N}_{\text{tot}} = \mathcal{N}_{\text{sig}} + \eta \mathcal{N}_{\text{bcg}}, \quad (7.3)$$

Partial wave	Figure reference	\mathbb{B} [%]
$1^+[\rho(770)\pi]_S$	Fig. 20	108.16
$1^+[\sigma\pi]_P$	Fig. 21	19.22
$1^+[\rho(1450)\pi]_S$	Fig. 22	4.40
$1^+[\mathbf{f}_0(1500)\pi]_P$	Fig. 23	3.81
$1^+[\rho(770)\pi]_D$	Fig. 24	2.26
$1^+[\rho(1450)\pi]_D$	Fig. 25	1.52
$1^+[\mathbf{f}_2(1270)\pi]_P$	Fig. 26	0.90
$1^+[\mathbf{f}_0(980)\pi]_P$	Fig. 27	0.40
$1^+[\mathbf{f}_2(1270)\pi]_F$	Fig. 28	0.11
$0^-[\rho(770)\pi]_P$	Fig. 29	0.20
$0^-[\sigma\pi]_S$	Fig. 30	0.09
$0^-[\mathbf{f}_2(1270)\pi]_D$	Fig. 31	0.02
$0^-[\mathbf{f}_0(980)\pi]_S$	Fig. 32	0.01
$1^-[\omega(782)\pi]_P$	Fig. 34	0.32
$1^-[\mathbf{f}_2(1270)\pi]_D$	Fig. 35	0.23
$1^-[\rho(770)\pi]_P$	Fig. 36	0.06

Table 12: References to the figures with intensities and phases of the partial-wave decomposition and the partial-wave branching fractions.

where \mathcal{N}_{sig} is the normalizing constant from Eq. (5.66), \mathcal{N}_{bck} is the background normalizing from Eq. (4.6), and η is the background-to-signal ratio; it is included in the partial-wave decomposition as a free parameter. Fig. 19a shows the real data, and Fig. 19b shows the simulated background data. The total normalizing constants from the partial-wave decomposition equals the number of events for all $m_{3\pi}$ bins. This happens because of the design of the extended logarithm likelihood function [4]. No observed discrepancy between \mathcal{N}_{tot} and N shows that the partial-wave decomposition works as expected.

Fig. 19a also shows, that the background normalizing constants has discontinuities in some of bins of $m_{3\pi}$. This leads to discontinuities in the signal normalizing constants, while \mathcal{N}_{tot} does not have discontinuities and follows the shape of $N(m_{3\pi})$. The discontinuities appear in the low $m_{3\pi}$ region, where the background contamination is large. They are caused by the significant systematic effect of the neural-network parametrization of the background.

7.1 Partial-wave decomposition

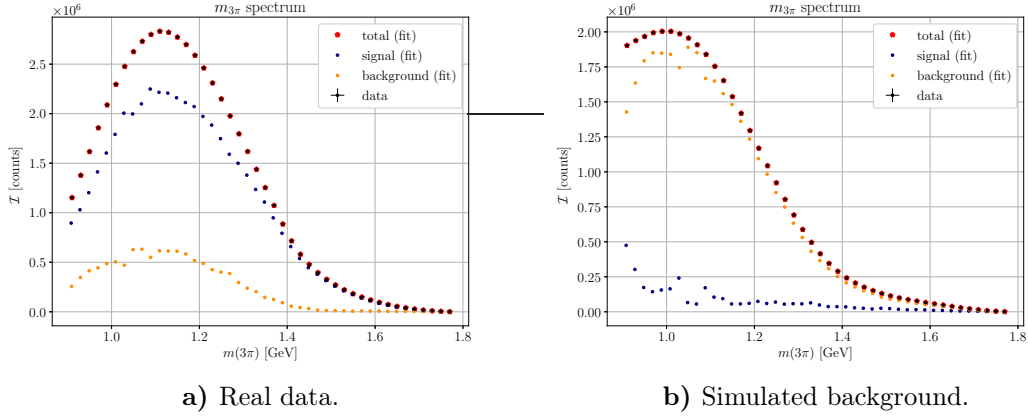


Figure 19: Number of events for signal and background for the real data and the simulated background data. Black dots with error bars show the number of data events, either real or simulated. The partial-wave decomposition parameters are: red hexagons are the total normalizing constants in the number of events, blue squares are the signal normalizing constants, and orange squares are the neural network background normalizing constants.

7.1.1.1 1⁺ sector

Fig. 20 shows the $1^+[\rho(770)\pi]_S$ wave. The intensity only is presented, because the imaginary part is fixed to zero in the fit. The $1^+[\rho(770)\pi]_S$ wave has a clear peak at 1.15 GeV, which corresponds to the $a_1(1260)$ resonance. No other clear peak structure is observed in this wave, but the long tail towards the large $m_{3\pi}$ indicates the presence of the $a_1(1640)$ resonance. This wave dominates in the $\tau^- \rightarrow \pi^- \pi^- \pi^+ \nu_\tau$ process: its branching fraction is above 90%, as shown in Table 12.

Next, the rest of the waves are presented. Their intensities are at least about one order of magnitude smaller than the $1^+[\rho(770)\pi]_S$ wave intensity, thus the background contamination has larger effects on their shapes. The first presented waves are from the $J^P = 1^+$ sector, then from the $J^P = 0^-$ sector, and then from the $J^P = 1^-$ sector. Both intensities and phases are shown.

Fig. 21 shows the $1^+[\sigma\pi]_P$ wave. It has a broad peak at 1.15 GeV corresponding to $a_1(1260)$ and a peaking structure at 1.35 GeV caused by background contamination. The positive phase change in the [1.55, 1.7] GeV range is notable, where the background contamination is relatively small. This might indicate the presence of the $a_1(1640)$ resonance in this partial wave. It is notable that the phase between the $1^+[\sigma\pi]_P$ wave and the $1^+[\rho(770)\pi]_S$ wave is approximately 90°.

Fig. 22 shows the $1^+[\rho(1450)\pi]_S$ wave. The threshold on this wave is set to 1.18 GeV. One might expect that this wave is coupled to the $a_1(1640)$ resonance,

7 Results

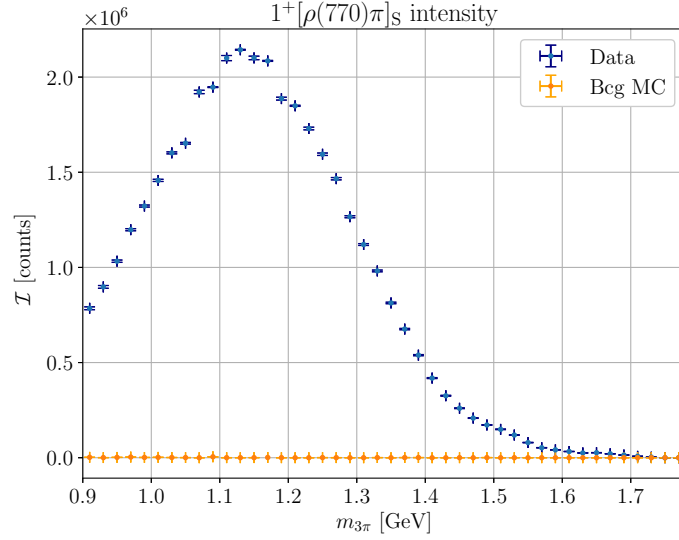


Figure 20: $1^+[\rho(770)\pi]_S$ wave. Blue dots with error bars show the partial-wave decomposition results for the real data, and orange dots with error bars show the partial-wave decomposition result for the simulated background data.

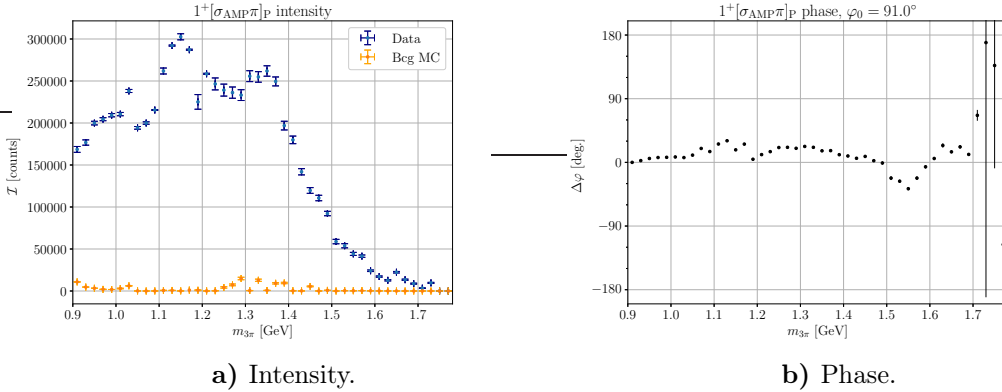


Figure 21: $1^+[\sigma\pi]_P$ wave. In Fig. a the color scheme is the same as in Fig. 20. In Fig. b black dots show the relative phase of the partial-wave decomposition to the real data only.

because of the non-zero intensity and phase increase by about 90° in the region above 1.5 GeV. The intensity discontinuity at 1.25 GeV is caused by the threshold on the $1^+[f_0(1500)\pi]_P$ wave. Below 1.5 GeV, the wave acts effectively as a

7.1 Partial-wave decomposition

complex-valued constant isobar with $1^+[1^{--}\pi]_S$ quantum numbers and compensates the limited precision of the Breit-Wigner model for the $1^+[\rho(770)\pi]_S$ wave. The intensity discontinuity at 1.53 GeV does not result in a discontinuity in the phase.

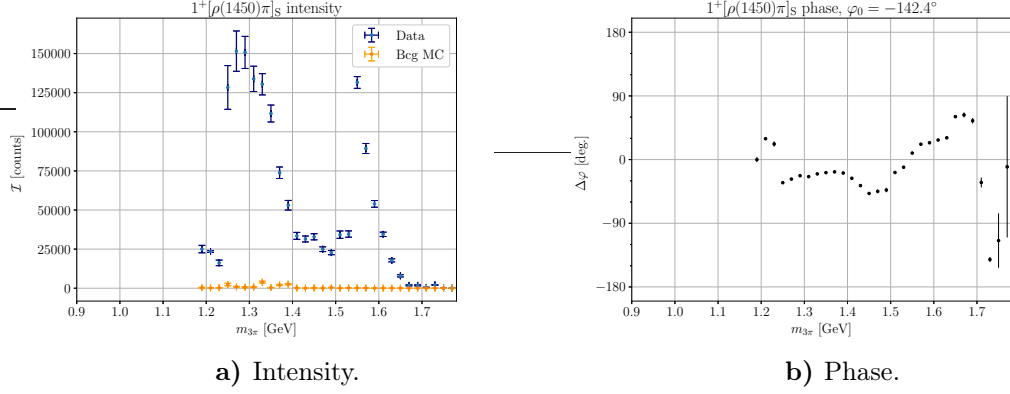


Figure 22: $1^+[\rho(1450)\pi]_S$ wave. The color scheme is the same as in Fig. 21.

Fig. 23 shows the $1^+[f_0(1500)\pi]_P$ wave. The threshold on this wave is set to 1.24 GeV. Below 1.5 GeV, the wave acts effectively as a complex-valued constant isobar with $1^+[0^{++}\pi]_P$ quantum numbers and compensates the limited precision of the $f_0(500)$ model. Above 1.5 GeV, the smooth phase increase by 90° indicates the presence of the $a_1(1640)$ resonance. There is a notable outlier at 1.53 GeV in the intensity plot.

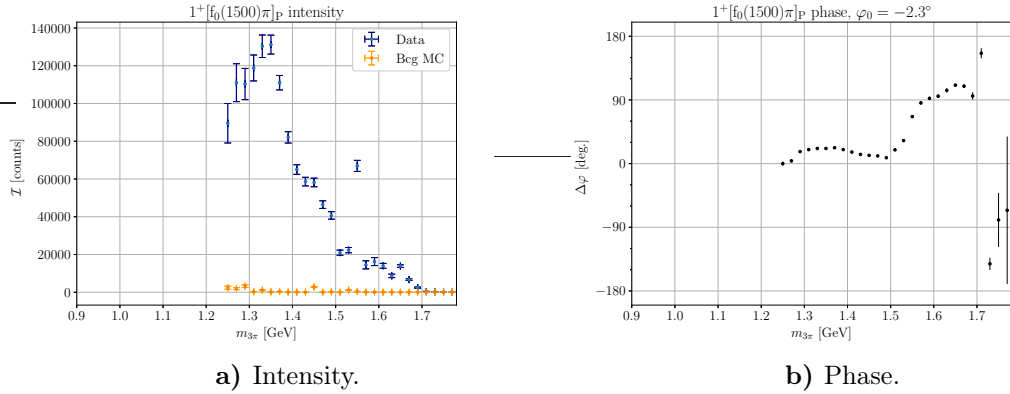


Figure 23: $1^+[f_0(1500)\pi]_P$ wave. The color scheme is the same as in Fig. 21.

7 Results

Fig. 24 shows the $1^+[\rho(770)\pi]_D$ wave. Peak structures at 1.15 GeV and 1.5 GeV are observed. These peaks, however, cannot be clearly attributed to the $a_1(1260)$ and $a_1(1640)$ resonances, because the relative phase smoothly decreases from approximately -120° at $m_{3\pi} = 1.05$ GeV by 60° at $m_{3\pi} = 1.5$ GeV. This phase variation shown in Fig. 24b appears due to the $a_1(1260)$ resonance in the $1^+[\rho(770)\pi]_S$ wave. There is a small background leakage at 1.25–1.4 GeV, which adds slight noise to the intensity but has little effect on the phase. The discontinuity at 1.53 GeV appears both in intensity and phase, which has unclear nature. Typically such a discontinuity is observed at the thresholds of the partial waves, however, at 1.53 GeV all waves are included into the PWA. Most likely this behavior is caused by the numerical precision of the fitter and the multimodal nature of the $\ln \mathcal{L}$ function.

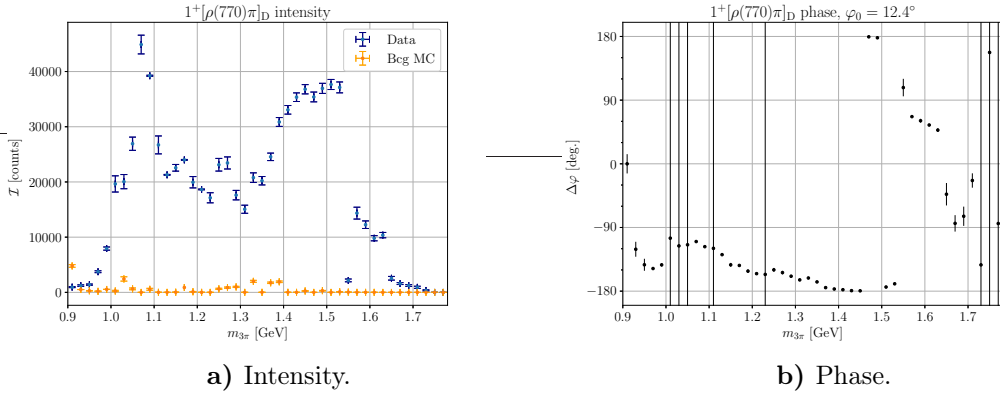


Figure 24: $1^+[\rho(770)\pi]_D$ wave. The color scheme is the same as in Fig. 21.

Large error bars in Fig. 24b at 1.0–1.05 GeV, 1.1 GeV, 1.23 GeV, and above 1.71 GeV are artificially set to 360° to indicate that the Gaussian error propagation from measured real and imaginary parts of \mathcal{C}_w returns an unphysical result. The error propagation $\delta\varphi$ of the relative phase φ is performed as follows:

$$x := \Re \mathcal{C}_w, \quad (7.4)$$

$$y := \Im \mathcal{C}_w, \quad (7.5)$$

$$\nabla := \frac{1}{1 + (y/x)^2} \begin{pmatrix} 1/x \\ -y/x^2 \end{pmatrix}, \quad (7.6)$$

$$\delta\varphi := \sqrt{\nabla^\top \text{cov}_{xy} \nabla}. \quad (7.7)$$

$\delta\varphi$ is unphysical if $\Re \mathcal{C}_w$ is zero, or the 2×2 covariance matrix cov_{xy} is not positive

definite. To avoid a bias in the resonance-model fit due to unphysical $\delta\varphi$ values, one should fit directly to \mathcal{C}_w extracted in PWA.

Fig. 25 shows the $1^+[\rho(1450)\pi]_D$ wave. The $1^+[\rho(1450)\pi]_D$ wave threshold is set to 1 GeV. The threshold on the $1^+[\rho(1450)\pi]_S$ wave causes the intensity discontinuity at 1.2 GeV, and below the $1^+[\rho(1450)\pi]_S$ threshold, the $1^+[\rho(1450)\pi]_D$ intensity could be considered as unphysical. The phase rise by more than 90° above 1.5 GeV might indicate the presence of the $a_1(1640)$ resonance. The intensity in this region is above zero, however it has a discontinuity at 1.53 GeV similar to what can be found in the $1^+[\rho(1450)\pi]_S$ intensity.

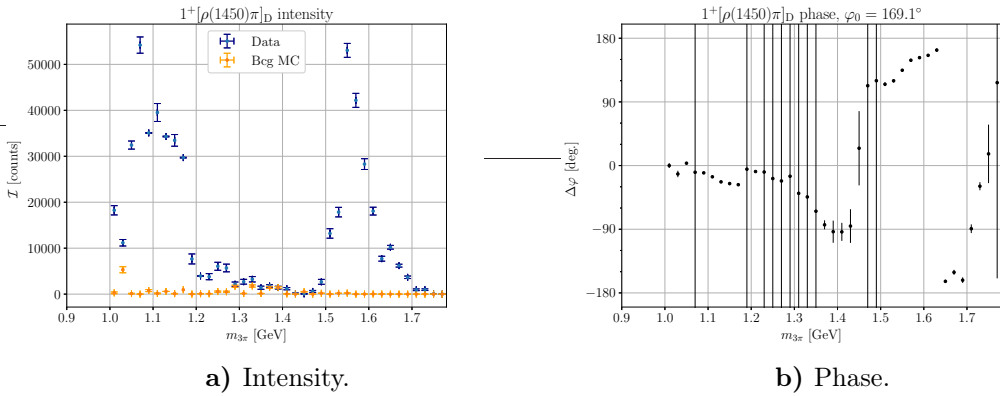


Figure 25: $1^+[\rho(1450)\pi]_D$ wave. The color scheme is the same as in Fig. 21.

Fig. 26 shows the $1^+[f_2(1270)\pi]_P$ wave. The threshold on this wave is set to 1.1 GeV. The intensity shown in Fig. 26a reveals notable background leakage into this wave near 1.3 GeV. The peak structure at 1.3 GeV could originate from the $a_1(1260)$ resonance. The phase shown in Fig. 26b is locked to the $1^+[\rho(770)\pi]_S$ wave in the [1.1, 1.45] GeV region with some variations below 30° . At 1.53 GeV, the intensity turns to be zero and thus at this $m_{3\pi}$ the phase is effectively undefined. After 1.53 GeV, there is an effective sign flip in the phase. Another phase jump appears at 1.63 GeV, which again corresponds to zero intensity.

Fig. 27 shows the $1^+[f_0(980)\pi]_P$ wave. The wave's threshold is set to 1.12 GeV. Both the intensity (Fig. 27a) and the relative phase (Fig. 27b) clearly contain an $a_1(1420)$ resonance-like structure in the [1.3, 1.5] range of $m_{3\pi}$. Below 1.3 GeV one observes the increasing intensity which resembles the $a_1(1260)$ resonance, however, the relative phase in this region is falling.

The presence of the $f_0(980)$ in the $1^+[0^{++}\pi]_P$ wave in the [1.3, 1.5] GeV range will be verified later in this thesis with the freed-isobar PWA.

Fig. 28 shows the $1^+[f_2(1270)\pi]_F$ wave. The threshold of this wave is set to

7 Results

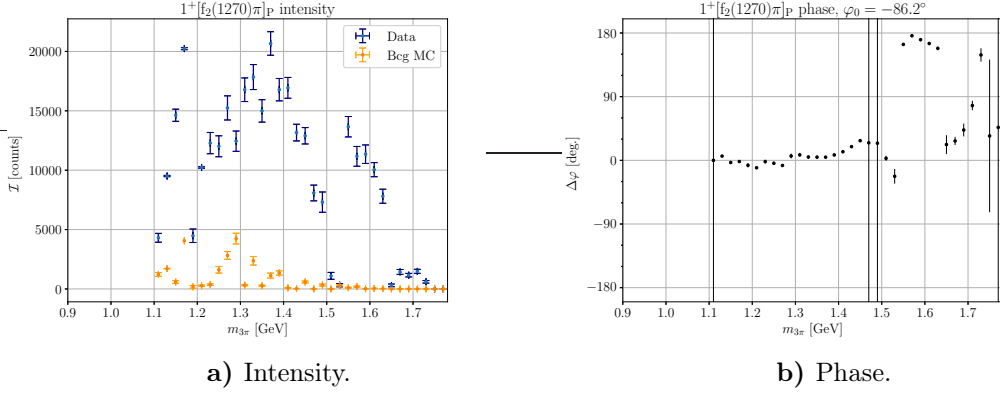


Figure 26: $1^+[f_2(1270)\pi]_P$ wave. The color scheme is the same as in Fig. 21.

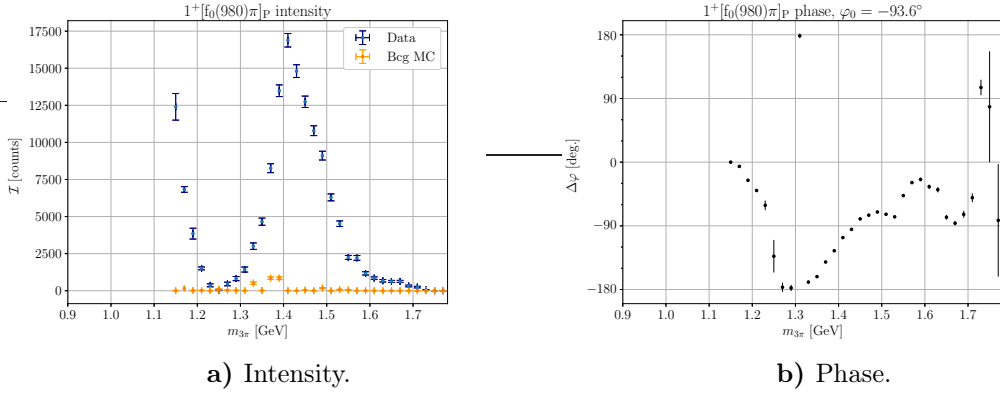


Figure 27: $1^+[f_0(980)\pi]_P$ wave. The color scheme is the same as in Fig. 21.

0.9 GeV. The intensity in Fig. 28a is above the possible background leakage in the [1.05, 1.4] GeV region. The intensity is distorted with the $1^+[\rho(1450)\pi]_S$, $1^+[\rho(1450)\pi]_D$, and $1^+[f_0(1500)\pi]_P$ wave thresholds. Overall, the $1^+[f_2(1270)\pi]_F$ wave has the lowest intensity among all in the $J^P = 1^+$ sector, therefore the statistical fluctuations are clearly visible. There is a small outlier at 1.53 similar to other waves in this sector. The phase in Fig. 28b increases in the [1.05, 1.3] GeV range, which may correspond to the $a_1(1260)$ resonance. The phase is effectively undefined above 1.4 GeV because the intensity is close to zero.

7.1 Partial-wave decomposition

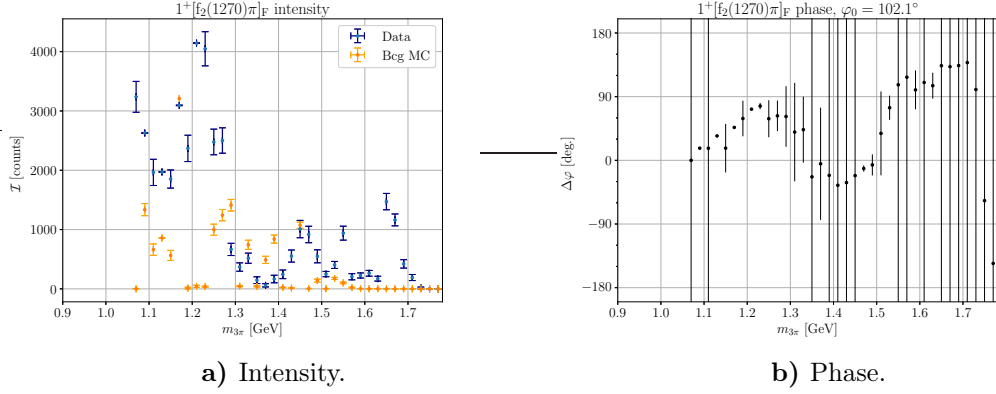


Figure 28: $1^+ [f_2(1270)\pi]_P$ wave. The color scheme is the same as in Fig. 21.

7.1.1.2 0^- sector

Fig. 29 shows the $0^- [\rho(770)\pi]_P$ wave. In the intensity plot (Fig. 29a) the large impact of the background leakage is observed for $m_{3\pi} < 1.4$ GeV. For the region above 1.4 GeV, significant intensity is observed, but there is no phase increase in the same region to indicate a resonance-like structure. Such large intensity could be explained if there is a background process that is not properly simulated at Belle and therefore could not be modeled by the neural network.

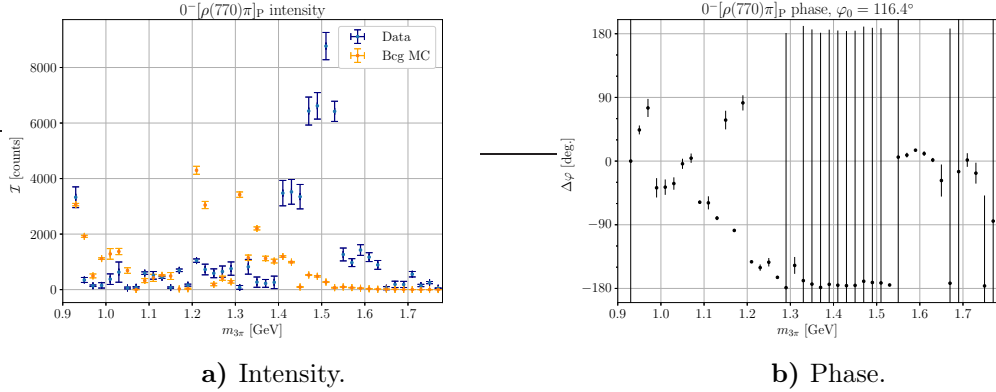


Figure 29: $0^- [\rho(770)\pi]_P$ wave. The color scheme is the same as in Fig. 21.

Fig. 30 shows the $0^- [\sigma\pi]_S$ wave. Most of the intensity can be explained with the background leakage, except only the small peak at 1.5 GeV.

7 Results

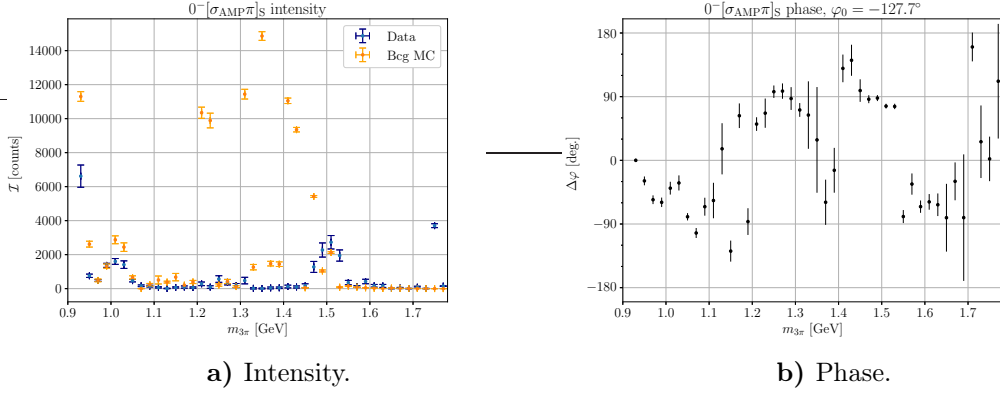


Figure 30: 0⁻[σπ]_S wave. The color scheme is the same as in Fig. 21.

Fig. 31 shows the 0⁻[f₂(1270)π]_D wave. The threshold of this wave is set to 1 GeV. The observed signal in the 0⁻[f₂(1270)π]_D wave can be fully explained with the background leakage.

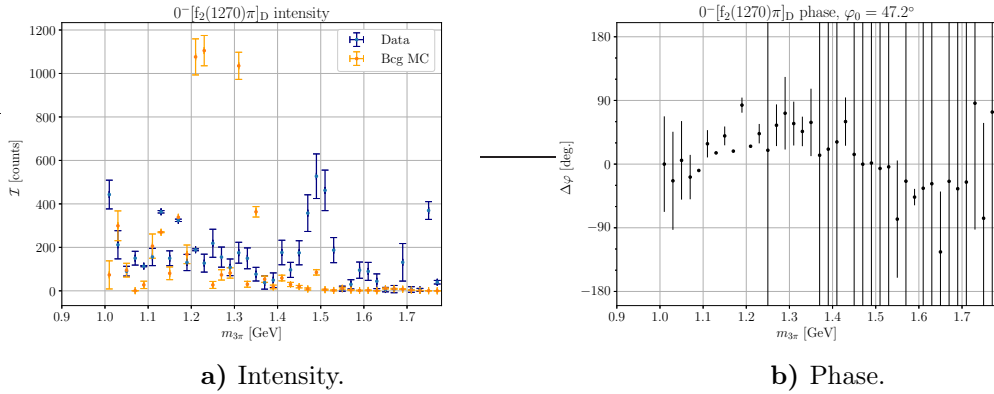


Figure 31: 0⁻[f₂(1270)π]_D wave. The color scheme is the same as in Fig. 21.

Fig. 32 shows the 0⁻[f₀(980)π]_S wave. The threshold on this wave is set to 1.14 GeV. No notable signal is observed in this wave.

No clear signal of the π(1300) resonance is observed in the $J^P = 0^-$ sector.

7.1.1.3 1⁻ sector

The inclusion of the 1⁻[ω(782)π]_P wave is motivated by a notable discrepancy at $s_1 \approx 0.6 \text{ GeV}^2$ in the comparison of the real data with the simulated data when the

7.1 Partial-wave decomposition

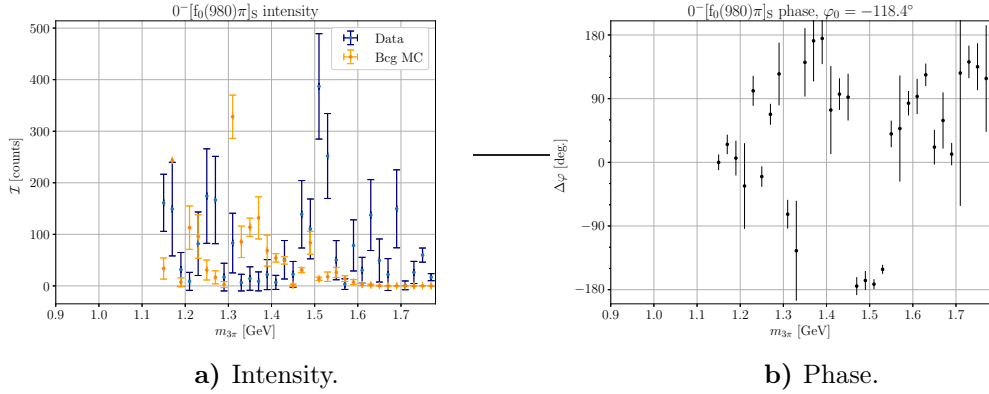


Figure 32: $0^- [f_0(980)\pi]_S$ wave. The color scheme is the same as in Fig. 21.

$1^- [\omega(782)\pi]_P$ wave was not taken into account (Fig. 33). A similar discrepancy was found for the s_2 phase-space variable. Because the discrepancy was observed in a narrow region near $m_{23} = 780$ MeV one could suspect the presence of the $\omega(782)$ resonance at this region.

It is known from the ρ - ω interference [79, 80] that $\omega(782)$ can decay to $\pi^+\pi^-$; this process violates G -parity and according to PDG [69] the branching fraction of $\omega(782) \rightarrow \pi^+\pi^-$ is 1.53 ± 0.06 %. The source of $\omega(782)$ in tauon decays could be the $\tau^- \rightarrow \omega(782)\pi^-\nu_\tau$ process with the branching fraction of 1.95 ± 0.06 % according to PDG [69]. By combining these two processes, one gets the same final state of $\pi^-\pi^-\pi^+\nu_\tau$ as the signal. The combined G -parity of the $\omega(782)\pi^-$ state implies the X^- resonance shall have $J^P = 1^-$ quantum numbers, and the angular momentum between $\omega(782)$ and π^- $L = 1$, thus $\omega(782)$ in $\tau^- \rightarrow \pi^-\pi^-\pi^+\nu_\tau$ is produced in the $1^- [\omega(782)\pi]_P$ wave.

The $1^- [\omega(782)\pi]_P$ branching fraction,

$$\mathcal{B}(1^- [\omega(782)\pi]_P) = \frac{\mathcal{B}(\tau^- \rightarrow \omega(782)\pi^-\nu_\tau)\mathcal{B}(\omega(782) \rightarrow \pi^-\pi^+)}{\mathcal{B}(\tau^- \rightarrow \pi^-\pi^-\pi^+\nu_\tau)} = 0.3\%, \quad (7.8)$$

which matches the measured value of 0.32% in Table 12.

Fig. 34 shows the $1^- [\omega(782)\pi]_P$ -wave complex amplitude. Fig. 34a resembles the $\omega(782)\pi^-$ spectrum from the CLEO II analysis of $\tau^- \rightarrow \pi^-\pi^-\pi^+\pi^0\nu_\tau$ [81] and could be described as interference of $\rho(770)$, $\rho(1450)$, and $\rho(1700)$ resonances. The relative phase shown in Fig. 34b does not change much which means it has locked phase with the $1^+ [\rho(770)\pi]_S$ wave. Whether such phase behavior can be reproduced in the resonance model or not will be revealed with the resonance-model fit.

7 Results

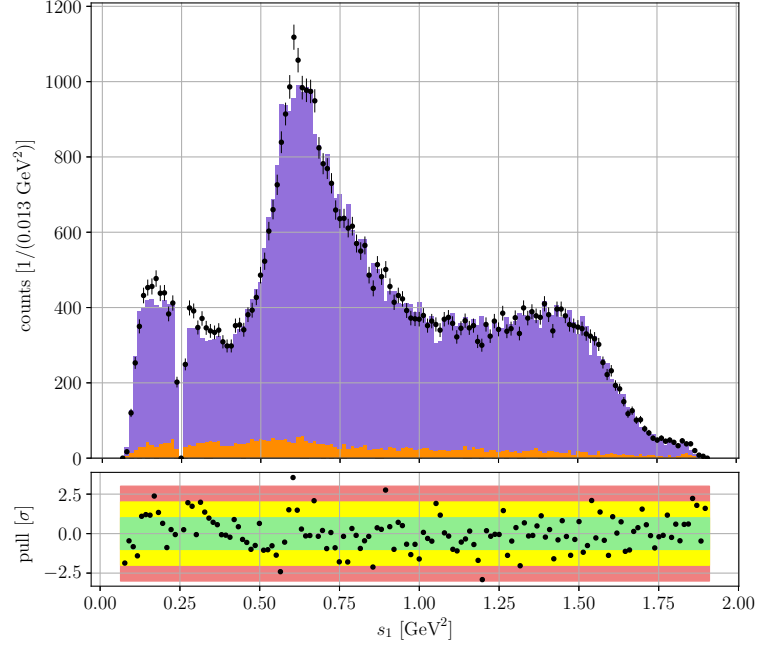


Figure 33: Comparison of the real data and simulated data for the $s_1 = m_{23}^2$ phase-space variable. $m_{3\pi} \in [1.50, 1.52]$ GeV. Black dots show the real data, orange histogram shows the simulated background, and violet histogram stacked on top of orange histogram shows the simulated signal. Simulation of the signal does not include the $1^-[\omega(782)\pi]_P$ wave.

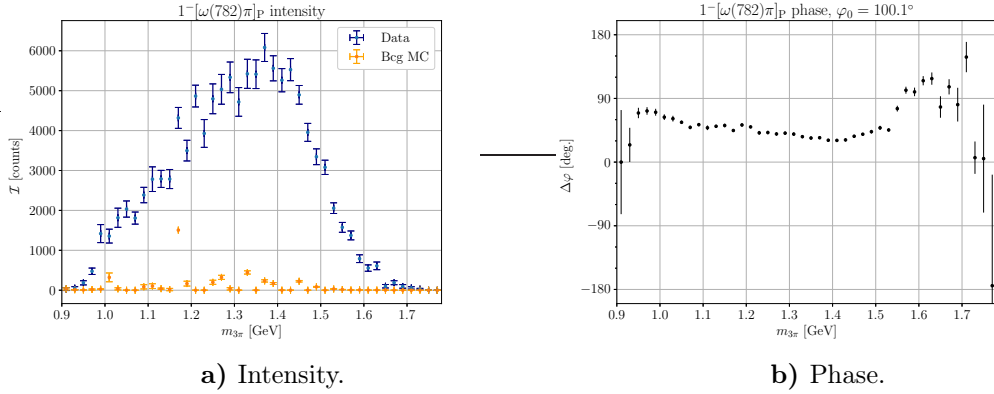


Figure 34: $1^+[\omega(782)\pi]_S$ wave. The color scheme is the same as in Fig. 21.

7.1 Partial-wave decomposition

Fig. 35 shows the $1^-[f_2(1270)\pi]_D$ wave. In the $m_{3\pi}$ range from 1.16 GeV to 1.4 GeV, the intensity of the $1^-[f_2(1270)\pi]_D$ wave can be explained with the background leakage. More detailed studies are needed of the $\tau^- \rightarrow \pi^- \pi^- \pi^+ \pi^0 \nu_\tau$ process which could be the source of the $1^-[f_2(1270)\pi]_D$ wave in this analysis.

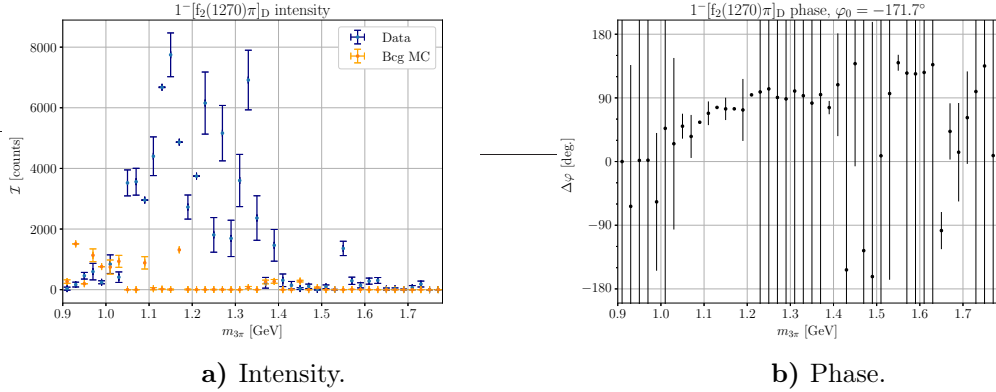


Figure 35: $1^-[f_2(1270)\pi]_D$ wave. The color scheme is the same as in Fig. 21.

Fig. 36 shows the $1^-[\rho(770)\pi]_P$ wave. The region below 1.4 GeV is contaminated with background. Above 1.4 GeV, there is a notable excess of data over background in Fig. 36a; also, there is a phase jump by more than 90° which might indicate a presence of the spin-exotic resonance $\pi_1(1600)$ studied in detail by COMPASS in [82]. The presence of $\pi_1(1600)$ in $\tau^- \rightarrow \pi^- \pi^- \pi^+ \nu_\tau$ could hint to the existence of the second-class current described by Weinberg in [83], however, this requires detailed studies of this process from both experimental and theoretical sides which is out of the scope of this thesis.

7.1.2 Freed-isobar PWA

To verify the existence of $a_1(1420)$ in $\tau^- \rightarrow \pi^- \pi^- \pi^+ \nu_\tau$, one needs to perform the freed-isobar PWA with the freed $1^+[0^{++}\pi]_P$ wave. To avoid a bias from the $\rho(770)$ modeling one needs to free also the $1^+[1^{--}\pi]_S$ wave, because the $1^+[\rho(770)\pi]_S$ wave dominates the $\tau^- \rightarrow \pi^- \pi^- \pi^+ \nu_\tau$ decay. The existence of $a_1(1420)$ will be verified if in the freed-isobar fit the $f_0(980)$ isobar is present in the $1^+[0^{++}\pi]_P$ wave and the three-body complex amplitude of the $1^+[f_0(980)\pi]_P$ wave has the same behavior in the freed- and fixed-isobar PWA.

In the fixed-isobar PWA, the $1^+[\rho(770)\pi]_S$ wave is an anchor wave and its imaginary part is set to zero. In this freed-isobar PWA, the $1^+[\rho(770)\pi]_S$ wave is freed

7 Results

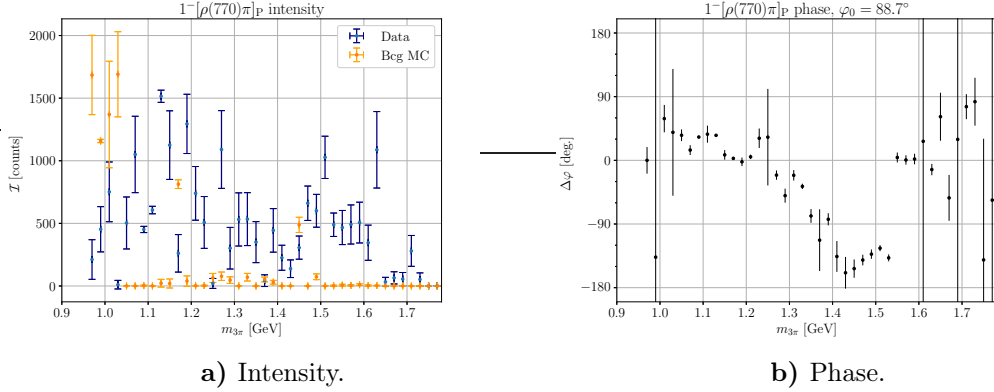


Figure 36: $1^-[\rho(770)\pi]_P$ wave. The color scheme is the same as in Fig. 21.

and therefore cannot be used as an anchor wave. The $1^+[\rho(770)\pi]_D$ wave is the anchor wave and its imaginary part is set to zero.

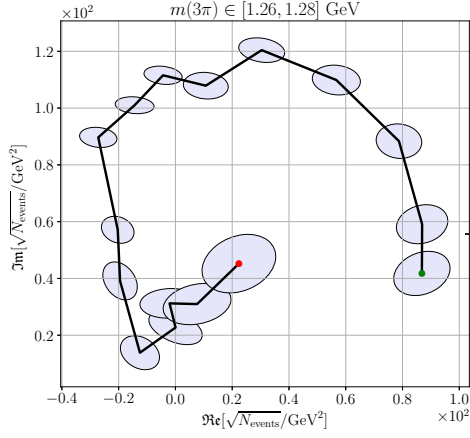
After the partial-wave decomposition, the isobars fits to the $1^+[1^{--}\pi]_S$ and $1^+[0^{++}\pi]_P$ waves are performed. The isobar fit program [84] also resolves zero modes as described in [60]. The zero-modes resolution is done in two steps. First, the $1^+[1^{--}\pi]_S$ wave is fitted with a single $\rho(770)$ isobar, and the zero-mode is determined by setting the resulting complex constant of the $\rho(770)$ isobar to zero. Then, $1^+[0^{++}\pi]_P$ is fitted with the sum of the Kachaev function [72] to describe the broad $[\pi\pi]_S$ wave component and with the Breit-Wigner function to describe $f_0(980)$.

Some obtained Argand diagrams are shown in Fig. 37. The $f_0(500)$ isobar dominates the $1^+[0^{++}\pi]_P$ wave for $m_{3\pi} < 1.35$ GeV as shown in Fig. 37a, and the $f_0(980)$ isobar dominates the $1^+[0^{++}\pi]_P$ wave if $m_{3\pi}$ is close to 1.4 GeV as shown in Fig. 37c. $\rho(770)$ dominates $1^+[1^{--}\pi]_S$ wave as shown in Figs. 37b and 37d. The broad tail in the high $m(2\pi)$ masses of the $1^+[1^{--}\pi]_S$ wave could indicate the presence of the $\rho(1450)$ resonance.

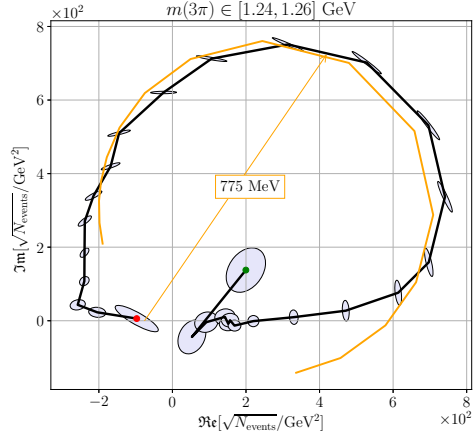
Fig. 37 demonstrates the notable discrepancy between the fitted curves and the data. This indicates a need to improve our understanding of the $[\pi\pi]_P$ and $[\pi\pi]_S$ waves. However, the existing models describe the real data qualitatively, and we can look how the three-pion complex amplitude $\mathcal{C}_{w \text{ output}}$ depend on $m_{3\pi}$ after the isobar fit.

In the three-pion amplitude shown in Fig. 38, $a_1(1420)$ is observed as a peak in the intensity in Fig. 38b and as a phase rise in Fig. 38d at approximately 1.4 GeV of the $1^+[f_0(980)\pi]_P$ wave. The wave behavior differs in the freed- and fixed-isobar PWA in Fig. 27 for the region below 1.25 GeV near the kinematic threshold of

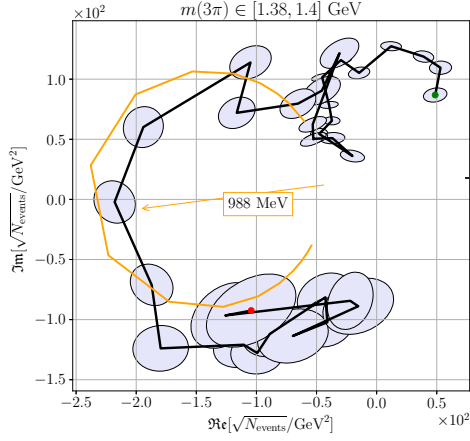
7.1 Partial-wave decomposition



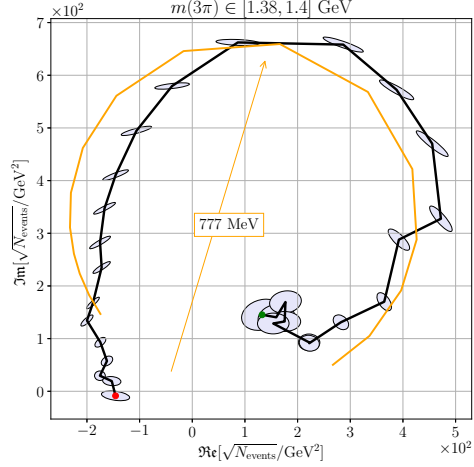
a) $1^+[0^{++}\pi]_P$ wave.



b) $1^+[1^{--}\pi]_S$ wave.



c) $1^+[0^{++}\pi]_P$ wave.



d) $1^+[1^{--}\pi]_S$ wave.

Figure 37: Argand diagrams for the freed fit PWA (dots with errorbars), zero-modes fixing (blue line), and isobar fit (pink line). Top row corresponds to $m(3\pi) \in [1.26, 1.28]$ GeV, bottom row corresponds to $m(3\pi) \in [1.38, 1.40]$ GeV.

the wave. The $a_1(1260)$ resonance dominates the $1^+[\rho(770)\pi]_S$ wave and is visible as a broad peak structure at 1.15 GeV in the intensity plot in Fig. 38a. Fig. 38c shows the phase relative to the $1^+[\rho(770)\pi]_S$ wave. A smooth phase rise by 90° is observed at 1.55 GeV which might indicate the presence of the $a_1(1640)$ resonance. These results agree with the fixed-isobar PWA.

7 Results

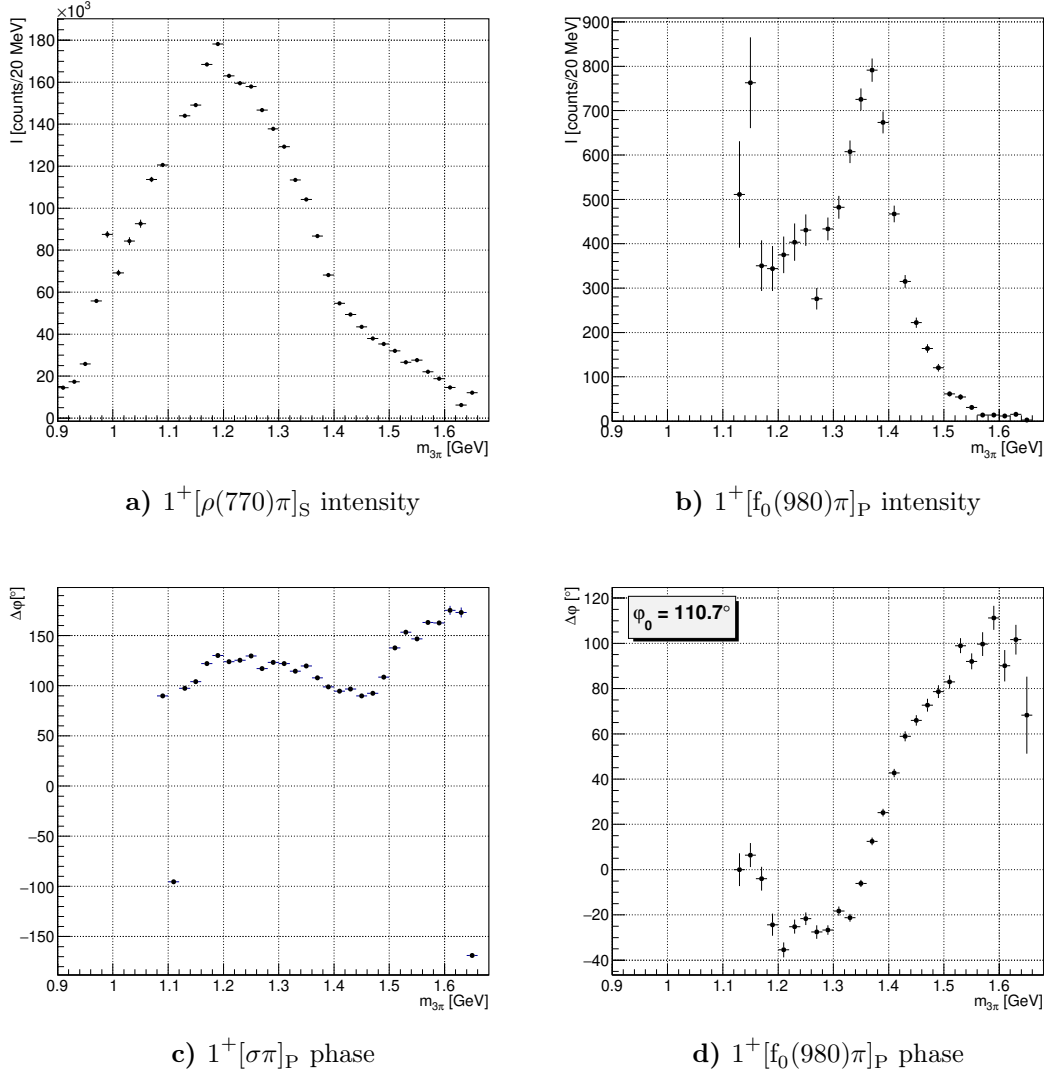


Figure 38: Partial-wave amplitudes \mathcal{C}_w extracted in the isobar fit to the freed-isobar PWA. $1^+[\rho(770)\pi]_S$ intensity is shown in Fig. a, $1^+[f_0(980)\pi]_P$ intensity is shown in Fig. b, $1^+[f_0(980)\pi]_P$ phase is shown in Fig. d, and $1^+[\sigma\pi]_P$ phase is shown in Fig. c. The phases are calculated relative to the $1^+[\rho(770)\pi]_S$ wave.

7.2 Resonance-model fit

To extract the parameters of $a_1(1260)$ and $a_1(1420)$ I fit the resonance-model to the complex amplitudes obtained in the partial-wave decomposition.

Fig. 39 demonstrates one attempt in the series of the resonance-model fits. I fit

only to three partial waves: $1^+[f_0(980)\pi]_P$, $1^-[\omega(782)\pi]_P$, and $1^+[\rho(770)\pi]_S$. The $1^+[\rho(770)\pi]_S$ wave dominates the $\tau^- \rightarrow \pi^- \pi^- \pi^+ \nu_\tau$ and thus determines the χ^2/ndf value. Adding $a_1(1640)$ improves the χ^2/ndf of the resonance-model fit, but the fit cannot find the mass and width of the $a_1(1640)$ resonance, and they are fixed. I use the COMPASS model for the $a_1(1260)$ to compare directly the obtained parameters. The obtained mass m and width Γ of the $a_1(1260)$ resonance are

$$m = 1328.9 \pm 0.1, \quad (7.9)$$

$$\Gamma = 388.4 \pm 0.1. \quad (7.10)$$

Only statistical uncertainties are given. The mass and width agree with the COMPASS values within the COMPASS systematic uncertainties [8].

The $1^-[\omega(782)\pi]_P$ wave is described as the coherent sum of $\rho(770)^-$, $\rho(1450)^-$, and $\rho(1700)^-$ resonances as it was done by CLEO II in [81]. All ρ^- resonances in this fit are modeled with the Gounaris-Sakurai model, and their parameters are taken from [85] and fixed in the fit. Some discrepancy between PWA and the resonance model is observed for the intensity of the $1^-[\omega(782)\pi]_P$ wave, which can be explained that the model includes only a single decay channel for the $\rho(1450)^-$ resonance and a more elaborate model for the $\rho(1450)^-$ resonance is required. However, this model agrees with the measured relative phase of $1^-[\omega(782)\pi]_P$ wave.

The $a_1(1420)$ is modeled by the Breit-Wigner formula with $J = 1$ without taking into account the Blatt-Weisskopf barrier factors. Additional complex constant is used to take into account other possible states decaying to $1^+[f_0(980)\pi]_P$. The yield of the $a_1(1420)$ amplitude relative to the $a_1(1260)$ amplitude is 3×10^{-3} . The obtained mass m and width Γ of the $a_1(1420)$ resonance are

$$m = 1387.8 \pm 0.3[\text{MeV}], \quad (7.11)$$

$$\Gamma = 109.2 \pm 0.6[\text{MeV}]. \quad (7.12)$$

Only statistical uncertainties are given. The mass and width are lower than the COMPASS values [8] by 23 MeV and 51 MeV correspondingly. This discrepancy is significant but can be explained by the presence of coherent Deck background in COMPASS data.

7 Results

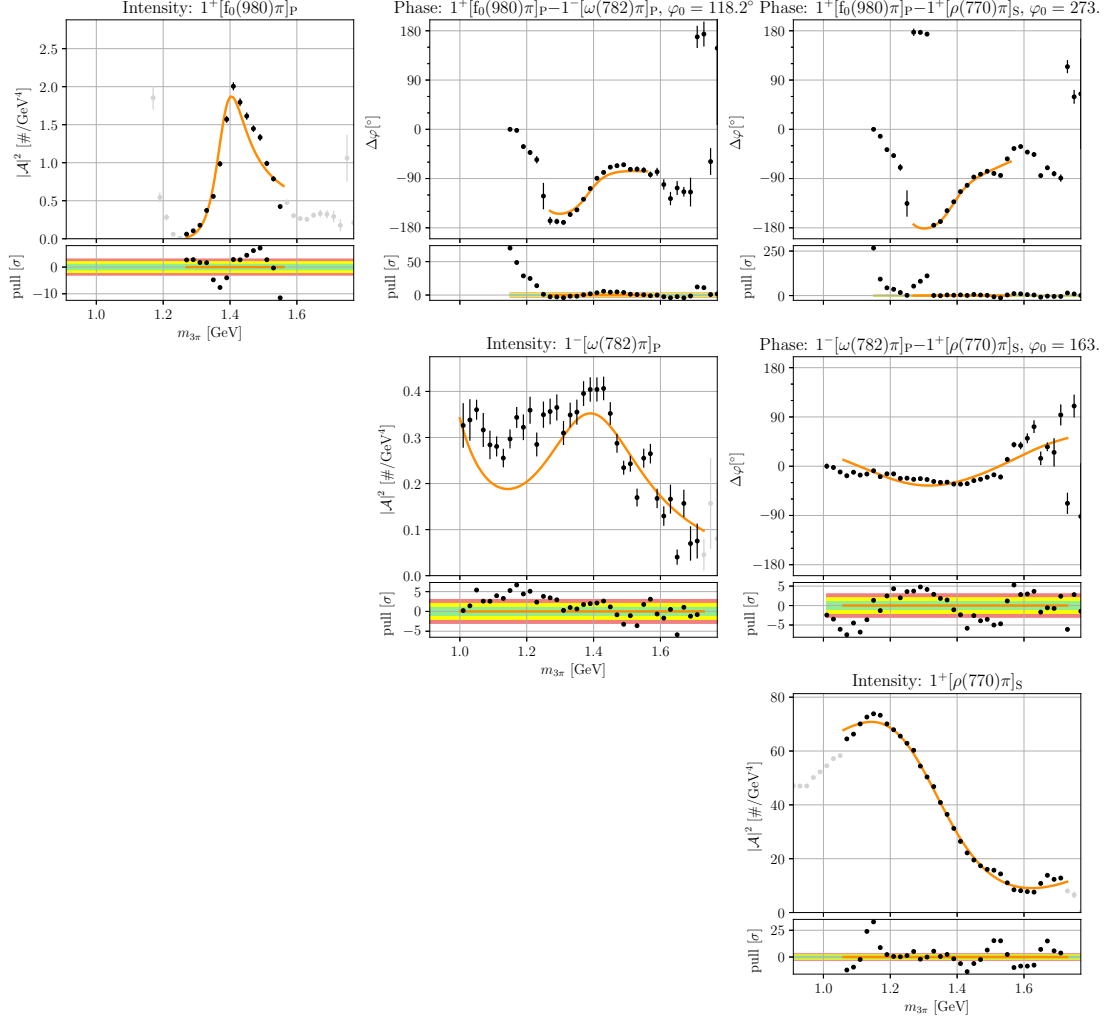


Figure 39: Resonance-model fit to three partial waves: $1^+[f_0(980)\pi]_P$, $1^-[\omega(782)\pi]_P$ and $1^+[\rho(770)\pi]_S$. The diagonal plots show the intensities dependence on $m_{3\pi}$, and the non-diagonal plots show the relative phases dependence on $m_{3\pi}$. Black dots with error bars are the results of the partial-wave decomposition, corrected with the $m_{3\pi}$ efficiency and the phase space. Orange curve shows the resonance-fit model. At the bottom of each plot the auxiliary pull plot is shown. It's \mathcal{Y} -axis is in units of the statistical uncertainties of the partial-wave decomposition fit.

8 Systematic uncertainties

There are four major sources of the systematic uncertainties: the fit model, background, acceptance, and detector resolution. This is similar to what CLEO II considered in their analysis [9].

8.1 Fit model

Different isobar models produce different results of the partial-wave decomposition. For example, variations of the meson radius d in the conventional partial-wave decomposition lead to a different shape of the $1^+[f_0(980)\pi]_P$ wave intensity (Fig. 40a) although it still peaks at 1.4 GeV and has a narrow structure. The phase relative to the $1^+[\rho(770)\pi]_S$ wave differs slightly as shown in Fig. 40b. Nevertheless, because of the large intensity difference it might be difficult to figure out whether the nature of $a_1(1420)$ is the re-scattering of K^*K , or it is an exotic particle.

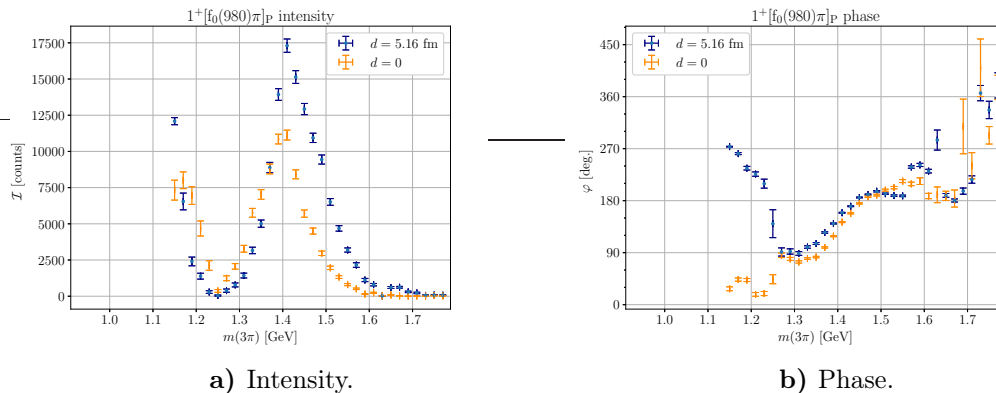


Figure 40: Partial-wave decomposition of the real data, $1^+[f_0(980)\pi]_P$ wave. Blue dots correspond to the model which includes the Blatt-Weisskopf centrifugal-barrier factors in the isobar parametrization with the meson radius $d = 1$ fm, and orange dots correspond to the model which does not include these factors.

Fig. 41 shows the difference of $\ln \mathcal{L}$ in the fit maxima between the partial-wave

8 Systematic uncertainties

decomposition results modeled without or with taking into account the Blatt-Weisskopf centrifugal-barrier factors. In the region below 1.4 GeV the data is better described without the Blatt-Weisskopf factors, while in the region above 1.4 GeV one achieves a better fit quality by taking the Blatt-Weisskopf factors. This effect can be explained by the increased significance of the waves with S or L equal or above 2. However, this figure shows that one cannot prefer one parametrization of isobars over the other, thus the discrepancy between these two models highlights the model uncertainty.

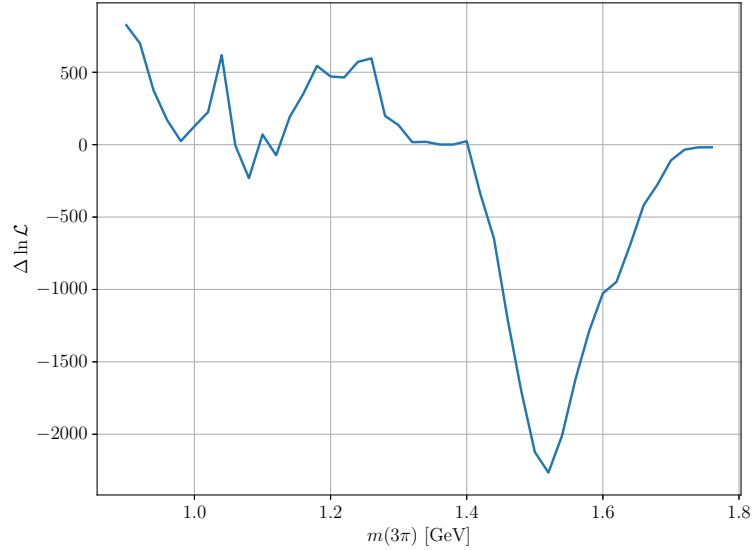


Figure 41: Difference of $\ln \mathcal{L}$ of the partial-wave decomposition results modeled with $d = 0$ and $d = 1$ fm as a function of $m_{3\pi}$.

8.2 Background

This analysis suffers from a relatively large background contamination, and it requires a better understanding of how background affects the result. In general, systematic uncertainty caused by the large background can be split into two sub-sources: the physics model of the MC used to simulate background response, and the background description method.

Systematic effects due to the physics model originate from the low precision measurement of cross-sections, branching fractions, and the overall shape of the processes being major background components to my analysis. In my case, background is mostly dominated by the $\tau \rightarrow 4\pi\nu_\tau$ decay for $m_{3\pi} < 1.3$ GeV and by

$e^+e^- \rightarrow q\bar{q}$ for $m(3\pi) > 1.3$ GeV, thus the relative branching fraction uncertainties can be neglected in contrast to the physics model of the background.

For example, the $\tau^- \rightarrow \pi^- \pi^- \pi^+ \pi^0 \nu_\tau$ model is based on Novosibirsk $e^+e^- \rightarrow 4\pi$ data, which is converted to the $\tau^- \rightarrow \pi^- \pi^- \pi^+ \pi^0 \nu_\tau$ model by applying the CVC hypothesis. It was shown in [86] that there is notable discrepancy between the MC modeled with the Novosibirsk current and the real data (see Fig. 42), which indicates that the model for the $\tau^- \rightarrow \pi^- \pi^- \pi^+ \pi^0 \nu_\tau$ decay is incomplete. It includes the two most dominant partial waves of the $a_1(1420)$ amplitude, $1^+[\rho(770)\pi]_S$ and $1^+[\sigma\pi]_P$, in the $\tau^- \rightarrow a_1(1260)\pi^- \nu_\tau$ process. The model includes also the $\tau^- \rightarrow \omega(782)\pi^- \nu_\tau$ process, however, it does not include such processes as $\tau^- \rightarrow \rho(770)^- \rho(770)^0 \nu_\tau$ or $\tau^- \rightarrow \rho(770)^- \sigma \nu_\tau$, which can impact the result of the $\tau^- \rightarrow \pi^- \pi^- \pi^+ \pi^0 \nu_\tau$ PWA via wrong background parametrization.

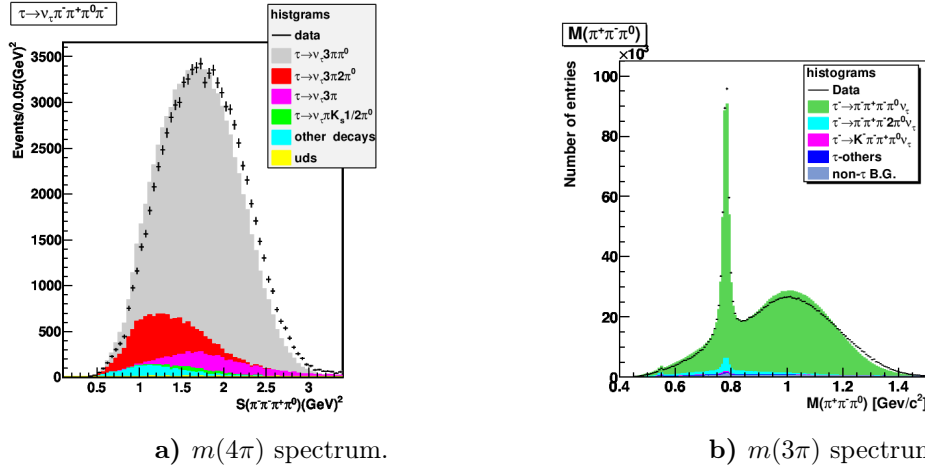


Figure 42: Spectra of $\tau^- \rightarrow 3\pi^\mp \pi^0 \nu_\tau$ decay. Pictures are taken from the preliminary study of the $\tau^- \rightarrow \pi^- \pi^- \pi^+ \pi^0 \nu_\tau$ decay at Belle [86].

Another source of systematic uncertainties in the background estimation comes from the parametrization method of the multi-dimensional background distribution. As a primary tool, I use the neural network parametrization which is fitted to the simulated background, and it might have not enough flexibility to describe all nuances of the background.

The background uncertainty is evaluated as follows. For each bin, I vary the neural network coefficients near its minimum in the training procedure, and effectively propagate the uncertainty on the coefficients by performing the partial-wave decomposition fit for each set of coefficients. The result is summarized in Fig. 43 for five major partial waves from the $J^P = 1^+$ sector. Shown are mean and standard deviations of the propagation procedure. The corresponding uncertainty is on the same scale as the statistical one.

8 Systematic uncertainties

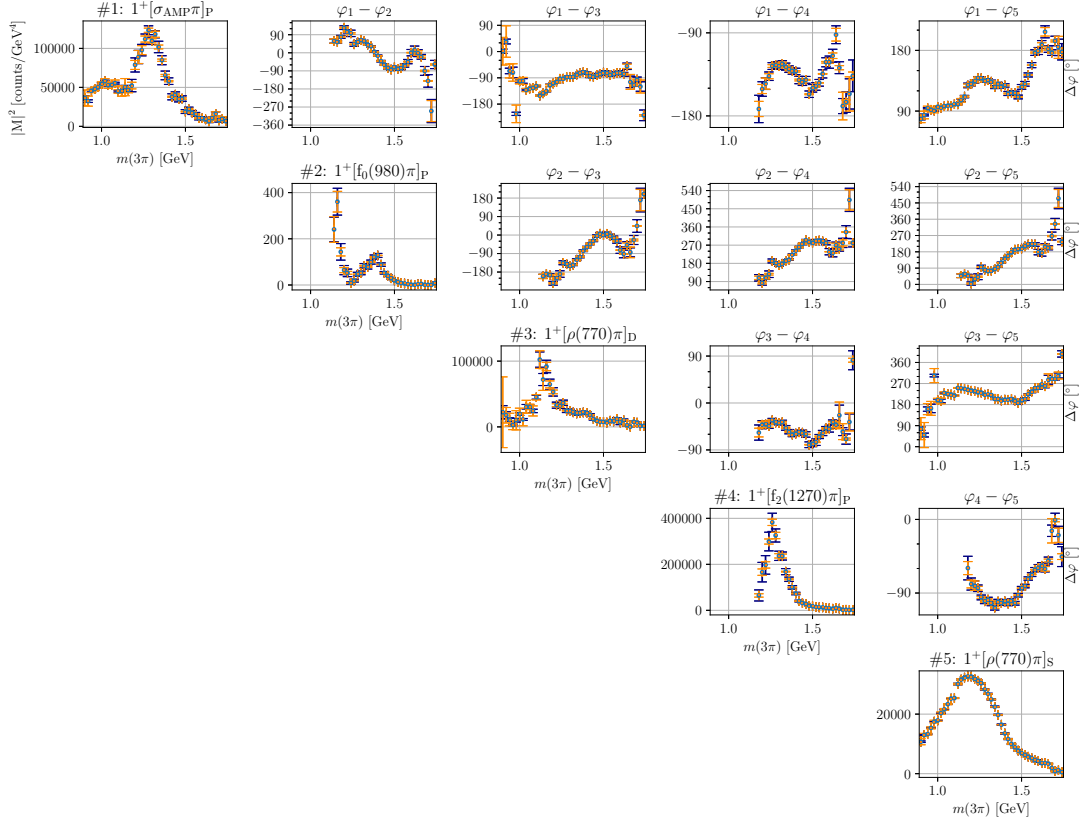


Figure 43: Systematic uncertainties for the neural network background. Statistical uncertainties are shown to be compared with. Blue color shows the statistical uncertainty, orange color shows the systematic uncertainty. The diagonal plots show the intensity dependence on $m_{3\pi}$, and the non-diagonal plots show the relative phases dependence on $m_{3\pi}$.

8.3 Acceptance

The detector acceptance is taken into account by the integrals, and it relies on the de-weighted generic MC.

The de-weighting procedure is cross-checked against the TAUOLA matrix element. No deviations were found within the numerical precision.

I use simulated data to evaluate integral matrices for the partial-wave decomposition. Due to the limited number of events in the simulated sample, the statistical uncertainties of the integrals are not negligible. I propagate it by sampling integrals according to their variances from simulated data, assuming Gaussian distribution. The resulting uncertainty, shown in Fig. 44, is larger than the statistical one, but the notable features of the partial-wave decomposition fit are kept.

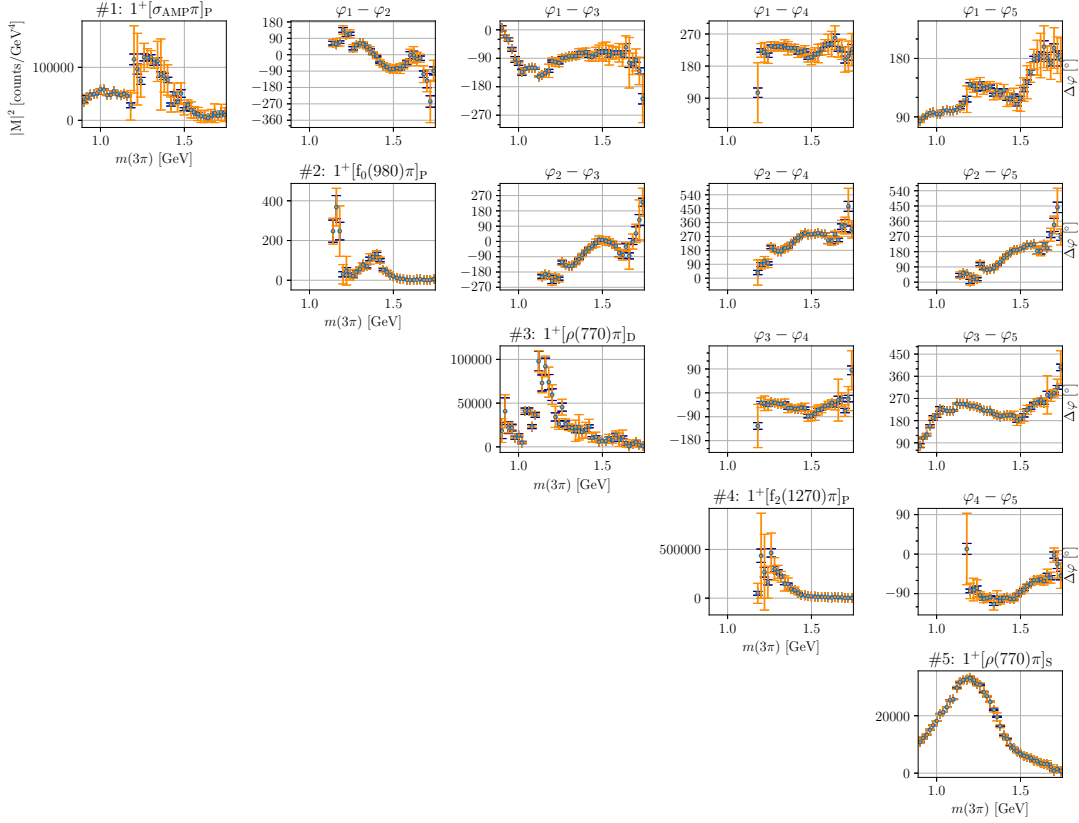


Figure 44: Systematic uncertainties due to the limited number of events used for the integral evaluation and statistical uncertainties. Blue color shows the statistical uncertainty, orange color shows the systematic uncertainty. The diagonal plots show the intensity dependence on $m_{3\pi}$, and the non-diagonal plots show the relative phases dependence on $m_{3\pi}$.

8.4 Resolution

I assume resolution effects are negligible. In principle, the effect of the resolution can be pre-calculated in the PWA, such that

$$\mathcal{I}_{wv}(\Phi_{\text{rec}}) = \int d\Phi_{\text{true}} \varepsilon(\Phi_{\text{true}}, \Phi_{\text{rec}}) \mathcal{I}_{wv}(\Phi_{\text{true}}), \quad (8.1)$$

where Φ_{rec} denotes the reconstructed phase space variables, Φ_{true} denotes the so-called true phase space variables, and $\varepsilon(\Phi_{\text{true}}, \Phi_{\text{rec}})$ is the detection efficiency as a function of true and reconstructed phase space variables. Unfortunately, there is no analytical function in 12-dimensional space which parametrizes $\varepsilon(\Phi_{\text{true}}, \Phi_{\text{rec}})$. For simplicity of the cross-check I assume that the resolution effects can be ap-

8 Systematic uncertainties

proximated such that

$$\varepsilon(\Phi_{\text{true}}, \Phi_{\text{rec}}) = \varepsilon(\Phi_{\text{true}} - \Phi_{\text{rec}}) \quad (8.2)$$

and there are no correlations between $\Phi_{\text{true}} - \Phi_{\text{rec}}$. Therefore, $\varepsilon(\Phi_{\text{true}}, \Phi_{\text{rec}})$ can be approximated as the product of one-dimensional templates of $\Phi_{\text{true}} - \Phi_{\text{rec}}$ obtained from the signal MC.

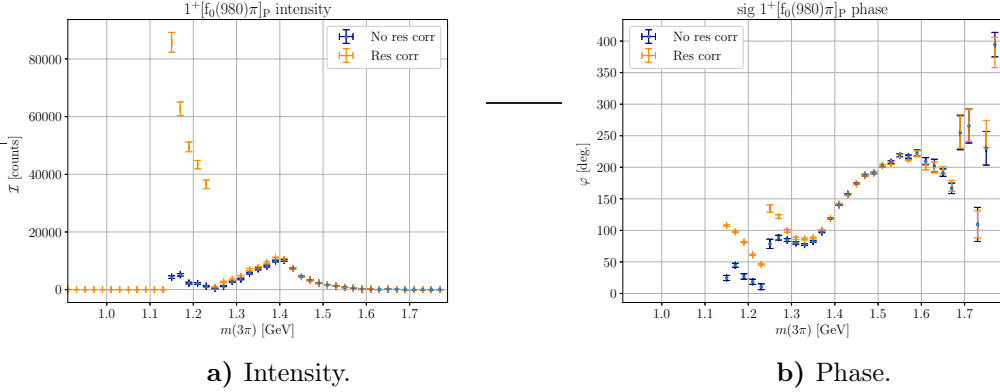


Figure 45: Partial-wave decomposition of the real data, $1^+[f_0(980)\pi]_P$ wave. Blue dots correspond to the model which neglects the resolution effects, and orange dots correspond to the model where the resolution effects are taken into account.

Fig. 45 shows the result of the partial-wave decomposition for the $1^+[f_0(980)\pi]_P$ wave with and without taking into account the resolution effects. Fig. 45a shows that the resolution effects impact the low mass of $m_{3\pi}$ of the intensity of the $1^+[f_0(980)\pi]_P$ wave, while in the region of $a_1(1420)$ there is almost no impact of the resolution onto the results. Fig. 45b shows that there is no resolution impact on the phase motion in the region of $a_1(1420)$. One can conclude that the resolution effects can be neglected for the reported $a_1(1420)$ parameters.

The resolution of the two-pion invariant mass, $m_{23, \text{true}} - m_{23, \text{rec}}$, can be approximated with the sum of two Gaussian functions,

$$\text{p.d.f.}(x) \propto e^{-\frac{(x-x_1)^2}{2\sigma_1^2}} + f e^{-\frac{(x-x_2)^2}{2\sigma_2^2}}, \quad (8.3)$$

such that $\sigma_1 = 2.24$ MeV, $\sigma_2 = 6.1$ MeV, and the relative strength of the second Gaussian function $f = 0.2$. For most of the isobars in the PWA the width is much larger than the resolution, however for $1^-[\omega(782)\pi]_P$ the resolution effects cannot be neglected.

9 Discussion

Before this analysis, there were concerns that a PWA of the $\tau^- \rightarrow \pi^- \pi^- \pi^+ \nu_\tau$ process would not be possible. The major concern was that the tau neutrino misses the detector, and therefore it is impossible to disentangle different partial waves. The MC studies in this analysis show that the averaging procedure does not introduce any bias into the partial-wave decomposition. Because of this I have decided to use the 3-1 topology with inclusive tag side to maximize the data sample. The total data sample reaches 55×10^6 events; this is the largest sample of $\tau^- \rightarrow \pi^- \pi^- \pi^+ \nu_\tau$ to date.

The second concern was about the relatively large background contribution identified during the data selection, about 13%. Such background contamination is unusual for a PWA. The first question was how to parametrize the background with a realistic physics model and unknown acceptance function. This analysis shows that the neural network approach minimizes the background leakage in the $m_{3\pi} > 1.05$ GeV range and keeps the background systematic uncertainty under control. There is still an open question whether the imprecise background model in the simulated data leads to a bias; the answer would require a PWA of $\tau^- \rightarrow \pi^- \pi^- \pi^+ \pi^0 \nu_\tau$. Neither the ongoing CMD-3 study of the $e^+ e^- \rightarrow 4\pi$ process nor the ongoing Belle study of the $\tau^- \rightarrow \pi^- \pi^- \pi^+ \pi^0 \nu_\tau$ is completed [86, 87]. This PWA will serve as an input to the CMD-3 and Belle analyses to better measure the four-pion vector current.

This analysis demonstrates a better performance of the BDT-based approach over the more traditional cut-based approach such that the resulting efficiency is 1.5 times larger than in the previous analysis of $\tau^- \rightarrow \pi^- \pi^- \pi^+ \nu_\tau$ at Belle [18]. The scheme of selecting first $e^+ e^- \rightarrow \tau^+ \tau^-$ and then selecting the signal process has now been adopted by some ongoing Belle and Belle II analyses.

This analysis also demonstrates the first use of the novel freed-isobar PWA technique in tau decays. The freed-isobar PWA validates the findings of the conventional partial-wave decomposition of $\tau^- \rightarrow \pi^- \pi^- \pi^+ \nu_\tau$. More generally, the freed-isobar PWA results offer quasi-model-independent experimental input for ongoing theoretical studies on the nature of the $f_0(500)$, $f_0(980)$ and $\rho(770)$ isobars.

The conventional PWA provides very detailed information about the hadron current. The statistical precision almost reaches the 1×10^{-4} level, such that we are capable of observing the unexpected signal in the $J^P = 1^-$ sector, which partially

9 Discussion

can be explained with the $1^-[\omega(782)\pi]_P$ wave. With such statistical precision, it is important to keep systematic uncertainties under control. It was shown that this analysis is limited by the systematic uncertainties, and the largest systematic uncertainty comes from the isobar model. This limitation was bypassed by using the freed-isobar PWA, and the observation of the $a_1(1420)$ was verified, but with lower statistical precision.

The discovery of $a_1(1420)$ in the $\tau^- \rightarrow \pi^- \pi^- \pi^+ \nu_\tau$ process does not conclude the debates on its nature, although it now seems that the K^*K re-scattering model is preferable over the exotic-meson one. Besides that, models of $\tau^- \rightarrow \pi^- \pi^- \pi^+ \nu_\tau$ will be clearly improved by including the $a_1(1420)$ resonance-like structure, which will be essential for precision tests of the Standard Model.

The value of the $a_1(1260)$ mass and width is a long-disputed issue. While the intensity of the $1^+[\rho(770)\pi]_S$ wave peaks at 1.15 GeV, which corresponds to the $a_1(1260)$ resonance, its mass is shifted towards the larger values in the resonance-model fit, $m = 1.331$ GeV. It is clear that the values of the $a_1(1260)$ mass and width depend on the model used in the resonance-model fit. The results of the partial-wave decomposition provide a quasi-model-independent experimental input for further theoretical studies of the $a_1(1260)$ resonance.

10 Conclusion

The isovector axial vector meson $a_1(1420)$ has been observed in the tauon decay for the first time. This observation was obtained in both conventional and freed-isobar PWA. The production proceeds in weak decays which is in contrast to COMPASS, where this meson is produced via strong interaction.

This work shows the significance of $a_1(1640)$ for the first time in an experimental study of the $\tau^- \rightarrow \pi^- \pi^- \pi^+ \nu_\tau$ process.

It is shown that the large spread of $a_1(1260)$ mass and width listed in PDG [11] originates from the different models used in the reported experimental studies.

The Au-Morgan-Pennington parametrization of the $[\pi\pi]_S$ wave with the Kachaev modification [72] was used for the first time in an analysis of a tauon decay. This parametrization fits the broad $[\pi\pi]_S$ component much better than a simple Breit-Wigner function. Another planned study based on this freed-isobar PWA will consider the $[\pi\pi]_P$ wave shape, which is also not well described by a simple Breit-Wigner function. A more sophisticated model is needed such as Gounaris-Sakurai [88]. The $\tau^- \rightarrow \pi^- \pi^- \pi^+ \nu_\tau$ freed-isobar PWA from this work provides a good laboratory for such studies.

The overall result is a very detailed picture of the hadron current, such that one can study G -parity violation effects. An example of this effect is the discovery of the $1^-[\omega(782)\pi]_P$ wave. It is observed for the first time in the $\tau^- \rightarrow \pi^- \pi^- \pi^+ \nu_\tau$ process.

The results of the partial-wave decomposition can be provided later as a data-driven input for an MC generator such as TAUOLA-m [77]. Such a generator will improve ongoing precision tests of the Standard Model in tauon decays, for example the tauon electric and magnetic moments, and the tauon Michel parameters.

The results of this thesis are verifiable in different experimental conditions of BES III and Belle II. At Belle II the number of reconstructed events is expected to rise 1×10^9 such that it will be possible to reach a 1×10^{-5} statistical precision and study in detail partial waves near the tauon mass, which might shed light on the mass and width of the $a_1(1640)$ resonance.

Appendix A Cut-flow table

Process notation, used in Table 13:

- **tau3pi**: signal process, $\tau^- \rightarrow \pi^- \pi^- \pi^+ \nu_\tau$,
- **tau4pi**: $\tau^- \rightarrow \pi^- \pi^- \pi^+ \pi^0 \nu_\tau$,
- **tauNpi0**: $\tau^- \rightarrow \pi^- \pi^- \pi^+ N \pi^0 \nu_\tau$, where $N \geq 2$,
- **tauKpipi**: $\tau^- \rightarrow K^- \pi^- \pi^+ \nu_\tau$,
- **tauNKs**: $\tau^- \rightarrow X N K^0 \nu_\tau$, where $N \geq 1$ (at least one K^0 in the decay products of the tauon),
- **tauNKLs**: $\tau^- \rightarrow X N K_L^0 \nu_\tau$, where $N \geq 1$ (at least one K_L^0 in the decay products of the tauon),
- **tauothers**: other tauon decays not listed above,
- **total**: total number of events,
- **signal**: number of signal events, matches with **tau3pi**,
- **total_bcg**: total number background of events.

	no_cuts	trig	skim	BDT	LID	HID	PHS	ISR	KS_veto	pi0_veto
tau3pi	1481239	1458380	1264739	1170609	1107089	1077071	1076932	1053119	1005994	947010
tau4pi	713371	706402	614038	554888	524572	511093	511085	509080	448540	134883
uds	1749839	1749839	1516895	188980	177051	116469	111292	90335	79395	35245
tauKpipi	57225	56370	49151	46200	43492	13466	13464	13369	12399	11522
charm	917054	917054	794040	63862	51796	37955	36049	28651	25139	10023
tauNpi0	293217	289298	248245	218232	96754	85046	85005	84593	69111	9526
tauother	37059	35742	29905	24498	19439	6878	6805	6663	6020	5374
eeuu	414631	353114	152741	11979	10812	9064	8751	5465	4709	3357
tauNKSSs	20876	20569	17568	16229	15182	13542	13542	13450	2389	1729
tauNKLs	2378	2341	1964	1779	1640	1549	1548	1545	1345	876
bhabha	613713	353808	152029	7136	630	456	446	404	373	306
eecc	35953	34728	24069	1272	1023	758	710	495	421	241
mixed	119144	119144	118913	2373	910	701	655	423	371	187
charged	132240	132240	132073	1963	752	500	460	294	255	132
eess	12986	11174	6114	730	633	332	312	221	161	115
eeee	8957	6548	4044	527	66	51	51	49	49	44
eemm	36306	31644	24558	284	47	42	35	28	24	22
mumu	22275	21582	16628	799	11	9	9	6	6	6
total	6668463	6299977	5167714	2312340	2051899	1874982	1867151	1808190	1656701	1160598
signal	1481239	1458380	1264739	1170609	1107089	1077071	1076932	1053119	1005994	947010
total_bcg	5187224	4841597	3902975	1141731	944810	797911	790219	755071	650707	213588

Table 13: Cut-flow table (exp. 31, exp. 37 runs 0–1000 for eeee and eemm).

Appendix B Acknowledgements

I would like to thank Prof. Stephan Paul for the opportunity to work on such a complicated but rich topic and Daniel Greenwald for his guidance in the world of science, writing, and food.

I want to express my acknowledgement to my present and former TUM colleagues. I thank Boris Grube, Fabian Krinner, Florian Kaspar, Dmitrii Ryabchikov, Stefan Wallner, Mikhail Mikhasenko, and Martin Bartl for the numerous discussions in person about the partial-wave analysis technique, and Dmytro Levit, Katarina Dugic, Lukas Gruessbach, and Lukas Bierwirth for the discussions about Belle and Belle II analysis methods. I want to express my appreciation to Karin Frank who maintains administrative tasks of our group.

I want to thank my colleagues from the Belle collaboration. I thank Michel Hernandez Villanueva, Boris Shwartz, and Vladimir Savinov for refereeing my analysis; Kiyoshi Hayasaka-san, Kenji Inami-san, Sadaharu Uehara-san, Kenta Uno-san, and Yaroslav Kuli for reviewing my analysis during several Belle tauon and two-photon working group meetings, and Shohei Nishida-san and Mikihiko Nakao-san for reviewing my analysis during Belle general and analysis meetings. I am much obliged to Denis Epifanov for the long and fruitful discussions about the caveats of the tau analyses at Belle.

Also, I want to express my deep acknowledgement to my teachers from NSU, SESC NSU, and Blagoveshchensk's school No. 1. Without Valerii Serbo, Boris Shwartz, Simon Eidelman, Aleksandr Bondar, Aleksandr Kuzmin, Boris Weiner, Galina Kuklina, and Svetlana Kirichenko this work would not be possible.

I would like to thank my dear Catriona Bruce for helping me to survive my PhD time and for the careful proofreading of this thesis.

I want to thank my brother Dmitrii Rabusov and my mother Margarita Rabusova for their love and patience.

Bibliography

- [1] G. Zweig. “An SU(3) model for strong interaction symmetry and its breaking. Version 2”. In: *DEVELOPMENTS IN THE QUARK THEORY OF HADRONS. VOL. 1. 1964 - 1978*. Ed. by D. B. Lichtenberg and Simon Peter Rosen. Feb. 1964, pp. 22–101.
- [2] M. Gell-Mann. “A schematic model of baryons and mesons”. In: *Physics Letters* 8.3 (1964), pp. 214–215. ISSN: 0031-9163. DOI: [https://doi.org/10.1016/S0031-9163\(64\)92001-3](https://doi.org/10.1016/S0031-9163(64)92001-3). URL: <https://www.sciencedirect.com/science/article/pii/S0031916364920013>.
- [3] P. Abbon et al. “The COMPASS experiment at CERN”. In: *Nuclear Instruments and Methods in Physics Research Section A: Accelerators, Spectrometers, Detectors and Associated Equipment* 577.3 (2007), pp. 455–518. ISSN: 0168-9002. DOI: <https://doi.org/10.1016/j.nima.2007.03.026>. URL: <https://www.sciencedirect.com/science/article/pii/S0168900207005001>.
- [4] B. Ketzer, B. Grube, and D. Ryabchikov. “Light-meson spectroscopy with COMPASS”. In: *Progress in Particle and Nuclear Physics* 113 (2020), p. 103755. ISSN: 0146-6410. DOI: <https://doi.org/10.1016/j.ppnp.2020.103755>.
- [5] A. Abashian et al. “The Belle Detector”. In: *Nucl. Instrum. Meth. A* 479 (2002), pp. 117–232. DOI: [10.1016/S0168-9002\(01\)02013-7](https://doi.org/10.1016/S0168-9002(01)02013-7).
- [6] D. Boutigny et al. “BaBar technical design report”. In: (Mar. 1995).
- [7] G. Alexander et al. “Evidence for the $\tau \rightarrow \nu\rho\pi$ decay mode”. In: *Physics Letters B* 73.1 (1978), pp. 99–104. ISSN: 0370-2693. DOI: [https://doi.org/10.1016/0370-2693\(78\)90181-8](https://doi.org/10.1016/0370-2693(78)90181-8). URL: <https://www.sciencedirect.com/science/article/pii/0370269378901818>.
- [8] M. Aghasyan et al. “Light isovector resonances in $\pi^- p \rightarrow \pi^- \pi^- \pi^+ p$ at 190 GeV/c”. In: *Phys. Rev. D* 98 (9 Nov. 2018), p. 092003. DOI: [10.1103/PhysRevD.98.092003](https://doi.org/10.1103/PhysRevD.98.092003). URL: <https://link.aps.org/doi/10.1103/PhysRevD.98.092003>.

Bibliography

- [9] D. M. Asner et al. “Hadronic structure in the decay $\tau^- \rightarrow \nu_\tau \pi^- \pi^0 \pi^0$ and the sign of the tau neutrino helicity”. In: *Phys. Rev. D* 61 (1 Dec. 1999), p. 012002. DOI: 10.1103/PhysRevD.61.012002. URL: <https://link.aps.org/doi/10.1103/PhysRevD.61.012002>.
- [10] D. Gomez Dumm et al. “tau \rightarrow pi pi pi nu(tau) decays and the a(1)(1260) off-shell width revisited”. In: *Phys. Lett. B* 685 (2010), pp. 158–164. DOI: 10.1016/j.physletb.2010.01.059. arXiv: 0911.4436 [hep-ph].
- [11] P. A. Zyla et al. “Rev. of Particle Physics”. In: *PTEP* 2020.8 (2020), p. 083C01. DOI: 10.1093/ptep/ptaa104.
- [12] C. Adolph et al. “Observation of a New Narrow Axial-Vector Meson $a_1(1420)$ ”. In: *Phys. Rev. Lett.* 115 (8 Aug. 2015), p. 082001. DOI: 10.1103/PhysRevLett.115.082001. URL: <https://link.aps.org/doi/10.1103/PhysRevLett.115.082001>.
- [13] M. Mikhasenko, B. Ketzer, and A. Sarantsev. “Nature of the $a_1(1420)$ ”. In: *Phys. Rev. D* 91 (9 May 2015), p. 094015. DOI: 10.1103/PhysRevD.91.094015. URL: <https://link.aps.org/doi/10.1103/PhysRevD.91.094015>.
- [14] Fabian Krinner and Stephan Paul. “Precision measurements on dipole moments of the tau and hadronic multi-body final states”. In: *16th International Workshop on Tau Lepton Physics*. Dec. 2021. arXiv: 2112.01980 [hep-ph].
- [15] D. A. Epifanov. “Measurement of Michel parameters in leptonic τ decays at Belle”. In: *Nucl. Part. Phys. Proc.* 287-288 (2017). Ed. by Changzheng Yuan, Xiaohu Mo, and Liangliang Wang, pp. 7–10. DOI: 10.1016/j.nuclphysbps.2017.03.033.
- [16] E Kou et al. “The Belle II Physics Book”. In: *Progress of Theoretical and Experimental Physics* 2019.12 (Dec. 2019). 123C01. ISSN: 2050-3911. DOI: 10.1093/ptep/ptz106. URL: <https://doi.org/10.1093/ptep/ptz106>.
- [17] I.M. Nugent. “Invariant mass spectra of $\tau^- \rightarrow h^- h^- h^+ \nu_\tau$ decays”. In: *Nuclear Physics B - Proceedings Supplements* 253-255 (2014). The Twelfth International Workshop on Tau-Lepton Physics (TAU2012), pp. 38–41. ISSN: 0920-5632. DOI: <https://doi.org/10.1016/j.nuclphysbps.2014.09.010>. URL: <https://www.sciencedirect.com/science/article/pii/S0920563214001418>.
- [18] M. J. Lee et al. “Measurement of the branching fractions and the invariant mass distributions for $\tau^- \rightarrow h^- h^+ h^- \nu_\tau$ decays”. In: *Phys. Rev. D* 81 (2010), p. 113007. DOI: 10.1103/PhysRevD.81.113007. arXiv: 1001.0083 [hep-ex].

- [19] I. M. Nugent et al. “Resonance chiral Lagrangian currents and experimental data for $\tau^- \rightarrow \pi^- \pi^- \pi^+ \nu_\tau$ ”. In: *Phys. Rev. D* 88 (9 Nov. 2013), p. 093012. DOI: 10.1103/PhysRevD.88.093012. URL: <https://link.aps.org/doi/10.1103/PhysRevD.88.093012>.
- [20] O. Shekhovtsova et al. “Resonance chiral Lagrangian currents and τ decay Monte Carlo”. In: *Phys. Rev. D* 86 (2012), p. 113008. DOI: 10.1103/PhysRevD.86.113008. arXiv: 1203.3955 [hep-ph].
- [21] Z. Was and P. Golonka. “TAUOLA as tau Monte Carlo for future applications”. In: *Nuclear Physics B - Proceedings Supplements* 144 (2005). TAU 2004, pp. 88–94. ISSN: 0920-5632. DOI: <https://doi.org/10.1016/j.nuclphysbps.2005.02.012>. URL: <https://www.sciencedirect.com/science/article/pii/S0920563205003257>.
- [22] G. Ecker et al. “The Role of Resonances in Chiral Perturbation Theory”. In: *Nucl. Phys. B* 321 (1989), pp. 311–342. DOI: 10.1016/0550-3213(89)90346-5.
- [23] G. Ecker et al. “Chiral Lagrangians for Massive Spin 1 Fields”. In: *Phys. Lett. B* 223 (1989), pp. 425–432. DOI: 10.1016/0370-2693(89)91627-4.
- [24] G. Ecker and C. Zauner. “Tensor meson exchange at low energies”. In: *Eur. Phys. J. C* 52 (2007), pp. 315–323. DOI: 10.1140/epjc/s10052-007-0372-x. arXiv: 0705.0624 [hep-ph].
- [25] Juan Jose Sanz-Cillero and Olga Shekhovtsova. “Refining the scalar and tensor contributions in $\tau \rightarrow \pi\pi\nu_\tau$ decays”. In: *JHEP* 12 (2017), p. 080. DOI: 10.1007/JHEP12(2017)080. arXiv: 1707.01137 [hep-ph].
- [26] N Toge. *KEK B-factory Design Report*. Tsukuba: KEK, 1995. URL: <https://cds.cern.ch/record/475260>.
- [27] Y. Makida et al. “Performance of a superconducting solenoid magnet for BELLE detector in KEKB B-factory”. In: *IEEE Transactions on Applied Superconductivity* 9.2 (1999), pp. 475–478. DOI: 10.1109/77.783338.
- [28] Yukiyoshi Ohnishi et al. “Accelerator design at SuperKEKB”. In: *Progress of Theoretical and Experimental Physics* 2013.3 (Mar. 2013). 03A011. ISSN: 2050-3911. DOI: 10.1093/ptep/pts083. eprint: <https://academic.oup.com/ptep/article-pdf/2013/3/03A011/4439973/pts083.pdf>. URL: <https://doi.org/10.1093/ptep/pts083>.
- [29] H. Hirano et al. “A high resolution cylindrical drift chamber for the KEK B factory”. In: *Nucl. Instrum. Meth. A* 455 (2000), pp. 294–304. DOI: 10.1016/S0168-9002(00)00513-1.

Bibliography

- [30] G. Alimonti et al. “The BELLE silicon vertex detector”. In: *Nucl. Instrum. Meth. A* 453 (2000). Ed. by F. Takasaki and T. Sumiyoshi, pp. 71–77. DOI: 10.1016/S0168-9002(00)00608-2.
- [31] H. Aihara et al. “Status and upgrade plans of the Belle silicon vertex detector”. In: *Nuclear Instruments and Methods in Physics Research Section A: Accelerators, Spectrometers, Detectors and Associated Equipment* 582.3 (2007). VERTEX 2006, pp. 709–713. ISSN: 0168-9002. DOI: <https://doi.org/10.1016/j.nima.2007.07.057>. URL: <https://www.sciencedirect.com/science/article/pii/S016890020701515X>.
- [32] H. Ikeda et al. “A detailed test of the CsI(Tl) calorimeter for BELLE with photon beams of energy between 20-MeV and 5.4-GeV”. In: *Nucl. Instrum. Meth. A* 441 (2000), pp. 401–426. DOI: 10.1016/S0168-9002(99)00992-4.
- [33] H. Kichimi et al. “The BELLE TOF system”. In: *Nucl. Instrum. Meth. A* 453 (2000). Ed. by F. Takasaki and T. Sumiyoshi, pp. 315–320. DOI: 10.1016/S0168-9002(00)00651-3.
- [34] T. Iijima et al. “Aerogel Cherenkov counter for the BELLE detector”. In: *Nucl. Instrum. Meth. A* 453 (2000). Ed. by F. Takasaki and T. Sumiyoshi, pp. 321–325. DOI: 10.1016/S0168-9002(00)00652-5.
- [35] A. Abashian et al. “The K(L) / mu detector subsystem for the BELLE experiment at the KEK B factory”. In: *Nucl. Instrum. Meth. A* 449 (2000), pp. 112–124. DOI: 10.1016/S0168-9002(99)01383-2.
- [36] Y. Ushiroda et al. “Development of the central trigger system for the BELLE detector at the KEK B factory”. In: *Nucl. Instrum. Meth. A* 438 (1999), pp. 460–471. DOI: 10.1016/S0168-9002(99)00823-2.
- [37] *QQ Documentation Sources*. URL: <https://www.classe.cornell.edu/public/CLE0/soft/qq/>.
- [38] Anders Ryd and David Lange. *EVTGEN Monte Carlo Event Generator*. <https://evtgen.hepforge.org>. Accessed: 2021-11-01.
- [39] Torbjorn Sjostrand. “PYTHIA 5.6 and JETSET 7.3: Physics and manual”. In: (May 1992).
- [40] Torbjorn Sjostrand et al. “High-energy physics event generation with PYTHIA 6.1”. In: *Comput. Phys. Commun.* 135 (2001), pp. 238–259. DOI: 10.1016/S0010-4655(00)00236-8. arXiv: hep-ph/0010017.

- [41] S. Jadach et al. “Monte Carlo program BHLUMI 2.01 for Bhabha scattering at low angles with Yennie-Frautschi-Suura exponentiation”. In: *Computer Physics Communications* 70.2 (1992), pp. 305–344. ISSN: 0010-4655. DOI: [https://doi.org/10.1016/0010-4655\(92\)90196-6](https://doi.org/10.1016/0010-4655(92)90196-6). URL: <https://www.sciencedirect.com/science/article/pii/0010465592901966>.
- [42] F.A Berends, P.H Daverveldt, and R Kleiss. “Monte Carlo simulation of two-photon processes: II: Complete lowest order calculations for four-lepton production processes in electron-positron collisions”. In: *Computer Physics Communications* 40.2 (1986), pp. 285–307. ISSN: 0010-4655. DOI: [https://doi.org/10.1016/0010-4655\(86\)90115-3](https://doi.org/10.1016/0010-4655(86)90115-3). URL: <https://www.sciencedirect.com/science/article/pii/0010465586901153>.
- [43] Stanisław Jadach and Zbigniew Waś. “KORALB — an upgrade to version 2.4”. In: *Computer Physics Communications* 85.3 (1995), pp. 453–462. ISSN: 0010-4655. DOI: [https://doi.org/10.1016/0010-4655\(94\)00091-F](https://doi.org/10.1016/0010-4655(94)00091-F). URL: <https://www.sciencedirect.com/science/article/pii/001046559400091F>.
- [44] S. Jadach, B.F.L. Ward, and Z. Was. “The precision Monte Carlo event generator KK for two-fermion final states in e^+e^- collisions”. In: *Computer Physics Communications* 130.3 (2000), pp. 260–325. ISSN: 0010-4655. DOI: [https://doi.org/10.1016/S0010-4655\(00\)00048-5](https://doi.org/10.1016/S0010-4655(00)00048-5). URL: <https://www.sciencedirect.com/science/article/pii/S0010465500000485>.
- [45] R. Brun et al. “GEANT3”. In: (Sept. 1987).
- [46] K. Inami. *Note on the tau-pair skim*. Belle Note No. 629. Belle Collaboration, 2003.
- [47] Johann H. Kuhn. “Tau kinematics from impact parameters”. In: *Phys. Lett. B* 313 (1993), pp. 458–460. DOI: 10.1016/0370-2693(93)90019-E. arXiv: [hep-ph/9307269](https://arxiv.org/abs/hep-ph/9307269).
- [48] S. Mandelstam. “Determination of the Pion-Nucleon Scattering Amplitude from Dispersion Relations and Unitarity. General Theory”. In: *Phys. Rev.* 112 (4 Nov. 1958), pp. 1344–1360. DOI: 10.1103/PhysRev.112.1344. URL: <https://link.aps.org/doi/10.1103/PhysRev.112.1344>.
- [49] Frederick E James. *Monte Carlo phase space*. CERN Academic Training Lecture. CERN, Geneva, 1 May 1968. Geneva: CERN, 1968. DOI: 10.5170/CERN-1968-015. URL: <http://cds.cern.ch/record/275743>.
- [50] K. Inami. *Location of data set at Nagoya*. https://belle.kek.jp/secured/wiki/doku.php?id=physics:taup:mdst_data. Accessed: 2022-02-23. 2011.

Bibliography

- [51] A. J. Bevan et al. “The Physics of the B Factories”. In: *Eur. Phys. J. C* 74 (2014), p. 3026. DOI: 10.1140/epjc/s10052-014-3026-9. arXiv: 1406.6311 [hep-ex].
- [52] K. Inami and D. Epifanov. [*tautp_ml:1290*] *Duplicated events in TauSkimB and HadronB*. <https://belle.kek.jp/secured/wiki/doku.php?id=physics:taup:removej>. Accessed: 2021-10-23. 2005.
- [53] Siegmund Brandt et al. *The principal axis of jets-an attempt to analyse high-energy collisions as two-body processes*. Tech. rep. 1964.
- [54] E. De La Cruz-Burelo et al. τ lepton mass measurement at Belle II. BELLE2-NOTE-PH-2021-036. Belle II Collaboration, Aug. 2021.
- [55] S.Eidelman, D.Epifanov, and B.Shwartz. *Study of $\tau^- \rightarrow K_S \pi^- \nu_\tau$ decay at Belle*. Belle Note No. 855. Belle Collaboration, 2007.
- [56] R. Brun and F. Rademakers. “ROOT: An object oriented data analysis framework”. In: *Nucl. Instrum. Meth. A* 389 (1997). Ed. by M. Werlen and D. Perret-Gallix, pp. 81–86. DOI: 10.1016/S0168-9002(97)00048-X.
- [57] A. Kolmogoroff. “Sulla determinazione empirica di una legge di distribuzione”. Italian. In: *G. Ist. Ital. Attuari* 4 (1933), pp. 83–91.
- [58] Abhijit Mathad et al. “Efficient description of experimental effects in amplitude analyses”. In: *JINST* 16.06 (2021), P06016. DOI: 10.1088/1748-0221/16/06/P06016. arXiv: 1902.01452 [physics.data-an].
- [59] Diederik P. Kingma and Jimmy Ba. *Adam: A Method for Stochastic Optimization*. 2014. DOI: 10.48550/ARXIV.1412.6980. URL: <https://arxiv.org/abs/1412.6980>.
- [60] F. Krinner et al. “Ambiguities in model-independent partial-wave analysis”. In: *Phys. Rev. D* 97 (11 June 2018), p. 114008. DOI: 10.1103/PhysRevD.97.114008. URL: <https://link.aps.org/doi/10.1103/PhysRevD.97.114008>.
- [61] R. H. Dalitz. “Decay of τ Mesons of Known Charge”. In: *Phys. Rev.* 94 (4 May 1954), pp. 1046–1051. DOI: 10.1103/PhysRev.94.1046. URL: <https://link.aps.org/doi/10.1103/PhysRev.94.1046>.
- [62] J. H. Kühn and E. Mirkes. “Structure functions in τ decays”. In: *Zeitschrift für Physik C Particles and Fields* 56.4 (Dec. 1992), pp. 661–671. ISSN: 1431-5858. DOI: 10.1007/BF01474741. URL: <https://doi.org/10.1007/BF01474741>.

- [63] J. H. Kühn and E. Mirkes. “Structure functions in τ decays”. In: *Zeitschrift für Physik C Particles and Fields* 67.2 (June 1995), pp. 364–364. ISSN: 1431-5858. DOI: 10.1007/BF01571299. URL: <https://doi.org/10.1007/BF01571299>.
- [64] M. Gell-Mann and M. Lévy. “The axial vector current in beta decay”. In: *Il Nuovo Cimento (1955-1965)* 16.4 (May 1960), pp. 705–726. ISSN: 1827-6121. DOI: 10.1007/BF02859738. URL: <https://doi.org/10.1007/BF02859738>.
- [65] Eugene Paul Wigner. *Gruppentheorie und ihre Anwendung auf die Quantenmechanik der Atomspektren*. ger. [Erscheinungsort nicht ermittelbar]: Vieweg, 1951.
- [66] S. U. Chung. “Helicity-coupling amplitudes in tensor formalism”. In: *Phys. Rev. D* 48 (3 Aug. 1993), pp. 1225–1239. DOI: 10.1103/PhysRevD.48.1225. URL: <https://link.aps.org/doi/10.1103/PhysRevD.48.1225>.
- [67] V. Filippini, A. Fontana, and A. Rotondi. “Covariant spin tensors in meson spectroscopy”. In: *Phys. Rev. D* 51 (5 Mar. 1995), pp. 2247–2261. DOI: 10.1103/PhysRevD.51.2247. URL: <https://link.aps.org/doi/10.1103/PhysRevD.51.2247>.
- [68] F. Krinner and S. Paul. “Hadronic Currents and Form Factors in three-body Semileptonic τ Decays”. In: (July 2021). arXiv: 2107.04295 [hep-ph].
- [69] P. A. Zyla et al. “Rev. of Particle Physics”. In: *PTEP* 2020.8 (2020), p. 083C01. DOI: 10.1093/ptep/ptaa104.
- [70] J.M. Blatt and V.F. Weisskopf. *Theoretical Nuclear Physics*. Dover Books on Physics Series. Dover Publications, 1991. ISBN: 9780486668277. URL: <https://books.google.de/books?id=R3BzWYQqNGsC>.
- [71] K. L. Au, D. Morgan, and M. R. Pennington. “Meson dynamics beyond the quark model: Study of final-state interactions”. In: *Phys. Rev. D* 35 (5 Mar. 1987), pp. 1633–1664. DOI: 10.1103/PhysRevD.35.1633. URL: <https://link.aps.org/doi/10.1103/PhysRevD.35.1633>.
- [72] Igor Kachaev and Ihep. “Modified S-wave $\pi\pi$ scattering amplitude for multiparticle PWA”. In: (May 2023). arXiv: 2305.11711 [hep-ph].
- [73] Stefan Wallner. *Exploring the Strange-Meson spectrum with COMPASS in the reaction $K^- + p \rightarrow K^- \pi^- \pi^+ + p$* . en. 2022.
- [74] M. Hatlo et al. “Developments of mathematical software libraries for the LHC experiments”. In: *IEEE Trans. Nucl. Sci.* 52 (2005), pp. 2818–2822. DOI: 10.1109/TNS.2005.860152.
- [75] F. Krinner. “Freed-Isobar Partial-Wave Analysis”. PhD thesis. Munich, Tech. U., 2018.

Bibliography

- [76] F. Krinner. *TauPWA software package*. <https://gitlab.lrz.de/no34sum/taupwa>. Accessed: 2022-08-29.
- [77] A. Rabusov. *TAUOLA-M MC generator*. <https://gitlab.desy.de/arabusov/kkmcBelle>. Accessed: 2023-04-30. 2022.
- [78] Andrei Rabusov, Daniel Greenwald, and Stephan Paul. “Partial wave analysis of $\tau^- \rightarrow \pi^- \pi^+ \pi^- \nu_\tau$ at Belle”. In: *41st International Conference on High Energy Physics*. Nov. 2022. arXiv: 2211.11696 [hep-ex].
- [79] S. Hagopian et al. “rho-omega Interference in the pi-pi+ Decay Mode of the Reaction pi-p + p -> (rho, omega) + n at 2.3 GeVc”. In: *Phys. Rev. Lett.* 25 (1970), pp. 1050–1053. DOI: 10.1103/PhysRevLett.25.1050.
- [80] J. E. Augustin et al. “ $\pi^+ \pi^-$ production in $e^+ e^-$ collisions and ρ - ω interference”. In: (1969). Ed. by J. Tran Thanh Van and D. Treille, p. 35. DOI: 10.1007/BF02755749.
- [81] K. W. Edwards et al. “Resonant structure of tau \rightarrow three pi pi0 neutrino(tau) and tau \rightarrow omega pi neutrino(tau) decays”. In: *Phys. Rev. D* 61 (2000), p. 072003. DOI: 10.1103/PhysRevD.61.072003. arXiv: hep-ex/9908024.
- [82] M. G. Alexeev et al. “Exotic meson $\pi_1(1600)$ with $J^{PC} = 1^{-+}$ and its decay into $\rho(770)\pi$ ”. In: *Phys. Rev. D* 105.1 (2022), p. 012005. DOI: 10.1103/PhysRevD.105.012005. arXiv: 2108.01744 [hep-ex].
- [83] Steven Weinberg. “Charge symmetry of weak interactions”. In: *Phys. Rev.* 112 (1958), pp. 1375–1379. DOI: 10.1103/PhysRev.112.1375.
- [84] D. Ryabchikov. *Isobar fit*. <https://gitlab.lrz.de/e18pwa/isobar-fit>. Accessed: 2023-04-30. 2022.
- [85] M. Fujikawa et al. “High-Statistics Study of the tau- \rightarrow pi- pi0 nu(tau) Decay”. In: *Phys. Rev. D* 78 (2008), p. 072006. DOI: 10.1103/PhysRevD.78.072006. arXiv: 0805.3773 [hep-ex].
- [86] H. Hayashii and E. Tanaka. *Measurement of the branching fraction and the spectral function $\tau \rightarrow 4\pi\nu_\tau$ decays*. Belle Note No. 1363. Belle Collaboration, 2014.
- [87] E. A. Kozyrev et al. “An amplitude analysis of the process $e^+e^- \rightarrow 4\pi$ in the center-of-mass energy range 900–2000 MeV with the CMD3 detector at the VEPP-2000 e^+e^- collider”. In: *EPJ Web Conf.* 212 (2019). Ed. by M. N. Achasov, F. V. Ignatov, and P. P. Krokovny, p. 03008. DOI: 10.1051/epjconf/201921203008.

- [88] G. J. Gounaris and J. J. Sakurai. “Finite-Width Corrections to the Vector-Meson-Dominance Prediction for $\rho \rightarrow e^+e^-$ ”. In: *Phys. Rev. Lett.* 21 (4 July 1968), pp. 244–247. DOI: 10.1103/PhysRevLett.21.244. URL: <https://link.aps.org/doi/10.1103/PhysRevLett.21.244>.